On the steady and unsteady aerodynamics of wing models at low Reynolds numbers for micro air vehicle applications

UNIVERSIDAD DE MÁLAGA

Jorge Aguilar Cabello

Supervisors: Prof. Carlos del Pino Peñas & Prof. Luis Parras Anguita

School of Industrial Engineering,
Department of Mechanical, Thermal and Fluid Engineering

This dissertation is submitted for the degree of
Doctor of Industrial Engineering
in the subject of
Mechatronics Engineering

Universidad de Málaga May 2021

UNIVERSIDAD DE MÁLAGA

AUTOR: Jorge Aguilar Cabello

https://orcid.org/0000-0003-0980-4884

EDITA: Publicaciones y Divulgación Científica. Universidad de Málaga

Esta obra está bajo una licencia de Creative Commons Reconocimiento-NoComercial-SinObraDerivada 4.0 Internacional:
http://creativecommons.org/licenses/by-nc-nd/4.0/legalcode
Cualquier parte de esta obra se puede reproducir sin autorización
pero con el reconocimiento y atribución de los autores.
No se puede hacer uso comercial de la obra y no se puede alterar, transformar o hacer obras derivadas.

Esta Tesis Doctoral está depositada en el Repositorio Institucional de la Universidad de Málaga (RIUMA): riuma.uma.es

A mi tía Katia que siempre ha sido como una segunda madre para mí y toda mi familia, y su apoyo me recargaba de ánimos cada verano.
A mis padres y mi abuelo José, que siempre me han apoyado y han creído en mí aun cuando yo no lo hacía.
A Aina por aguantarme en los altibajos durante este tiempo y ser mi mayor motivación terminar esta tesis.
A Luis y Carlos, quienes han sido mi guía y ejemplo a seguir. Además de transmitirme la "enfermedad", han sido grandes amigos cuando los he necesitado.
A Enrique por su inestimable ayuda en el trabajo conjunto así como como su ejemplo como profesor.
A Paloma, cuya llegada dio el impulso final a las publicaciones derivadas de esta tesis.

UNIVERSIDAD DE MÁLAGA

UNIVERSIDAD
DE MÁLAGA

Acknowledgements

I would like to thank the University of Malaga for providing the facilities and equipment.

Likewise, I am thankful to the Department of Mechanical, Thermal and Fluid Engineering for giving me the opportunity to do my PhD.

Research on chapter 4 have been supported by grants from the Ministerio de Economia y Competitividad of Spain (Grant No. DPI2016-76151-C2-1-R) and from the Junta de Andalucia, Spain (Award/Contract numbers. UMA18-319FEDER-JA-047 and P18-FR-1532). The computations were performed in the Picasso Supercomputer at the University of Malaga, a node of the Spanish Supercomputing Network.

UNIVERSIDAD
DE MÁLAGA

UNIVERSIDAD DE MÁLAGA

ANDALUCÍA TECH
Campus de Excelencia Internacional

Escuela de Doctorado

DECLARACIÓN DE AUTORÍA Y ORIGINALIDAD DE LA TESIS PRESENTADA PARA OBTENER EL TÍTULO DE DOCTOR

D./Dña JORGE AGUILAR CABELLO
Estudiante del programa de doctorado EN INGENIERÍA MECATRÓNICA de la Universidad de Málaga, autor/a de la tesis, presentada para la obtención del título de doctor por la Universidad de Málaga, titulada: On the steady and unsteady aerodynamics of wing models at low Reynolds numbers for micro air vehicle applications

Realizada bajo la tutorización de CARLOS MANUEL DEL PINO PEÑAS y dirección de CARLOS MANUEL DEL PINO PEÑAS Y LUIS PARRAS ANGUITA (si tuviera varios directores deberá hacer constar el nombre de todos)

DECLARO QUE:

La tesis presentada es una obra original que no infringe los derechos de propiedad intelectual ni los derechos de propiedad industrial u otros, conforme al ordenamiento jurídico vigente (Real Decreto Legislativo 1/1996, de 12 de abril, por el que se aprueba el texto refundido de la Ley de Propiedad Intelectual, regularizando, aclarando y armonizando las disposiciones legales vigentes sobre la materia), modificado por la Ley 2/2019, de 1 de marzo.

Igualmente asumo, ante a la Universidad de Málaga y ante cualquier otra instancia, la responsabilidad que pudiera derivarse en caso de plagio de contenidos en la tesis presentada, conforme al ordenamiento jurídico vigente.

En Málaga, a 25 de ENERO de 2021

EFQM AENOR

bequal

Edificio Pabellón de Gobierno. Campus El Ejido.
29071
Tel.: 952 13 10 28 / 952 13 14 61 / 952 13 71 10
E-mail: doctorado@uma.es

UNIVERSIDAD DE MÁLAGA

Los doctores D. Carlos del Pino Peñas y D. Luis Parras Anguita del Departamento de Ingeniería Mecánica, Térmica y de Fluidos de la Universidad de Málaga

CERTIFICAN

Que D. Jorge AGUILAR CABELLO ha realizado bajo nuestra dirección la Tesis Doctoral titulada ON THE STEADY AND UNSTEADY AERODYNAMICS OF WING MODELS AT LOW REYNOLDS NUMBERS FOR MICRO AIR VEHICLE APPLICATIONS que se recoge en la presente memoria, cumpliendo todos los requisitos legales para optar al grado de DOCTOR, por lo que autorizan su lectura y defensa pública en la Escuela de Ingenierías Industriales de la Universidad de Málaga.

Y para que así conste y surta los efectos oportunos, firman el presente certificado en Málaga a 15 de Enero de 2021.

UNIVERSIDAD DE MÁLAGA

Extended Spanish Abstract

La aerodinámica se refiere a la ciencia encargada del estudio del flujo de aire, particularmente cuando se ve afectado por la interacción con un cuerpo, como puede ser el ala de un avión. De la misma forma, todo problema aerodinámico consiste en la determinación de las fuerzas y momentos producidos sobre un objeto inmerso en un flujo. En general, el término aerodinámica se refiere al estudio del aire, pero para la gran mayoría de casos en los que la velocidad del fluido es mucho menor que la velocidad del sonido en el medio, el fluido se puede considerar incompresible, y por tanto se puede utilizar para la predicción de fuerzas y momentos sobre objetos producidas por el flujo de un líquido (hidrodinámica). Esta disciplina ha tenido un desarrollo espectacular desde el siglo XIX con el estudio de perfiles aerodinámicos para el progreso de la aviación, donde se comenzó con una aproximación puramente experimental para después continuar con el desarrollo de modelos teóricos muy precisos de las fuerzas generadas. A día de hoy son innumerables las aplicaciones directas de la aerodinámica sobre perfiles, desde la generación de energía eléctrica con turbinas hidráulicas o aerogeneradores hasta el propio avance de la aviación.

El primer paso para poder realizar una aproximación teórica al problema es la aplicación de simplificaciones basadas en las condiciones del flujo que permitan resolver las ecuaciones de Navier-Stokes de una manera analítica. Las simplificaciones comunes necesarias para el desarrollo de la aerodinámica clásica son la de flujo incompresible, no viscoso y sin transmisión de calor. Tomando esto como base, se han desarrollado distintas teorías que permiten predecir de forma analítica las fuerzas aerodinámicas sobre un objeto:

- Kutta - Joukowski: La primera solución teórica para la sustentación bidimensional de un perfil aerodinámico se obtuvo mediante la teoría del potencial y la transformación conforme (*conformal mapping* en inglés) a principios del siglo XX. Dos de los primeros aerodinamicistas, Kutta en Alemania y Joukowski en Rusia, trabajaron para cuantificar la sustentación lograda por un flujo de aire sobre un cilindro girando. Este problema puede considerarse en términos de una reorientación del movimiento del aire. Si

UNIVERSIDAD DE MÁLAGA

el cilindro atrapa parte del aire en la superficie del cilindro y lo arrastra consigo, desprendiéndose de él hacia abajo lo que produce un impulso en esta dirección (o sustentación), de acuerdo con el principio de conservación de la cantidad de movimiento. La clave de este trabajo es que un perfil aerodinámico puede transformarse fácilmente en este ejemplo (cilindro giratorio) utilizando la transformación conforme, de forma que la solución de sustentación obtenida para un cilindro giratorio puede ser transformada en la sustentación que generaría un determinado perfil aerodinámico.

- Teoría de perfiles esbeltos: Esta teoría fue desarrollada por primera vez por Munk [1], y consta de unas hipótesis simples para relacionar el ángulo de ataque con la sustentación producida por un perfil cuando este se encuentra inmerso en un flujo incompresible y no viscoso. Esta teoría produce un resultado idealizado para el flujo bidimensional alrededor de un perfíl esbelto, que puede interpretarse como el resultado al que tiende un perfil aerodinámico con espesor nulo. Su aplicación se puede resumir de la siguiente forma:

  1. Si el perfil es suficientemente delgado, puede ser modelado como una secuencia de vórtices a lo largo de la cuerda.
  2. La velocidad en cada punto es la suma de la velocidad del medio mas la inducción de la secuencia de vórtices que modela el perfil bidimensional.
  3. Se impone que la geometría del perfil sea una línea de corriente y se calcula la circulación de los vórtices que modelan el perfil aerodinámico que hacen que esto ocurra.
  4. Siguiendo el teorema de Kuttta-Joukowsky, la sustentación es proporcional a la circulación total.

- Alas finitas: Siguiendo con el desarrollo teórico, la sustentación de un ala finita puede ser calculada para un caso no viscoso a partir de las soluciones 2D calculadas anteriormente. En la punta de un ala real se encuentran la zona de baja presión con la alta y siempre se produce un vórtice. Este vórtice induce un cambio en la velocidad que afecta al ángulo de ataque que realmente tendrá el ala localmente, por lo que se hace necesario corregir la teoría bidimensional para tener en cuenta la relación de aspecto del ala. El procedimiento para el cálculo de la sustentación es el siguiente:

  1. Cada sección del ala genera un vórtice en la estela en función de su circulación local.

UNIVERSIDAD DE MÁLAGA

2. Cada filamento de la estela continua de vorticidad induce una velocidad en el ala cambiando el ángulo de ataque.
3. La distribución de circulación compatible con esta situación es la solución de la ecuación de Prandtl

$$\Gamma(y) = \pi c \left(U\alpha - \frac{1}{4\pi} \int_{-b/2}^{b/2} \frac{d\Gamma/dy'}{y-y'} dy' \right) , \tag{1}$$

donde b es la envergadura del ala, y es la posición donde se está calculando la circulación e y' es una variable que recorre todo el largo del ala.

4. La sustentación total se obtiene como la integral a lo largo del ala de la circulación local:

$$C_L = \int_{-b/2}^{b/2} \rho v \Gamma dy' . \tag{2}$$

Estos modelos han demostrado su efectividad y utilidad a lo largo de los años y fueron una de las bases principales que ha permitido el desarrollo de la aviación. Sin embargo, todas estas teorías se construyen sobre la asunción de flujo ideal que solo ocurre para altos números de Reynolds (del orden de 10^5 o superior) y para cuerpos fuselados que no estén en pérdida de sustentación, siempre que no existan efectos de compresibilidad. Esta simplificación tiene un enorme rango de validez ya que incluye el régimen de funcionamiento de la mayoría de aviones, o alas de helicópteros y durante muchos años ha sido justamente el caso que ha suscitado mayor interés de estudio. Sin embargo, debido al creciente desarrollo de vehículos aéreos no tripulados de distintas tipologías, así como la existencia de vehículos aéreos de tamaño mucho mas reducido que las típicas aeronaves, se ha incrementado el interés en los regímenes de vuelo de estos aparatos cuyo funcionamiento es a números de Reynolds mucho mas bajos (del orden de 10^4 o inferior). En estas condiciones, la suposición de flujo ideal deja de tener validez y las teorías vistas anteriormente fallan al predecir las fuerzas aerodinámicas generadas.

En el capítulo 2 se describen las grandes instalaciones experimentales que se han empleado en la tesis, a saber, (i) el túnel aerodinámico equipado con un sensor de fuerza y momentos 3D y (ii) el canal de arrastre equipado con un sensor de fuerza 3D, así como de láser continuo y cámara digital para conocer el campo de velocidad en dos dimensiones mediante la técnica de Velocimetría por Imágenes de Partículas (o PIV en inglés).

En el capítulo 3 se han estudiado las propiedades aerodinámicas de uno de los modelos más sencillos de alas que se utiliza como referencia para el estudio de la aerodinámica, la placa plana rectangular (ver Lee and Su [2]). Este modelo ha sido probado a números

UNIVERSIDAD DE MÁLAGA

de Reynolds ultrabajos (ver Nakayama et al. [3]). Desde principios del siglo XX, la placa plana se ha utilizado para estimar la sustentación para imitar la configuración del túnel de viento, encontrando que las correcciones de sustentación para una placa plana y un perfil aerodinámico son casi idénticas a pequeños ángulos de incidencia (Rosenhead [4]). Más tarde, se informó de las correcciones de sustentación en el límite de espesor cero para un cilindro elíptico en Havelock [5]. El interés por las placas planas no ha disminuido desde entonces, y se ha utilizado como caso de prueba para muchas aplicaciones a bajo *Re* en diferentes áreas de investigación. Algunas de las aplicaciones más directas están relacionadas con la imitación de un par de alerones (ver Savage and Larose [6]), con la simulación de una cascada de palas (ver Fedoul et al. [7]) o con el estudio de la estabilidad del aleteo (ver Wu et al. [8]). Otros se inspiran en los pequeños voladores presentes en la naturaleza, como Zhang et al. [9], que compara de modelos de alas rígidas y de membrana, el análisis de los movimientos de cabeceo Yu and Bernal [10], o la búsqueda de perfiles aerodinámicos ondulados bioinspirados como Murphy and Hu [11]. Además, las placas planas también se han utilizado para estudiar problemas relacionados con el control, como el control activo para proporcionar una mejora de la sustentación (Wang and Gursul [12]) o la determinación de la frecuencia de desprendimiento de vórtices (Chen and Fang [13]), incluso a *Re* ultrabajos (Olmstead and Hector [14], Afgan et al. [15]). Además, las placas planas también han atraído la atención de otras ramas de la ingeniería y se han utilizado, por ejemplo, para analizar el comportamiento de los puentes en Larose and Livesey [16], o para correlacionar la intensidad de la turbulencia y la escala de longitud con la fuerza de sustentación no permanente en un flujo de capa límite atmosférica en Jafari et al. [17].

Uno de los parámetros más significativos para caracterizar la aerodinámica de cualquier objeto es el coeficiente de sustentación, C_L y su variación lineal con el ángulo de ataque, α. Así, la obtención de la pendiente del coeficiente de sustentación ($C_{L\alpha}$) es esencial para el diseño de cualquier ala. Se han realizado comparaciones entre placas planas y otros perfiles aerodinámicos como el NACA0012, encontrando coeficientes de sustentación similares a ángulos de ataque iguales a 6,5° (Lee and Su [2]). Cabe mencionar que se elije la placa plana como objeto de estudio para la dependencia de la sustentación con el ángulo de ataque en aras de la simplicidad ya que otros perfiles aerodinámicos simétricos como la NACA0012 darían lugar a múltiples pendientes a bajos *Re* y bajos ángulos de ataque, como muestra por ejemplo Lee and Su [2].

Se ha medido el coeficiente de sustentación en placas planas rectangulares en la región previa a la entrada en pérdida (*stall* en inglés) y en valores pequeños de la relación entre el espesor geométrico y la cuerda (t/c=0,0133), junto con bajos niveles de turbulencia en condiciones sub-sónicas (números de Mach inferiores a 0,06). Los ensayos experimentales

UNIVERSIDAD DE MÁLAGA

se realizaron con placas de aluminio rectangulares con los bordes redondeados en el túnel aerodinámico cerrado de baja velocidad del Laboratorio de Aero Hidrodinámica de Vehículos de la Universidad de Málaga.

El túnel aerodinámico tiene una sección de ensayo cerrada de 4 m de longitud, sección transversal de 1x1 m^2 y velocidad de la corriente libre desde U_∞=4 hasta 40 m/s. Cada experimento se caracterizó por su número de Reynolds basado en la cuerda Re. Se utilizan placas rectangulares con una cuerda de $c = 150$ mm y un espesor de $t = 2$ mm. La longitud de los perfiles, l, varía entre 75 mm y 600 mm, por lo que la relación de aspecto $AR = 2l/c$ está entre 1 y 8. La intensidad de la turbulencia se ha medido mediante anemometría de hilo caliente obteniendo valores de intensidad de turbulencia inferiores al 0,8% para todos los Reynolds estudiados.

Las fuerzas aerodinámicas se midieron utilizando un sensor de fuerza/par de 6 ejes ATI FTD-GAMMA SI-32-2.5 con una resolución de $\pm 0,006$ N. Este sensor de fuerza se encuentra fijada a un motor paso a paso para controlar el ángulo de ataque. Todo el conjunto está atornillado a la base inferior fuera del túnel de viento para evitar el ruido de vibración estructural que afectaría a las paredes de la sección de pruebas. La placa está fijada firmemente a una base de aluminio, unida a la parte superior del sensor de fuerza mediante 4 tornillos y nivelada respecto al suelo del túnel.

En los experimentos se ha obtenido el coeficiente de sustentación y arrastre de las placas planas barriendo el ángulo de ataque para varias relaciones de aspecto (AR=$1,2,4,8$) y números de Reynolds moderados (Re=40x10^3 a Re=200x10^3). Como las curvas son aproximadamente lineales en el rango de ángulos de ataque pequeños, podemos calcular su pendiente, $C_{L\alpha}$, utilizando un ajuste lineal como el propuesto por Martínez-Aranda et al. [18]. Por lo tanto, se ha calculado la pendiente para el rango de α más pequeño ($-7^\circ \leq \alpha \leq 7^\circ$) para cada par ($Re$, AR). Se observa que el coeficiente de sustentación aumenta con la relación de aspecto y con Re, pero la influencia de Re en la variación del coeficiente de sustentación es menos notable para los valores más pequeños de Re.

La literatura presenta varios estudios que obtienen la pendiente del coeficiente de sustentación para pares específicos de AR y Re pero, hasta donde sabemos, nadie ha ofrecido una correlación que incluya ambos parámetros. Existen varias correlaciones para la pendiente del coeficiente de sustentación que dependen sólo de la AR y que son válidas para Re elevados. Siguiendo la idea de la línea de sustentación de Prandtl pero incluyendo la influencia de Re para valores moderados del mismo, se propone la siguiente correlación obtenida a partir de la batería de experimentos realizada:

$$C^*_{L\alpha} = \left(\frac{2\pi}{1+\alpha_1 * AR^{-1}}\right)\left(\frac{\alpha_2}{1+10^6/Re}\right)^{1/5} \tag{3}$$

UNIVERSIDAD DE MÁLAGA

con $\alpha_1 = 5.21$ and $\alpha_2 = 14.61$, ofreciendo una predicción de la pendiente de la sustentación con un error inferior al 5%.

Ampliando esta idea, en el capítulo 4 se estudia experimentalmente el coeficiente de sustentación en el modelo de ala NACA0012 a diferentes números de Reynolds desde 40x10^3 hasta 200x10^4. El procedimiento experimental es similar al realizado con la placa plana, sin embargo, a diferencia de lo que ocurre en ese caso, el NACA0012 presenta mayor complejidad y se pueden observar distintas pendientes en la sustentación, junto con una sorprendente falta de acuerdo entre los resultados de distintos autores a números de Reynolds moderados (ver Tank et al. [19]). A bajo número de Reynolds observamos se observa de una no-linealidad, lo que hace infructuoso el intento de obtener expresiones fiables para la pendiente de la sustentación. Por el contrario, se han analizado la aparición de la sustentación negativa alrededor de un perfil NACA 0012 para pequeños ángulos de ataque en Reynolds ($\mathscr{O}10^4$). Utilizando un túnel de viento de baja turbulencia, observamos que la no linealidad alrededor del ángulo de ataque cero se produce sólo para una relación de aspecto suficientemente grande. En concreto, para $sAR = 1$, el flujo es completamente tridimensional y C_L es lineal, para $sAR = 2$ captamos una baja no linealidad y para $sAR = 3$ pudimos captar claramente la sustentación negativa. Para entender el origen de este fenómeno, se han realizado simulaciones numéricas 2D utilizando un modelo de transición de TSM implementado en Ansys-Fluent v19.1. Se han validado los resultados obtenidos con los estudios de investigación anteriores que fueron capaces de reproducir la sustentación negativa, obteniendo una buena concordancia. En todos ellos, la sustentación negativa se produce para ángulos de ataque aproximadamente inferiores a 1°, alcanzando su mínimo ($C_L = -0,025$ en nuestras simulaciones) a $0,5^\circ$ aproximadamente. Dado que la sustentación negativa aparece experimentalmente para una relación de aspecto relativamente grande, y que las simulaciones 2D (equivalentes a una relación de aspecto infinita) son capaces de reproducir también la sustentación negativa, el inicio de la sustentación negativa parece estar relacionado principalmente con patrones periódicos bidimensionales tanto temporales como espaciales.

Las simulaciones numéricas también han revelado que la existencia de la sustentación negativa para el caso de $\alpha < 1^\circ$ a $Re = 40 \times 10^3$, está directamente relacionada con la circulación neta en sentido contrario a las agujas del reloj alrededor del perfil. Esta circulación produce un campo de velocidad más rápido en la parte inferior del perfil, disminuyendo su presión estática en esa región, generando una fuerza de sustentación negativa. Otro rasgo característico de los casos con fuerza de sustentación negativa es una prealineación del flujo aguas arriba del perfil aerodinámico que da lugar a un gradiente máximo de presiones con una componente vertical negativa cerca del borde de ataque, promoviendo la sustentación negativa. Para los casos con sustentación positiva, la circulación neta calculada alrededor del

UNIVERSIDAD DE MÁLAGA

perfil aerodinámico es en el sentido de las agujas del reloj, produciendo una sustentación positiva como predice el teorema de Kutta-Joukowski.

Los siguientes capítulos de esta tesis se centran en la medición no intrusiva de las fuerzas en problemas aerodinámicos, que eventualmente se aplicarán a un ala batiente. En primer lugar, en el capítulo 5 se presenta un nuevo programa de PIV programado en Python que se basa en el programa ya existente DPIVSoft. Esta técnica permite conocer la velocidad de un fluido comparando dos imágenes consecutivas del mismo en el que se han introducido partículas trazadoras. Básicamente la técnica consiste en dividir las imágenes en sub-imágenes más pequeñas, y comparar qué movimiento aplicado sobre la primera sub-imagen, haría que fuese más parecida a la segunda mediante el uso de la correlación cruzada. De esta manera se puede conocer el desplazamiento que se ha producido entre los dos instantes de tiempo. Cada sub-imagen producirá un valor de desplazamiento, pudiendo así tener un campo discreto de velocidades. La variante del algoritmo implementada en esta tesis consta de varios pasos en los que las sub-imágenes son deformadas según el campo de velocidad calculado en el paso previo, de forma que en principio, a cada iteración el resultado es más preciso. Entre un paso y el siguiente el tamaño y número de sub-imágenes puede permanecer o variar aumentando la resolución.

Las operaciones para obtener el desplazamiento de cada sub-imagen son independientes del resto por lo que se puede hacer una paralelización completa del procedimiento. Debido a esto, cobra especial sentido hacer uso de la aceleración por Unidades de Procesamiento Gráfico (GPU en inglés) para este problema. La principal aportación al código original, mas allá de la traducción a Python, es la implementación de computación acelerada por GPU utilizando el lenguaje de código abierto Open Computing Language (OpenCL).

La implementación del algoritmo consta de los siguientes pasos que se realizan mediante la ejecución de distintos kernels:

1. Cargar las 2 imágenes sobre las que aplicar el algoritmo.
2. Dividir cada una de las imágenes en distintas sub-imágenes sobre las que aplicar la correlación.
3. Calculo de desplazamientos mediante correlación cruzada.
4. Buscar valores erróneos (*outliers* en inglés) para eliminarlos de la solución.
5. Deformar las imágenes según la solución obtenida
6. Repetir el proceso desde el paso 2 hasta que el resultado llegue a una convergencia según un criterio establecido en el error.

UNIVERSIDAD DE MÁLAGA

Para validar el código se han usado imágenes sintéticas creadas a partir de dos flujos canónicos analíticos: un flujo de Poiseuille y un vortice de Scully. Las partículas trazadoras son generadas aleatoriamente en la imagen y desplazadas respecto a estos campos analíticos. Tras aplicar el algoritmo PIV se compara cada valor local de velocidad con el impuesto analíticamente, obteniendo así los errores debidos a la técnica en sí misma. A pesar de la necesidad de uso de precisión simple en la GPU, la precisión del algoritmo es prácticamente equivalente a la de CPU, con la gran ventaja del aumento de rendimiento, pudiendo llegar a una aceleración de un factor de 300 respecto a su versión ejecutada en CPU.

En el capítulo 6 se contempla el problema de la obtención de las fuerzas mediante la técnica no intrusiva del PIV. Esté método de obtención de fuerzas presenta grandes ventajas por un lado elimina la necesidad de utilizar instrumentos de medida de un alto coste como sensores de fuerza o presión que incrementan y limitan el diseño de los experimentos.

Si bien el campo de velocidad puede ser obtenido directamente a partir de las medidas de PIV, conocer las fuerzas a partir del mismo puede ser mas complicado debido a la sensibilidad al error de los distintos términos empleados en la formulación que predice la fuerza. Existen diversos trabajos relacionados con las estimaciones de fuerzas aerodinámicas a partir de campos 2D de PIV como Lin and Rockwell [20], Noca et al. [21], Unal et al. [22], Noca et al. [23], van Oudheusden et al. [24, 25], Spedding and Hedenström [26], Jardin et al. [27], van Oudheusden [28], Gharali and Jonhson [29], Siala and Liburdy [30] entre otros. Todos los métodos usados presentan grandes desventajas. Por un lado, la necesidad de dominios de cómputo muy grandes o con una enorme precisión cerca de las paredes del cuerpo, la sensibilidad a áreas oscuras o de sombra inevitables o la necesidad del cálculo de la presión. Es bien conocido también que el ruido introducido en las ecuaciones debido a las medidas PIV es una fuente esencial de error para el cálculo indirecto de fuerzas.

Dicho todo esto, la medida de fuerzas mediante PIV está lejos de ser un estándar en la investigación, las limitaciones o rangos de validez son siempre desconocidos a priori, y la aplicación de estas técnicas en experimentos se limita a demostrar que unos parámetros concretos funcionan para un caso concreto comparando los valores con sensores de fuerza. La necesidad del sensor de fuerza como validación, resta sentido al uso de la propia técnica PIV.

Para resolver este problema, el primer paso que se realiza es aplicar distintas formulaciones a campos de velocidad obtenidos de simulaciones CFD en las que se conocen exactamente los valores de velocidad en la malla usada. Al ser el campo de velocidad de la simulación la resultante de la fuerza obtenida, cualquier formulación aplicada sobre el mismo ha de coincidir. Esta aproximación tiene dos ventajas: por un lado se separa la incertidumbre del experimento de la precisión del método en sí, y por otro, el hecho de que las velocidades

UNIVERSIDAD DE MÁLAGA

provengan de una simulación permite modificar la resolución con la resolución espacial, temporal y el tamaño del domino, lo cual requeriría el diseño y dimensionamiento de distintos experimentos para hacer este estudio pormenorizado si se quisiese optar directamente por la vía experimental. Usando esta aproximación, se han estudiado dos métodos para obtener las fuerzas a partir de los campos de velocidad: un balance del momento (MB) y la formulación de impulso (IF).

El balance del momento consiste en aplicar la ecuación de conservación del momento en su forma integral:

$$\frac{d}{dt}\int_V \rho\vec{v}dV + \int_S \rho\vec{v}\vec{v}\vec{n}dS = -\int_S p\vec{n}dS + \int_S \bar{\bar{\tau}}'\vec{n}dS + \int_V \vec{f}_m dV\,, \tag{4}$$

donde en el lado izquierdo de la ecuación todas las integrales pueden ser computadas directamente a partir de los campos de velocidad. Las fuerzas actuando en el cuerpo son las integrales de presión y viscosidad evaluadas en sus superficies del objeto.

Las fuerzas másicas $\vec{f}_{mass}$ son las relativas al sistema de referencia y $\bar{\bar{\tau}}$ representa el tensor de viscosidad que, conociendo las propiedades del fluido, se puede obtener a partir de la velocidad. La principal problemática radica en la integral de presíon, ya que en principio, esta solo se puede obtener indirectamente a partir del campo de velocidad usando la forma diferencial de la ecuación de conservación del momento y aplicando la divergencia para obtener una ecuación de Poisson:

$$\nabla^2 p = \rho\left[\left(\frac{\partial u}{\partial x}\right)^2 + 2\frac{\partial v}{\partial x}\frac{\partial u}{\partial y} + \left(\frac{\partial v}{\partial y}\right)^2\right]. \tag{5}$$

que ha de ser resuelta con un esquema de elementos finitos, por lo que este término añade complejidad y error a las soluciones.

Por otro lado, la formulación del Impulso (IF), desarrollada por Wu et al. [31, 32, 33]; es conocida por descomponer la fuerza en la contribuciones circulatorias y no circulatorias, junto con una dependencia lineal de la vorticidad. Para un volumen no-inercial acotado se puede expresar como:

$$\vec{F}_i = \vec{F}_{iv} + \vec{F}_{iI} + \vec{F}_{io} + \vec{F}_{iRe} + \vec{F}_{iV}\,, \tag{6}$$

donde

$$\vec{F}_{iv} = -\rho\int_{V_c} \mathscr{L} dV\,, \tag{7}$$

UNIVERSIDAD DE MÁLAGA

$$\vec{F}_{iI} = -\rho \int_{V_c} \vec{x} \wedge \frac{\partial \vec{\omega}}{\partial t} dV \,, \tag{8}$$

$$\vec{F}_{io} = -\rho \int_{S_o} \vec{x} \wedge (\vec{n} \wedge \mathscr{L}) \, dS \,, \tag{9}$$

$$\vec{F}_{iRe} = \mu \int_{S_o} [\vec{\omega} \wedge \vec{n} - \vec{x} \wedge (\vec{n} \wedge \bigtriangledown \wedge \vec{\omega})] \, dS \,, \tag{10}$$

$$\vec{F}_{iV} = \rho \frac{d}{dt} \int_{V_s} \vec{V} dV \,. \tag{11}$$

Se usa el programa OpenFoam para calcular numéricamente el flujo no-estacionario y laminar sobre un cilindro cuadrado en agua con una velocidad incidente equivalente a un número de Reynolds igual a 100, definido por la longitud del cuadrado L,

$$Re = \frac{UL}{\nu}, \tag{12}$$

donde U es la velocidad incidente y ν la viscosidad cinemática. OpenFoam resuelve las ecuaciones de Navier-Stokes usando un método de volúmenes finitos. El método usado es de segundo orden en espacio, y para resolver la evolución temporal se usa el método de Crank-Nicolson, el cual también tiene segundo orden en tiempo.

Utilizando los campos de velocidad obtenidos se aplican ambas formulaciones para ver sus rangos de validez. Los campos de presión necesarios para usar la formulación MB son obtenidos directamente de OpenFoam. Ambas formulaciones funcionan relativamente bien para resoluciones de malla a partir de 10 puntos por cuerda, no, sin verse diferencias significativas a partir de 20 puntos del dominio por cuerda. La predicción dada por MB es en todos los casos más precisa que la de IF. Por otro lado el tamaño del dominio de computación tiene gran influencia en los resultados, y sorprendentemente, la precisión aumenta al disminuir el volumen de cálculo. IF presenta una gran sensibilidad al tamaño del domino y puede producir valores completamente erróneos si este es demasiado grande. Se encuentran dos razones para este hecho: por un lado, si los vórtices son difusos en los límites, las integrales de superficie añaden gran error, y por otro, los términos a sumar pueden ser varios órdenes de magnitud superiores a la solución final, produciendo errores al sumarlos. Conociendo los valores óptimos a utilizar, ambas formulaciones son candidatas a una correcta estimación de las fuerzas. La formulación del impulso por su parte, presenta la ventaja adicional de poder

UNIVERSIDAD DE MÁLAGA

estudiar la contribución a la fuerza total de las estructuras de vórtices mediante los términos F_{iv} y F_{iI}.

Por último en el capítulo 7, se aplica la formulación del impulso a un experimento físico sobre un ala oscilante. Los experimentos son realizados utilizando el canal de arrastre de la Universidad de Málaga con dimensiones de 500 $\times$ 500 mm^2 de área de sección y 10000 mm de longitud. Se utiliza como modelo de ala una placa plana de aluminio de 30 $\times 300 \times 1,5$ mm (cuerda, longitud y anchura respectivamente) situada horizontalmente a 250 mm de profundidad.

El movimiento de oscilación de la placa se crea utilizando un motor paso a paso y un sencillo sistema de biela-manivela. Las fuerzas se midieron con un preciso sensor de fuerza digital (Schunk FTD-Nano 17 SI-12-0.12) que sostiene el modelo de ala desde fuera del agua. El transductor mide las fuerzas en tres dimensiones en un rango de 12N$\pm$0,004N para la dirección x y 17N$\pm$0,004N para la dirección z.

Para compensar las fuerzas de inercia, se ha repetido el experimento idéntico en el aire, por lo que el sensor de fuerza midió directamente las fuerzas de inercia. La fuerza de flotación se obtuvo a partir de la densidad del agua, y la posición de la placa plana se obtiene de las propias imágenes utilizadas para el PIV 2D. Para obtener las cargas aerodinámicas, se restan las fuerzas de inercia y flotabilidad a las obtenidas en el experimento dentro del agua.

El equipo PIV consiste en una Fast-CAM Photron SA3 que registraba imágenes de 1024 por 1024 píxeles hasta 1000 fps aunque en este trabajo sólo se han utilizado 125 fps. Para la iluminación de las partículas trazadoras se hace uso de tres láseres continuos de 500mW cada uno, con un conjunto de lentes cilíndricas de -6,25 mm de distancia focal para generar una lámina de 1 mm de espesor. Se utiliza un objetivo Nikon de 105 mm (modelo AF Micro Nikkor 105mm) y f/2,8. Los láseres se encuentran alineados para generar un único plano. Las sombras generadas por el ala se eliminan mediante la colocación de un espejo en el fondo del canal y la posición angular correcta de los láseres. La presencia del espejo también ayuda a aumentar la intensidad del plano láser. Las partículas trazadoras para el PIV son esferas de vidrio huecas recubiertas de plata de 10μm. El plano láser 2D se colocó a lo largo de la dirección de avance del ala. Todo el equipo para el experimento está montado en los raíles del tanque de arrastre de forma que la placa plana oscilante, la cámara y los láseres se mueven solidariamente hacia adelante durante el experimento de configuración de vuelo. El sistema de coordenadas cartesianas asociado se definió como sigue: Las coordenadas y y z son las direcciones transversales (normal de la pared), respectivamente. La coordenada x es la dirección de la corriente definida a lo largo de la corriente libre.

La velocidad y la aceleración de la placa plana en movimiento se obtuvieron a partir de la señal de posición. El disparador de la cámara comienza la adquisición de datos del sensor de

UNIVERSIDAD DE MÁLAGA

fuerza con un retraso de 50 ms. No hay sincronización con el sistema de biela-manivela, ya que la posición instantánea de la placa plana se obtuvo de la grabación de vídeo, como se ha mencionado anteriormente. La configuración de vuelo hacia adelante se inició previamente a la grabación de imágenes durante al menos 50 períodos junto con el tanque de arrastre. En el caso del vuelo suspendido, la grabación comienza antes de que se active el sistema de biela, y sólo utilizamos los dos primeros ciclos en nuestros resultados. Todos los cálculos son realizados en un sistema de referencia no-inercial centrado en el ala. Esto se obtiene interpolando los campos de velocidad obtenidos en una malla centrada en el ala de forma que se reduce el dominio disponible para los cálculos en la dirección z.

Para los casos con una velocidad de avance, los campos de velocidad obtenidos por PIV han sido calculados usando el promediado en fase de 8 ciclos y 3 experimentos diferentes asegurando la reproducibilidad del experimento. La vorticicidad se calcula mediante un método de 9 puntos basado en la circulación (ver Raffel et al. [34]). Comparando los resultados obtenidos mediante IF con los que ofrece el sensor de fuerzas, se puede observar un buena concordancia en los valores de la de la sustentación aunque existen algunas discrepancias en la posiciñón de los máximos y mínimos. Una posible explicación de este error radica en que esta discrepancia se produce al inicio de los movimientos de bajada o subida, donde el flujo permanece totalmente pegado a la superficie de la placa plana. Es precisamente en esos momentos donde desgraciadamente la resolución de la capa límite y la consiguiente generación de vorticidad no está bien resuelta por la 2D-PIV. Esta cuantificación de la incertidumbre también ha sido reportada anteriormente en Siala and Liburdy [30]. Los valores de empuje si bien presentan cierta concordancia, tienen un error mucho mayor en relación a la magnitud de la propia fuerza y no pueden considerarse fiables.

Aplicando nuevamente la formulación IF a un aleteo estático entran en juego patrones caóticos y una fuerte difusión de los vórtices. El tamaño del dominio espacial tiene una mayor influencia en el caso de vuelo suspendido, ya existen vórtices que entran y salen continuamente del dominio haciendo que los resultados presenten un error sustancialmente mayor. Los valores de sustentación no obstante, siguen reproduciendo aceptablemente la tendencia de la señal de fuerza proporcionada por el sensor en los primeros ciclos.

UNIVERSIDAD DE MÁLAGA

UNIVERSIDAD
DE MÁLAGA

Referencias

[1] Max M Munk. General theory of thin wing sections. 1923.

[2] T. Lee and Y. Y. Su. Low Reynolds number airfoil aerodynamic loads determination via line integral of velocity obtained with particle image velocimetry. *Experiments in Fluids*, 53:1177–1190, 2012.

[3] R Nakayama, Y. Nakamura, Y. Ohya, and S. Ozono. A numerical study on the flow around flat plates at low Reynolds numbers. *Journal of Wind Engineering and Industrial Aerodynamics*, 46:255–264, 1993.

[4] L. Rosenhead. The lift on a flat plate between parallel walls. *Proceeding Royal Society London A*, 132:127–152, 1931.

[5] T. H. Havelock. Flow over a flat plate with uniform inlet and incident coherent gusts. *Proceeding Royal Society London A*, 166:178–196, 1938.

[6] M. G. Savage and G. L. Larose. An experimental study of the aerodynamic influence of a pair of winglets on a flat plate model. *Journal of Wind Engineering and Industrial Aerodynamics*, 91:113–126, 2003.

[7] F Fedoul, L Parras, C del Pino, and R Fernandez-Feria. Experimental study of the aerodynamic characteristics of a low-aspect-ratio flat plate array in a configuration of interest for a tidal energy converter. *Journal of Fluids and Structures*, 48:487–496, 2014.

[8] B. Wu, Q. Wang, H. Liao, Y. Li, and M. Li. Flutter derivatives of a flat plate section and analysis of flutter instability at various wind angles of attack. *Journal of Wind Engineering and Industrial Aerodynamics*, 196:104046, 2020.

[9] Z. Zhang, J. P. Hubner, A. Timpe, L. Ukeiley, Y. Abudaram, and P. Ifju. Effect of aspect ratio on flat-plate membrane airfoils. *50th AIAA Aerospace Sciences Meeting including the New Horizons Forum and Aerospace Exposition*, pages 1–15, 2012.

[10] H.-T. Yu and L. P. Bernal. Effects of pivot location and reduced pitch rate on pitching rectangular flat plates. *AIAA Journal*, pages 1–17, 2016.

[11] J. T. Murphy and H. Hu. An experimental study of a bio-inspired corrugated airfoil for micro air vehicle applications. *Experiments in Fluids*, 49:531–546, 2010.

[12] Z. Wang and I. Gursul. Lift enhancement of a flat-plate airfoil by steady suction. *AIAA Journal*, 55:1–18, 2017.

UNIVERSIDAD DE MÁLAGA

[13] J. M. Chen and Y.-C. Fang. Strouhal numbers of inclined flat plates. *Journal of Wind Engineering and Industrial Aerodynamics*, 61:99–112, 1996.

[14] W. E. Olmstead and D. L. Hector. The lift and drag on a flat plate at low Reynolds number via variational methods. *Quarterly of Applied Mathematics*, 25:415–422, 1966.

[15] I. Afgan, S. Benhamadouche, X. Han, P. Sagaut, and D. Laurence. Flow over a flat plate with uniform inlet and incident coherent gusts. *Journal of Fluid Mechanics*, 720: 457–485, 4 2013. ISSN 1469-7645.

[16] G. L. Larose and F. M. Livesey. Performance of streamlined bridge decks in relation to the aerodynamics of a flat plate. *Journal of Wind Engineering and Industrial Aerodynamics*, 69-71:851–860, 1997.

[17] A. Jafari, F. Ghanadi, M. Arjomandi, M. J. Emes, and B. S. Cazzolato. Correlating turbulence intensity and length scale with the unsteady lift force on flat plates in an atmospheric boundary layer flow. *Journal of Wind Engineering and Industrial Aerodynamics*, 189:218–230, 2019.

[18] S Martínez-Aranda, AL García-González, L Parras, JF Velázquez-Navarro, and C del Pino. Comparison of the aerodynamic characteristics of the NACA0012 airfoil at low-to-moderate reynolds numbers for any aspect ratio. *International Journal of Aerospace Sciences*, 4(1):1–8, 2016.

[19] J. Tank, L. Smith, and G.R. Spedding. On the possibility (or lack thereof) of agreement between experiment and computation of flows over wings at moderate Reynolds number. *The Royal Societey*, 7:20160076, 2017.

[20] J.-C Lin and D. Rockwell. Force identification by vorticity fields: techniques based on flow imaging. *Journal of Fluids and Structures*, 10:663–668, 1996.

[21] F. Noca, D. Shiels, and D. Jeon. Measuring instantaneous fluid dynamic forces on bodies, using only velocity fields and their derivatives. *Journal of Fluids and Structures*, 11:345–350, 1997.

[22] M. F. Unal, J.-C. Lin, and D. Rockwell. Force prediction by PIV imaging: a momentum-based approach. *Journal of Fluids and Structures*, 11:965–971, 1997.

[23] F. Noca, D. Shiels, and D. Jeon. A comparison of methods for evaluating time-dependent fluid dynamic forces on bodies, using only velocity fields and their derivatives. *Journal of Fluids and Structures*, 13:551–578, 1999.

[24] B. W. van Oudheusden, F. Scarano, and E. W. F. Casimiri. Non-intrusive load characterization of an airfoil using PIV. *Experiments in fluids*, 40:988–992, 2006.

[25] B. W. van Oudheusden, E. W. F. Casimiri, and F. Scarano. Aerodynamic load characterisation of a low speed aerofoil using particle image velocimetry. *The Aeronautical Journal*, 3240:197–205, 2008.

[26] G. R. Spedding and A. Hedenström. PIV-based investigations of animal flights. *Experiments in fluids*, 46:749–763, 2009.

UNIVERSIDAD DE MÁLAGA

[27] T. Jardin, L. David, and A. Farcy. Characterization of vortical structures and loads based on time-resolved PIV for asymmetric hovering flapping flight. *Experiments in fluids*, 46:847–857, 2009.

[28] B. W. van Oudheusden. PIV-based pressure measurement. *Measurement Science and Technology*, 24, 2013.

[29] K. Gharali and D. A. Jonhson. PIV-based load investigation in dynamic stall for different reduced frequencies. *Experiments in fluids*, 55:1803–1807, 2014.

[30] F. F. Siala and J. A. Liburdy. Leading-edge vortex dynamics and impulse-based lift force analysis of oscillating airfoils. *Experiments in fluids*, 60:157, 2019.

[31] J. Z. Wu, H. Y. Ma, and M. D. Zhou. *Vorticity and vortex dynamics*. Springer, 2006.

[32] J. Z. Wu, X. Y. Lu, and L. X. Zhuang. Integral force acting on a body due to local flow structures. *Journal of Fluid Mechanics*, 576:265–286, 2007.

[33] J. Z. Wu, L. Liu, and T. Liu. Fundamental theories of aerodynamic force in viscous and compressible complex flows. *Progress in Aerospace Sciences*, 99:27–63, 2018.

[34] Markus Raffel, Christian E Willert, Fulvio Scarano, Christian J Kähler, Steve T Wereley, and Jürgen Kompenhans. *Particle image velocimetry: a practical guide*. Springer, 2018.

UNIVERSIDAD DE MÁLAGA

Abstract

In this thesis we have studied the stationary and non-stationary aerodynamic characteristics of wings at low Reynolds numbers commonly achieved in MAVS vehicles. The lift coefficient for a flat plate at low angles of attack is obtained experimentally for various aspect ratios (AR=1, 2, 4, 8) and moderate Reynolds numbers (Re=40x10^3 to Re=200x10^3). The variation of the lift coefficient with the angle of attack in the pre-stall region is consistent with a linear slope approximation. We consider this slope to be a function of both the aspect ratio and Reynolds number. In this research, we provide a correlation that can predict the lift slope value with an average error of less than 5%.

Further extending this idea, we study experimentally the lift coefficient on NACA0012 wing model at different Reynolds numbers from 40x10^3 to 200x10^4. A non-linearity around the zero angle of attack leading to a shift of sign in the lift was observed for a sufficiently large aspect ratio at Re=40×10^3. The existence of the negative lift for wing models with the largest aspect ratio suggests that the three-dimensional effects are negligible. Therefore, two-dimensional simulations were performed to understand the cause of the negative lift. For the cases with the negative lift, the flow displays an interesting feature of pre-alignment with the chord upstream of the airfoil. Furthermore, it was found that the negative lift is directly related to the positive net circulation (anti-clockwise) around the airfoil.

The following chapters of this thesis focus on the non-intrusive measurement of forces that will eventually be applied to a flapping wing. We introduce a new Particle Image Velocimetry (PIV) software coded in Python that is based on the already existing DPIVSoft program which is a double pass with a window deformation algorithm. We present a code for GPU computing using the open-source language Open Computing Language (OpenCL). We obtain almost the same accuracy as with DPIVSoft, but having a dramatic increase in performance.

Two methods of obtaining the forces from velocity fields, the Momentum balance (MB) and the Impulse formulation (IF), have been also studied. We make use of the velocity fields obtained from the numerical simulation of the flow around a square cylinder at Re=100 to investigate the influence of both, grid refinement and window size to perform the calculations in the prediction of the forces. The forces obtained from CFD calculations are compared

UNIVERSIDAD DE MÁLAGA

with those obtained from velocity fields. The prediction given by MB is more accurate than IF. However, the following common features appear in both methods, MB and IF. The grid refinement seems sufficiently precise even when using a coarse grid of 10 boxes in a chord, but the influence of domain size becomes very important, with better results being found for smaller domains, as expected. IF is very sensitive to the window domain and can produce wrong estimations if the vortices are diffused at domain limits or if there are large differences in the order of magnitude between the different terms appearing in the formulations.

In the last study performed, we applied IF to a physical experiment to calculate the forces on an oscillating flat plate. We analyze both forward flight and hovering configurations with a null angle of attack. For this purpose, we perform 2D-PIV measurements in a towing tank to calculate the instantaneous velocity field during several flapping cycles. IF is slightly in better agreement with the forward flight configuration since the vortex patterns, captured using a 2D-PIV in the wake behind the moving plate, are well defined. Conversely, in the hovering configuration, chaotic patterns and strong diffusion are in play. The spatial domain size has a stronger influence in the hovering case than in the forward flight configuration. Finally, the main drawback is that IF does not provide a reasonable estimate of the drag coefficient.

UNIVERSIDAD
DE MÁLAGA

Table of contents

List of figures **7**

List of tables **13**

1 Introduction **1**
1.1 A brief History of Aerodynamics 1
1.2 NACA airfoils 2
1.3 Aerodynamics theories of flight 4
1.3.1 Kutta-Joukowsky 6
1.3.2 Thin Airfoil Theory 12
1.3.3 XFoil panel method 13
1.3.4 Finite wings 15
1.4 UAVS 17
1.4.1 Non-linearity 19
1.4.2 Flapping 21
1.5 Objectives 21
1.6 Structure 22

2 Experimental Facilities **23**
2.1 Introduction 23
2.2 Wind tunnel 23
2.3 Towing tank 25

3 Lift slope for a flat plate configuration **29**
3.1 Background 29
3.2 Experimental arrangement 32
3.3 Experimental measurements 34
3.3.1 Validation 34
3.3.2 Results 34

UNIVERSIDAD DE MÁLAGA

3.4 Correlation between $C_{L\alpha}$, aspect ratio and Re . . . 37
3.5 Comparison with previous results presented in the State of Art . . . 40
3.6 Conclusions . . . 41

4 Non-linearity in a NACA0012 wing model 43
4.1 Background . . . 43
4.2 Experimental Arrangement . . . 45
4.3 Numerical setup . . . 45
4.4 Experimental results . . . 47
4.5 Numerical results . . . 50
4.6 Physical interpretation of the negative lift . . . 52
4.7 Conclusions . . . 58

5 GPU computed PIV 61
5.1 Background . . . 61
5.2 Particle Image Velocimetry with windows deformation . . . 63
5.3 GPU acceleration . . . 64
5.4 Results and performance . . . 66

6 PIV Forces 73
6.1 Background . . . 73
6.2 Force formulations . . . 75
6.2.1 Momentum balance . . . 75
6.2.2 Impulse Formulation . . . 77
6.3 CFD . . . 80
6.4 Results . . . 83
6.5 Conclusions . . . 89

7 Application of the impulse formulation to an experimental flapping flat plate. 91
7.1 Background . . . 91
7.2 Experimental setup . . . 92
7.3 Results . . . 96
7.3.1 Forward flight configuration . . . 96
7.3.2 Hovering configuration . . . 101
7.4 Conclusions . . . 105

UNIVERSIDAD DE MÁLAGA

8 Conclusions and future work **107**
8.1 Conclusions 107
8.2 Future work 109

Referencias **111**

UNIVERSIDAD DE MÁLAGA

UNIVERSIDAD
DE MÁLAGA

List of figures

1.1 Panemones windmill Photograph by Fu Bingchang. Image courtesy of C.H. Foo, Y.W. Foo and Historical Photographs of China, University of Bristol (a), Wright brothers first flight. Image obtained from NASA (b). 2
1.2 4-digits NACA foil representation. 3
1.3 Potential flow streamlines for uniform flow (a) and source/sink (b). 8
1.4 On the left, stream function of a potential vortex (blue), and a source (black) (a). On the right, stream function of a dipole (b). 9
1.5 Complex flow around a cylinder (a), flow around a flat plate (b), flow around a cylinder with rotation Γ (c), flow around a flat plate with rotation (d). . . . 11
1.6 Thin airfoil approximation. 12
1.7 Vortex panel method scheme. 14
1.8 Wing and trailing vortex sheet model for inviscid Prandtl's lifting line theory. 15
1.9 (a) Vigilance UAV of American Army for vigilance purpose[1], (b) Quadricopter[2], (c) Smart bird by Festo based on Seagulls[3]. 18
1.10 Lift curve for a NACA0012 using software XFOIL at $Re = 50 \times 10^3$, for different configurations. Nc is a parameter for the coupling of the inviscid panel method with a boundary layer model. 20

2.1 Schematic of the wind tunnel at Málaga University. 24
2.2 Honeycomb the wind Tunnel in Málaga University. 25
2.3 Aerodynamic model in the test section of the wind tunnel. 26
2.4 3D sketch of the towing tank: flapping flat plate (1), system drive motor (2), transparent towing tank (3), continuous laser sheet (4), support structure (5), speed control computer (6), high-speed camera (7), integrated force sensor and rod-crank shaft system (8), and rail guide (9). The whole system consists of (1)-(2)-(4)-(8) and moves together from right to left in the schedule in the forward flight configuration. 27
2.5 Camera Photron SA3. 28

UNIVERSIDAD DE MÁLAGA

2.6 Snapshot of the experiment setup. 28

3.1 Experimental setup scheme. The inset represents the cross-section of the flat plate to highlight the rounded leading and trailing edges. 33
3.2 Validation of force measurements for a flat plate at $Re = 160 \times 10^3$ and $AR = 2$ comparing with Pelletier & Mueller [1] at $Re = 140 \times 10^3$ and Fedoul *et al.* [2] 150×10^3. 34
3.3 Force signals for $\alpha = 7°$, $AR = 8$, $Re = 2e5$ 35
3.4 Variation of C_L versus α for different AR for the following cases: (a) $Re = 40 \times 10^3$,(b) $Re = 80 \times 10^3$, (c) 120×10^3, (d) $Re = 160 \times 10^3$, (e)$Re = 200 \times 10^3$. 36
3.5 Variation of the measured $C_{L\alpha}$ with respect to Reynolds number (a) and aspect ratio (b). 37
3.6 Variation of the measured $C_{L\alpha}$ with respect to Reynolds number (a) and aspect ratio (b). Superposed in dashed lines the computed $C_{L\alpha^*}$ values using the correlation in equation (9). 38
3.7 Computed $C^*_{L\alpha}$ and $C^{**}_{L\alpha}$ using the correlations in equations (9)-(10) versus measured $C_{L\alpha}$ obtained directly as the slope for different Re and AR, in (a)-(c) respectively. Relative error when computing $C^*_{L\alpha}$, $e_1 = |\frac{C^*_{L\alpha} - C_{L\alpha}}{C_{L\alpha}}|$, (b) and relative error when computing $C^{**}_{L\alpha}$ (d) for each Re, AR value. 39
3.8 Computed $C_{L\alpha^*}$ using the correlation in equation (9) with (a) their corresponding parameters α_1 and α_2 for each author and (b) $\alpha_1 = 5.21$ and $\alpha_2 = 14.61$ versus the measured $C_{L\alpha}$ obtained directly as the slope for different Re and AR for different authors. 40

4.1 Sketch of the NACA 0012 airfoil and relevant quantities (a). Computational domain and boundary conditions (b). 47
4.2 Quasi-structured mesh#3 around the profile with a zoom of the trailing edge region. 48
4.3 Validation of force measurements comparing with Pelletier & Mueller [1] for a flat plate at $Re = 80 \times 10^3$ and $sAR = 3$ using both lift (a) and drag (b) coefficients. 48
4.4 Lift coefficient (C_L) by means of angle of attack for a NACA 0012 at $Re = 90 \times 10^3$ (a) and $Re = 40 \times 10^3$ (b) with semi-aspect ratio sAR from 1 to 3. . 49
4.5 Lift coefficient (C_L) for small angles of attack at $Re = 40 \times 10^3$ and semi-aspect ratio $sAR = 3$. Measures from $-1.75°$ to $1.75°$ in increments of $\Delta\alpha = 0.25$ going in the positive direction in red and going backwards in blue. 51

UNIVERSIDAD DE MÁLAGA

4.6 Comparison of our averaged C_L obtained numerically and experimentally with the published results of Tank *et al.* [3] and Ohtake *et al.* [4]. 51
4.7 Streamlines at $Re = 40 \times 10^3$ for $\alpha = 0.5°$ (a) and $\alpha = 2°$ (b). 53
4.8 Pressure field near the tip of the wing for a case of $Re = 40 \times 10^3$, $\alpha = 0.5°$ (a), $\alpha = 2°$ (b). 54
4.9 Contours of ω_z at $t = 90$ for $Re = 40 \times 10^3$. $\alpha = 0.5°$ and $\Gamma = 0.0032$ (anti-clockwise, a); $\alpha = 2°$ and $\Gamma = -0.045$ (clockwise, b). 55
4.10 Velocity contours for a case of $Re = 40 \times 10^3$, $\alpha = 0.5°$ (a), $\alpha = 2°$ (b). . . 56
4.11 Contours of static pressure for a case of $Re = 40 \times 10^3$, $\alpha = 0.5°$ (a), $\alpha = 2°$ (b). 56
4.12 Temporal evolution of C_L obtained at $t = 90$ for $Re = 40 \times 10^3$ and $\alpha = 0°, 0.5°$ and $2°$ (a), Power Spectral density for the same cases (b). 57
4.13 Contours of static pressure for a case of $Re = 40 \times 10^3$, $\alpha = 0.5°$ $t = 89$ (a), $t = 90$ (b). 58

5.1 Outline of the basic functioning of PIV. 63
5.2 Cross-Correlation process using the correlation theorem [5]. 64
5.3 DPIVSoft algorithm scheme. 65
5.4 Velocity fields obtained with the new implementation of PIV for two different synthetic flows: the 2D (laminar) Hagen-Poiseuille flow (a) and 2D vortex (b). 68
5.5 Azimuthal velocity of vortex as function of radius. 68
5.6 On the left and right columns the 2D Hagen-Poiseuille flow and the Scully vortex, respectively, with the contours of the normalized error on the CPU (a, b) and the GPU (c, d). 70
5.7 Comparison on performance of the GPU implementation compared with CPU. (a) Computational time per image pair, (b) CPU computational time divided by GPU one. 71

6.1 Scheme of the body and surfaces of the control volume. 76
6.2 Sketch of the geometry defined for the problem. It is also shown the square mesh created for the case of 10 divisions per L. 81
6.3 Drag and lift on the square cylinder versus time, for the mesh with $n = 30$ divisions for each L. In dashed red line are marked the values to calculate the maximum and minimum drag and lift, $[D_{min}, D_{max}]$ and $[L_{min}, L_{max}]$ respectively, for $\tau \geq 130$. 82
6.4 Maximum and minimum drag and lift on the square cylinder, increasing the size of the mesh n. 82

UNIVERSIDAD DE MÁLAGA

6.5 Instantaneous flow field around square cylinder from CFD simulations, interpolated on $h = 0.1c$ grid. For the sake of clarity only one every two velocity arrows are shown. Colors indicates non-dimensional vorticity computed using circulation method [5]. Red and green rectangles indicates computational domains for Figs. 6.6 and 6.7. 83
6.6 RMSD of the drag (a) and lift (b) coefficients using the impulse formulation (solid line) and the momentum balance (dashed line) for different computational domains (red squares in Figure 6.5). 84
6.7 RMSD of the drag (a) and lift (b) coefficients using the impulse formulation (solid line) and the momentum balance (dashed line) for different computational domains (green rectangles in Fig. 6.5). 85
6.8 Forces signal computed for h=1/20, and using the square domain $-2 < x < 2$ and $-2 < y < 2$. 86
6.9 Integral terms for drag and lift coefficients using the impulse formulation (a)-(b) and the momentum balance (c)-(d). 87
6.10 Impulse integral terms for lift in two failing cases: (a) windows domain from $-1 < x < 2$, $-1 < y < 1$, and (b) $-3 < x < 5$, $-3 < y < 3$. In (c) both solutions are compared with Openfoam base signal. 88
6.11 Contours of vortical contribution to lift force in the impulse formulation: (a) F_{iv} and (b) F_{iI}. 90

7.1 Experimental setup layout: flapping flat plate (1), rod-crank shaft movement system (2), digital force sensor (3), high-speed camera (4), laser sheet (5), continuous laser source (6). A detail of the rod-crank shaft movement system (2) is given in the inset: DC motor (A), rod (B), and guide rail (C). The whole system (1)-(6) moves together from right to left in the schedule in the forward flight configuration. 93
7.2 Comparison between experimental tracked movement and a sinusoidal . . . 95
7.3 Schematic view of the spatial domain to evaluate the aerodynamic forces on the flat plate. 96
7.4 2D-PIV Isocontours of ω for Re=1000 and k=2.7 (left column) and k=5.4 (right column) at h=-h_0 (a)-(b), h=0 (c)-(d), h=h_0 (e)-(f), h=0 (g)-(h). 98
7.5 Temporal evolution of each term of IF formulation lift for Re=1000 and k=2.7 on the left image. (1)-(4) represents 4 instants showed on right side. . 99
7.6 Experimental windows domain used for computation in the forward flight. . 99

UNIVERSIDAD DE MÁLAGA

7.7 RMSD as a function of the position of surface S_3 on the left column for forward flight experiments. The red points (1)-(3), represents the experimental windows domains shown in Fig. 7.6. Temporal evolution of Lift coefficient is shown on right column for points (1)-(3). 100
7.8 Temporal evolution of C_L and C_D (a)-(b) with different computations (see legend) for Re=1000 and k=2.7 (a) and k=5.4 (b). 101
7.9 2D-PIV Isocontours of ω for Re_h=335.2 (left column) and 668.7 (right column) at $\hat{h}$=0 (a)-(b), $\hat{h}$=$\hat{h}_0$ (c)-(d), $\hat{h}$=0 (e)-(f), $\hat{h}$=-$\hat{h}_0$ (g)-(h), starting at $\hat{h}$=-$\hat{h}_0$. 103
7.10 Lift coefficient against time and its corresponding five terms using IF for Re_h=668.7 on the left. (1)-(4) represents four instants and their associated snapshots are presented on the right side using the vorticity magnitude. . . . 104
7.11 Experimental windows used for computation in the hovering case. 104
7.12 RMSD against area of the domain on the left column for hovering experiments. The red highlighted points (1)-(3), represent the experimental window domains shown in Fig. 7.11. Temporal evolution of Lift coefficient is shown on right column. 105
7.13 Temporal evolution of C_L with different computations (see legend) for Re_h=335.2 (a) and Re_h=668.7 (b). 106

UNIVERSIDAD DE MÁLAGA

UNIVERSIDAD
DE MÁLAGA

List of tables

2.1 Characteristics of force sensor FTD-GAMMA SI-32-2.5 25
2.2 Characteristics of force sensor FTD-Nano 17 SI-12-0.12 26

3.1 Measured turbulence level using Hot-Wire Anemometer for each Reynolds number used for the study. 32
3.2 Main parameters from various studies. 41

4.1 Measured turbulence level using Hot-Wire Anemometer for each Reynolds number used for the study. 45
4.2 Details of the three meshes for the grid convergence study. $Re = 40 \times 10^3$ and $\alpha = 2^o$. Temporal evolutions of 90 time units and average values calculated over the last 30. 46

5.1 PIV parameters 67
5.2 PIV error in % 69

UNIVERSIDAD DE MÁLAGA

UNIVERSIDAD
DE MÁLAGA

Chapter 1

Introduction

1.1 A brief History of Aerodynamics

The term "Aerodynamics" is generally used for flight-related problems and other airflow topics. So taking this definition, we only need to look at a little on History to see how important this Science has been to humanity since ancient times. Sailboats have existed for at least 7000 years. Egypt used wind-powered boats to transport people and goods along the Nile river in 5000 B.C. and the designs of these transport ships have been continuously improving since then. Windmills have been in existence at least until the 9th century, when the first known model of a horizontal windmill was invented (a reconstruction of first known type of windmill is shown in Fig. 1.1(a), is not clear if they existed before), and it has been an invaluable resource since then. Firstly, to process grain or elevate water, but even nowadays we continuously use this concept secondly to generate electricity in wind turbines. Finally, it is worth to mention the first most common thought when we speak of Aerodynamics, the airplanes, which have dramatically changed the world since the first flight of Wright brothers in 1903, shown in Fig. 1.1(b).

Despite the initial definition, the use of word Aerodynamics is not usually limited to air. The physical mechanisms that govern an airflow are the same for non-compressible flows (e.g. liquid). As it is known, the compressibility of air is important, but only when very high speeds are reached, so the word "Aerodynamics" is commonly used to describe also the hydrodynamics and dynamics of gases, as long as they share the same basic principles. This fact allows the application of the results obtained theoretically for the flow around objects for different domains, from airplanes to boats, from water pumps to turbines, or for wind turbines to generate electricity. Other interesting flows in Aerodynamics but for which the compressibility constraints must be taken into account are compressors and gas turbines (turbo-jets in airplanes or for electricity generation). In this thesis we will experimentally

UNIVERSIDAD DE MÁLAGA

Fig. 1.1 Panemones windmill Photograph by Fu Bingchang. Image courtesy of C.H. Foo, Y.W. Foo and Historical Photographs of China, University of Bristol (a), Wright brothers first flight. Image obtained from NASA (b).

study wing models with moderate Reynolds numbers (see its definition below), which is a very small part of the complete set of applications.

Every aerodynamic problem that exists, consists of predicting the forces and moments acting on a submerged body for certain flow conditions. In the case of aerial vehicles, it is easy to see the importance of obtaining reliable results because the flight depends on the lift forces generated on the wings (or propellers), which counteract the gravity that makes the device fly, so the precise prediction of these forces is essential for the design. The Wright brothers understood this problem and in 1902 began a series of experiments in a wind tunnel to test a variety of wing models, including flat plates. These early experiments allowed them to obtain not only the lift and drag coefficients, but also the center of momentum of a variety of wings, achieving a kind of good balance and wing performance that made possible the first manned flight of a heavier-than-air device in 1903. The race to understand and improve the performance of these wings has continue until today, and two main basics approaches have been followed in this work:

- Experimental results based on wing tunnels.
- Development of simplified analytical solutions.

1.2 NACA airfoils

The first profiles used for airplanes were customized. Each inventor in the race to get the first airplane carried out his/her own research and used the shapes he/she considered best from the results in new models of airplanes. In the early 1930s, NACA, NASA's predecessor,

UNIVERSIDAD DE MÁLAGA

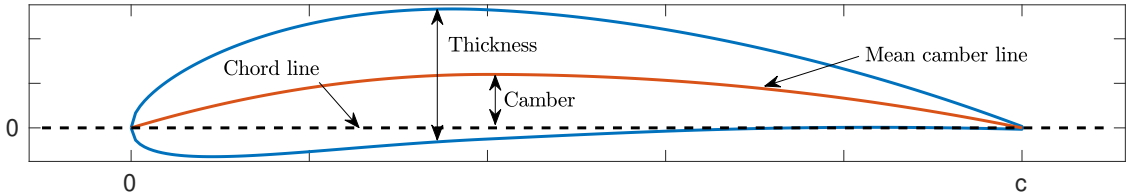

Fig. 1.2 4-digits NACA foil representation.

began a series of final experiments on airfoils systematically constructed for use in aircraft. Many of these early airfoils are still very common today and one of the bases for conducting basic research.

The NACA nomenclature consists of a series of digits, which unequivocally define the shape of the airfoil (see Fig. 1.2). There are two series of NACA depending on the number of digits used to define it, the four and five digits series. The four-digit wing sections of the NACA define the profile [6], as follows

- First digit: describes the maximum camber or curvature as percentage of the chord.
- Second digit: gives the distance from the point of maximum camber of the airfoil to the leading edge in tenths of the chord.
- Last two digits: indicates the maximum thickness of the airfoil as percent of the chord.

Using this definition we can distinguish two types of 4-digits NACA airfoils, if the first two digits are 0, we have a symmetrical airfoil, otherwise we would have a cambered airfoil. The equation that describes the shape is different for these two cases. On the four digits symmetrical airfoil, the thickness as a percentage of the chord follows (1.1)

$$y_t = 5t\left[0.2969\sqrt{x} - 0.1260x - 0.3516x^2 + 0.2843x^3 - 0.1015x^4\right] \tag{1.1}$$

where x is the position along the chord from 0 to 1.00, y_t is the half thickness at a given value of x (centerline to surface) and t is the maximum thickness as a fraction of the chord (given by the last two digits divided by 100).

For an asymmetrical 4-digits NACA, the same formula is used, but with the mean camber line of the following expression

$$y_t = \begin{cases} \frac{m}{p^2}\left(\left(2p\frac{x}{c}\right) - \left(\frac{x}{c}\right)^2\right) & if \quad 0 \leq x \leq pc \\ \frac{m}{(1-p)^2}\left((1-2p) + 2p\left(\frac{x}{c}\right) - \left(\frac{x}{c}\right)^2\right) & if \quad pc \leq x \leq c \end{cases} \tag{1.2}$$

UNIVERSIDAD DE MÁLAGA

where c is the chord, 100 times m is the first digit and 10 times p is the second digit of the NACA nomenclature. This foils have proven to be very optimal for most applications, even nowadays, and are widely used in modern designs for many applications.

1.3 Aerodynamics theories of flight

Being able to predict the flow around a body is incredibly useful for any fluid related application. This can be achieve through the well known principles of basic physics such as conservation of mass, momentum and energy under the right boundary conditions. The fluid is a "squeezed" substance, and solving these equations means knowing the solution at any point in the changing medium, this can only be achieved by differential equations. In this section we will introduce the differential equations that govern the fluid motion.

The conservation of mass, also known as continuity equation, reads as follows

$$\frac{\partial \rho}{\partial t} + \nabla \cdot (\rho \vec{v}) = 0\,, \tag{1.3}$$

where ρ is the fluid density, ∇ denotes its standard derivative as defined in Calculus, and $\vec{v}$ is the velocity field. The temporal derivatives are null for steady-state flows.

The momentum equation is Newton's second law written for a continuous and free deformable substance

$$\frac{\partial \rho \vec{v}}{\partial t} + \nabla \cdot (\rho \vec{v}\vec{v}) = -\nabla p + \nabla \cdot \bar{\bar{\tau}}' + \rho \vec{f}_m\,, \tag{1.4}$$

where p is the thermodynamic pressure, $\bar{\bar{\tau}}'$ is the viscous stress tensor and $\vec{f}_m$ is the mass force vector (forces acting over the mass, like gravity or the ones relative to a non inertial frame of reference). The total force acting on a body immersed in the fluid is the integral of the pressure and the viscous stress on the surfaces

$$\vec{F} = \int_S \bar{\bar{\tau}}' \cdot \vec{n} ds - \int_S p \cdot \vec{n} ds\,. \tag{1.5}$$

It is worth mentioning that the total force acting on an aerodynamic profile ($\vec{F}$) at a certain angle of attack can be decomposed into a lift force (L) and a drag force (D) which are projected at the perpendicular and in the direction of the chord line, respectively. The non-dimensional parameter regarding these two forces are the lift and drag coefficients

$$C_L \equiv \frac{L}{\frac{1}{2}\rho V_\infty^2 c}\,,$$

UNIVERSIDAD DE MÁLAGA

$$C_D \equiv \frac{D}{\frac{1}{2}\rho V_\infty^2 c}, \tag{1.6}$$

where ρ and c are again the fluid density and chord length, and V_∞ is the free-stream velocity.

The conservation of energy says that the increase in the total energy of the fluid is equal to the sum of power sources in it as indicates by (1.7)

$$\rho \frac{\partial \left(e + \frac{1}{2}v^2\right)}{\partial t} + \rho \nabla \cdot \left(e + \frac{1}{2}v^2\right) = \rho \vec{f}_m \cdot \vec{v} + \nabla \cdot (-p\vec{v}) + \nabla \cdot \left(\bar{\bar{\tau}}' \cdot \vec{v}\right) - \nabla \cdot \vec{q} + Q_r, \tag{1.7}$$

where e is the internal energy, $v^2/2$ is the kinetic energy, $\vec{q}$ is the heat introduced into the flow on the surfaces, and Q_r is the volumetric heat generated in it.

Equations (1.3)-(1.5), and (1.7) predict the behavior of any flow, but due to its complexity and the presence of non-linear terms, there is no unique analytical solution. This is the basis of all fluid dynamics problems and they can all be accomplished by different approaches, each with its advantages and disadvantages. The classical analytical approach to predicting the forces on a wing is to make simplifying assumptions until a solution to the conservation equations can be calculated at some threshold. Of course any simplification introduces errors, so finding out what the main mechanisms of flight are and discarding the non-relevant ones is the challenge, but it is not an easy task. The standard theory developed for wing aerodynamics makes use of some strong simplifications that are proven to be very accurate for most cases of interest. These assumptions are stationary, inviscid, and incompressible flow.

The inviscid flow means that there is no thermal conduction, diffusion, or friction forces acting on the body. This is never strictly true in nature, but it is a very accurate approximation in many situations. The Reynolds number is a quantitative form of knowing how good is this assumption for a particular problem. It is defined as the ratio of convective and viscous forces, which, referring to the wing chord, reads as follows:

$$Re = \frac{\rho V_\infty c}{\mu}, \tag{1.8}$$

where μ is the temperature dependent dynamic viscosity, V_∞ is the free-stream (or incident) velocity, and c is the wing chord as mentioned above. Analyzing problems with very large Reynolds numbers will allow us to neglect the viscous terms in the momentum equation.

Assuming steady-state flows, and also if all the thermal and viscous effects from the energy equation (1.7) are neglected as a consequence of the inviscid assumption, we would obtain one of the most important equations on Aerodynamics, the Bernoulli's equation (1.9),

UNIVERSIDAD DE MÁLAGA

which indicates that the pressure plus square velocity in an inviscid flow is a constant for each streamline (or in the whole flow if it is irrotational)

$$p + \frac{1}{2}\rho v^2 = \text{constant}\,. \tag{1.9}$$

Non-compressible flow is the last condition necessary for the theory developed in this chapter. If the density does not change, ρ is no longer a variable and (1.9) will close the problem and the momentum equation (1.4) is not required. This assumption will be approximately true even for air, if the speed of flight is much lower than the speed of sound. The experimental results show that this assumption is reasonable for $M < 0.3$ which for real aircraft will means approximately $V_\infty < 500$ km/h. Nowadays most aircraft fly in this speed range, and only military aircraft (or very few civilian exceptions like the Concorde) reach the speed of sound, so incompressible theory is still useful in today's aircraft design.

With this small introduction we can define how the predictions of the lift over an airfoil are achieved analytically using the potential theory. Here different approaches are presented in chronological order of appearance in the literature.

1.3.1 Kutta-Joukowsky

The first theoretical solution for the two-dimensional lift of an airfoil was obtained by means of potential theory and conformal mapping at the beginning of the 20th century. Two early aerodynamicists, Kutta in Germany and Joukowski in Russia, worked to quantify the lift achieved by an airflow over a spinning cylinder. This problem can be looked at in terms of a redirection of the air motion. If the cylinder traps some air in a boundary layer at the cylinder surface and carries it around with it, shedding it downward, then it has given some of the air a downward momentum. That can give the cylinder an upward momentum in accordance with the principle of conservation of momentum. The important point of this work is that an aerodynamic profile can be easily transformed into this example (spinning cylinder) using complex variables. Let us develop in equations this interesting result along with the calculation of the lift slope or the linear dependence of the lift force on the angle of attack.

When the flow is irrotational the velocity can be written as the gradient of a potential function given by

$$\vec{v} = \nabla\phi\,, \tag{1.10}$$

so replacing $\vec{v}$ in the continuity equation (1.3) we obtain

UNIVERSIDAD DE MÁLAGA

$$\nabla \cdot (\nabla \phi) = \nabla^2 \phi = 0\,, \tag{1.11}$$

which is Laplace's equation. The same type of expression can be obtained by defining the stream function

$$u = \frac{\partial \psi}{\partial y}\,, \quad v = -\frac{\partial \psi}{\partial x}\,, \tag{1.12}$$

where using again the continuity expression and taking into account that the flow is irrotational, we obtain again Laplace's equation

$$\frac{\partial^2 \psi}{\partial x^2} + \frac{\partial^2 \psi}{\partial y^2} = 0\,. \tag{1.13}$$

Laplace's equation is well known by mathematicians and allows different simple flows to be combined to obtain more complex solutions.

Typically, to understand the operating principle of the generation of lift it is necessary to use the complex potential function defined as

$$f(z) = \varphi + i\psi, \tag{1.14}$$

using the complex variable

$$z = x + iy. \tag{1.15}$$

In this case, the velocity field can be easily calculated as

$$f'(z) = \frac{\partial \phi}{\partial x} + i\frac{\partial \psi}{\partial y} = u - iv. \tag{1.16}$$

The stagnation point is the point where the two components of the velocity are zero, thus $f'(z) = 0$.

From this potential flow, one can define different elemental solutions and, due to the linearity of the laplacian, any complex solution can be defined as the addition of multiple elemental solutions.

Uniform flow at angle α

The potential function is defined as

$$f(z) = Uze^{-i\alpha}, \tag{1.17}$$

UNIVERSIDAD DE MÁLAGA

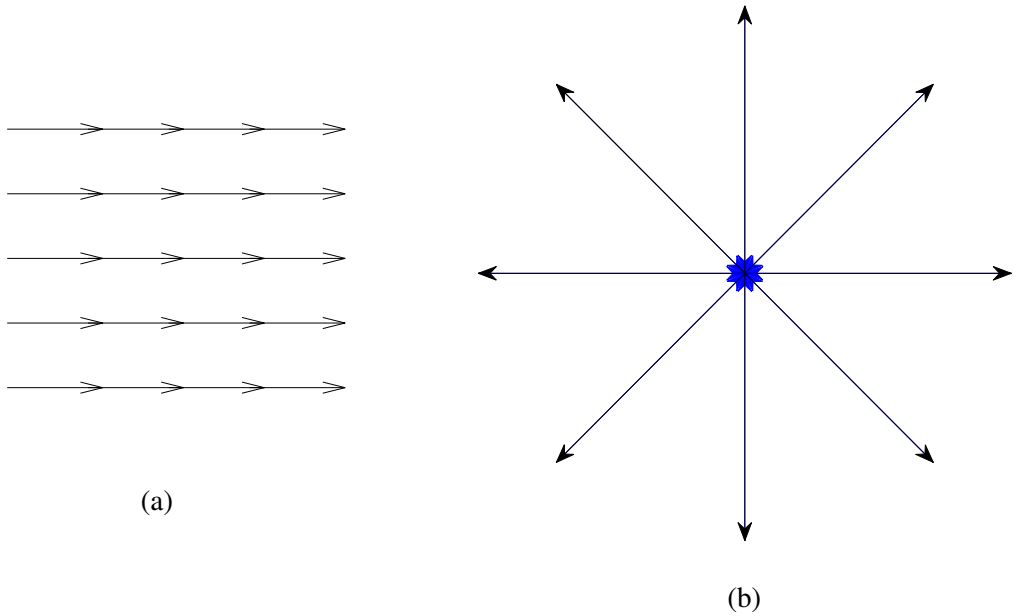

Fig. 1.3 Potential flow streamlines for uniform flow (a) and source/sink (b).

with U the magnitude of the velocity and α the angle of the flow with respect to the horizontal. An example of the streamlines are shown in Fig. 1.3 (a).

Source or sink

The potential function in this case is

$$f(z) = \frac{\pm Q}{2\pi} \ln(z - z_0), \tag{1.18}$$

with $\pm Q$ the flowrate and z_0 the position of the injection/suction point. An example of the streamlines of the flow for a source ($+Q$) is shown in Fig. 1.3 (b) (a sink can be created just by changing the sign of the parameter Q).

Potential vortex

The potential function can be defined as

$$f(z) = \frac{i\Gamma}{2\pi} \ln(z - z_0), \tag{1.19}$$

with Γ the constant circulation of the vortex and z_0 the position of the center of rotation. An example of the streamlines of the flow for a potential vortex is shown in Fig. 1.4 (a).

UNIVERSIDAD DE MÁLAGA

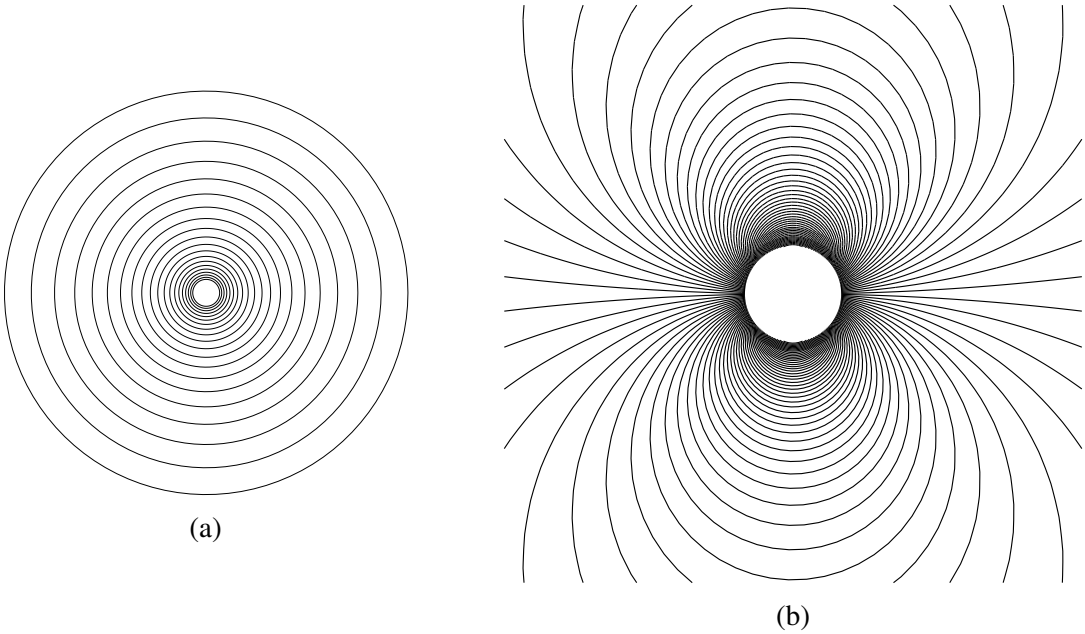

Fig. 1.4 On the left, stream function of a potential vortex (blue), and a source (black) (a). On the right, stream function of a dipole (b).

Dipole

A dipole is defined as a source and a sink placed in the same point of the space. The potential function is given by

$$f(z) = \frac{Me^{i\beta}}{2\pi}\frac{1}{z-z_0}, \tag{1.20}$$

with $Me^{i\beta}$ measuring the intensity of the dipole with the symmetry axis rotated an angle β and z_0 marking its center. The typical streamlines produced by a dipole are shown in Fig. 1.4 (b).

Flow around a circular cylinder

This flow is created by the addition of an uniform flow and a dipole. In this case, we will use the same angle for the symmetry plane of the dipole and the incident angle of the uniform flow

$$f(z) = U\left(ze^{-i\alpha} + \frac{a^2}{ze^{-i\alpha}}\right), \tag{1.21}$$

with a the radius of the cylinder, U the magnitude of the uniform flow and α its angle. This flow is shown in Fig. 1.5 (a) for α=30°.

UNIVERSIDAD DE MÁLAGA

Flow around a flat plate with a given angle of attack

To calculate the flow around a flat plate with a given angle of attack, we make use of a conformal mapping. A conformal mapping is a complex transformation that preserves angles, but not necessarily lengths. In particular, we make use of the Joukowski transformation, defined as

$$\tau = \xi + i\eta = z + \frac{a^2}{z}. \tag{1.22}$$

This expression transforms the flow around a cylinder of radius a as the one presented in Fig. 1.5 (a) in the variables (x,y) into the flow around a flat plate of length $4a$ in the variables (ξ,η) shown in Fig. 1.5 (b). One can observe that the streamline $\psi = 0$ (marked in dashed black line) has two stagnation points. The first one in the intrados of the flat plate and the second one in the extrados of the flat plate. This last stagnation point makes no physical sense, because one expects this line to come out from the trailing edge of the profile. To solve this problem, Kutta-Joukowsky's hypothesis is imposed, which consists in adding a potential vortex in such a way that the velocity at the trailing edge is zero ($f'(a) = 0$). The full potential function of this flow is

$$f(z) = U\left(ze^{-i\alpha} + \frac{a^2}{ze^{-i\alpha}}\right) + i\frac{\Gamma}{2\pi}\log\left(ze^{-i\alpha}\right), \tag{1.23}$$

that is shown in Fig. 1.5 (c) for the flow around a circular cylinder with rotation. To calculate the velocity once the flow is transformed, one has to use the chain rule,

$$G'(\tau) = \frac{df}{dz}\frac{dz}{d\tau} = U\left(\cos(\alpha) + i\sin(\alpha)\frac{1-a/z}{1+a/z}\right). \tag{1.24}$$

Imposing the Kutta-Joukowsky hypothesis, the circulation to be added to obtain $f'(a) = 0$ is

$$\Gamma = 4\pi a U \sin(\alpha). \tag{1.25}$$

Finally, to calculate the forces, the velocity is calculated on the surface of the cylinder $z = ae^{i\theta}$, and using the Bernoulli equation, the pressure on both sides of the flat plate can be easily calculated, providing a normal force F_N,

$$F_N = \int_{-2a}^{2a}(p_- - p_+)d\xi = 4\pi a\rho U^2 \sin(\alpha)\cos(\alpha). \tag{1.26}$$

UNIVERSIDAD DE MÁLAGA

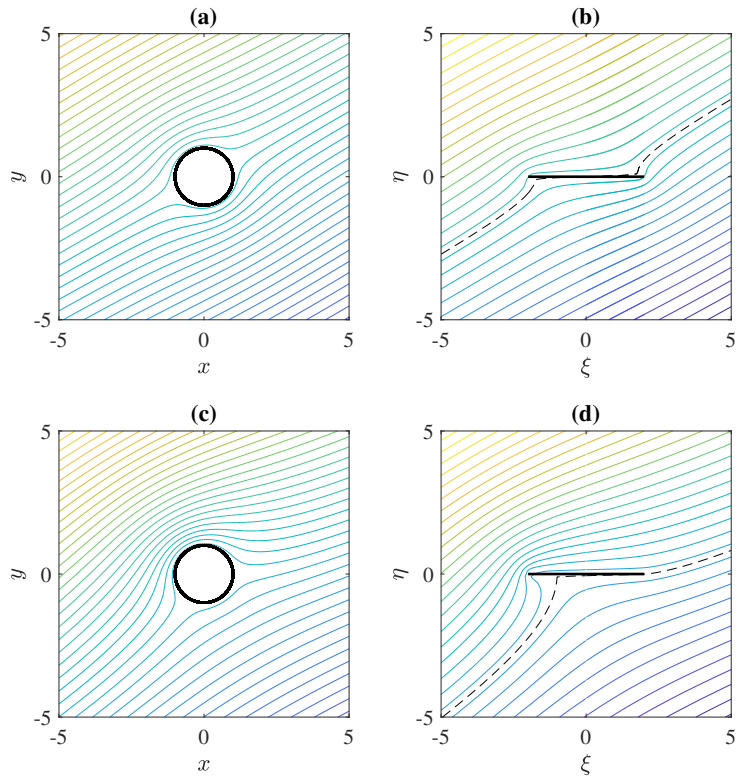

Fig. 1.5 Complex flow around a cylinder (a), flow around a flat plate (b), flow around a cylinder with rotation Γ (c), flow around a flat plate with rotation (d).

The lift is defined in the direction perpendicular to the incident flow, and one can easily calculate it as

$$L = 4\pi a \rho U^2 \sin(\alpha) = \rho U \Gamma. \tag{1.27}$$

The main conclusion of this demonstration is that the generation of lift is due to the circulation created by the profile, which makes the streamlines to bend around it. An analytical approximation of the lift coefficient for a 2D flow around a flat plate can be obtained by linearizing L for small angles of attack, defining the chord as $c = 4a$, so the non-dimensional lift coefficient (1.6) becomes

$$C_L = \frac{L}{\frac{1}{2}\rho U^2 c} \simeq \frac{4\pi a \rho U^2 \alpha}{\frac{1}{2}\rho U^2 c} = 2\pi\alpha. \tag{1.28}$$

UNIVERSIDAD DE MÁLAGA

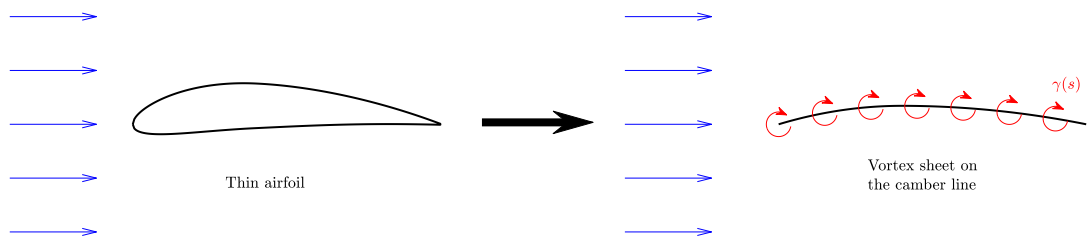

Fig. 1.6 Thin airfoil approximation.

1.3.2 Thin Airfoil Theory

Thin Airfoil Theory was first developed by Marx Munk in 1922 [7], and it is a straightforward hypothesis of airfoils that relates angle of attack to lift for an incompressible and inviscid flow past an airfoil. This theory idealizes the flow past an airfoil as a two-dimensional stream around a thin airfoil which can be envisioned as tending to an airfoil of zero thickness and infinite wingspan. The general idea is the following

1. An airfoil can be modeled like an infinite sheet of vortices along the camber line. If the airfoil is thin enough, we can simplify this to a vortex sheet along the chord line, as shown in Fig. 1.6.

2. The velocity at each point in the flow is the sum of free-stream velocity and velocity induced by the sheet of vortices along the chord line. If we define γ as the strength of the vortex sheet per unit length, γds is the strength at an infinitesimal point on the sheet. The velocity induced at a point in the flow located at a distance r from ds by this infinitesimal portion of the vortex sheet is

$$dV = -\frac{\gamma ds}{2\pi r}, \tag{1.29}$$

where the velocity dV is the magnitude, and its direction is perpendicular to r in cylindrical coordinates. In turn, the velocity $v_i(x)$ at a certain point x induced by all the elemental vortices along the chord line is obtained by integrating Equation from the leading edge

$$v_i(x) = -\int_0^c \frac{\gamma(x')\,dx'}{2\pi(x-x')}, \tag{1.30}$$

where x is the point where the induced velocity is calculated, and x' is a variable along all the chord line.

UNIVERSIDAD DE MÁLAGA

3. To generate the solution, the camber line is imposed to be a streamline, this means that the normal velocity component of this camber line must be 0 at each point, so the strength of each vortex is calculated to occur, which gives the fundamental equation of thin airfoil theory

$$\frac{1}{2\pi}\int_0^c \frac{\gamma(x')\,dx'}{x-x'} = V_\infty\left(\alpha - \frac{dz}{dx}\right). \tag{1.31}$$

4. Following the Kutta-Joukowsky's theorem, the lift force is proportional to circulation

$$L = \rho v \Gamma\,. \tag{1.32}$$

Using this approach for a thin 2D symmetrical airfoil at low angles of attack the resulting lift coefficient is

$$C_L = 2\pi\alpha \tag{1.33}$$

being 2π the lift slope $C_{L\alpha}$. This is the same result obtained from the conformal mapping of a cylinder to a flat plate. Kutta-Joukowsky's theorem has also been proven to obtain the circulation experimentally but for lower *Re* [8].

In the previous section, we showed the simplification of conformal mapping for a flat plate, and this thin airfoil theory, which has a completely different focus, is based on the assumption that if the airfoil is thin enough, we can replace it with a vortex sheet along the chord line, and this would be strictly true for a flat plate, so the interest of a rectangular flat plate as a reference wing for the study is clear [9]. Since the early 20th century, the flat plate has been used to estimate the lift with bounded parallel walls to mimic the wind tunnel configuration, finding that the lift corrections for a flat plate and aerofoil are almost identical at small angles of incidence [10], but as we have pointed, this is limited to high Reynolds numbers (but low enough to fulfill the non-compressible condition). Later, lift corrections to the zero thickness limit were reported for an elliptic cylinder [11]. Interest in flat plates has not diminished since then, and it has been used as a test case for many applications at low *Re* in different areas of research.

1.3.3 XFoil panel method

When the thin airfoil assumption is not fulfilled, or we do not want to introduce the error of its approximation, the next step to study 2D flow is to use a vortex base panel method, which

UNIVERSIDAD DE MÁLAGA

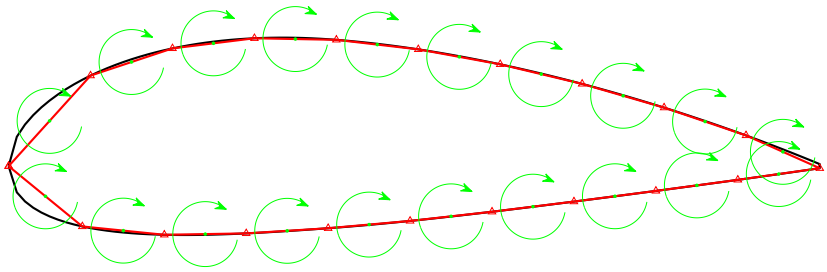

Fig. 1.7 Vortex panel method scheme.

is faster than the simulation of the complete Navier-Stokes equations. This method uses a similar concept to the Thin airfoil theory, but allows us to solve any arbitrary geometry.

The shape of the airfoil is discretized by straight panels, and a potential vortex is placed in the center point of each of these panels as depicted in Fig. 1.7. As more panels are used, the geometry is closer to the real one, but the calculation time to obtain the solution increases. At this point, the circulation of each vortex is unknown, but it is calculated to make the surface of the upper and lower surfaces of the airfoil being streamlines by iterative methods. Once the circulation of each panel vortex is calculated, the lift is obtained by applying Kutta-Joukowsky's theorem to the sum of all the vortex circulations. To sum up, mathematically each panel induces a (yet unknown) velocity on itself and also on the remaining panels. This velocity can be expressed by relatively simple equations, which contain geometric relations like distances and angles between the panels only. All these influences are collected in a matrix and, additionally, a flow condition is defined on the surface, which must be satisfied by the induced velocities. This boundary condition is the requirement that the flow does not pass through the airfoil, but flows tangentially along the surface. Together with the onset flow direction, a system of linear equations can be composed and solved for the unknown panel velocities.

The panel method can theoretically calculate the flow around any airfoil, using exactly the given coordinates, but some problems may occur. To resolve the flow properties in curved regions, enough panels must be used. One should use between 50 and 100 coordinate points, distributed more densely in the leading and trailing edge regions, where the velocity changes rapidly. Very thin airfoils or pointed trailing edges can create numerical difficulties, and the method has no implicit smoothing property. This means that a small deviation of a coordinate from the smooth airfoil shape will result in a wiggle in the resulting velocity distribution. While this is good for smoothing airfoils, it is bad for the subsequent boundary layer analysis. As in real life, wiggles cause premature transition and increased drag. For this reason, the final solution can be combined with the viscous boundary layer for better approximations.

UNIVERSIDAD DE MÁLAGA

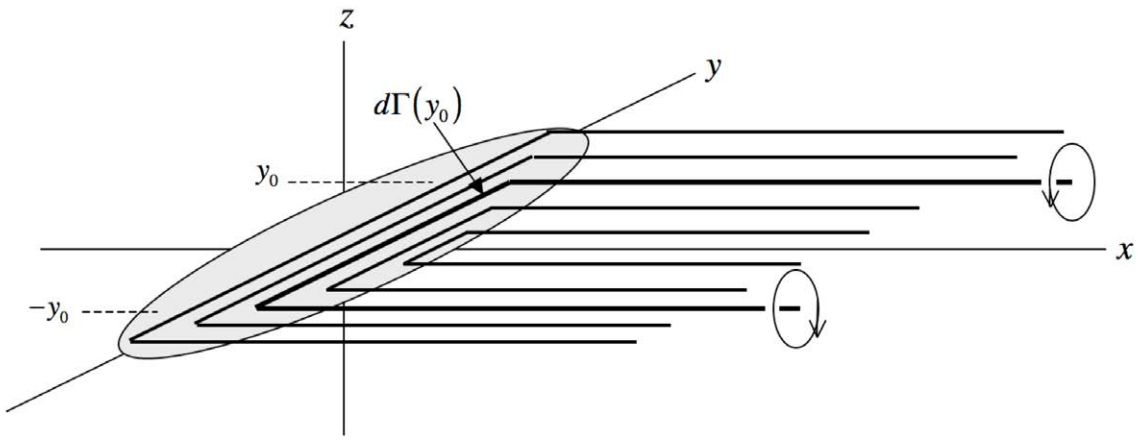

Fig. 1.8 Wing and trailing vortex sheet model for inviscid Prandtl's lifting line theory.

The XFOIL software performs exactly this combination and solves the boundary layer and the wake with an integral dissipation Boundary Layer (BL) formulation of two equations and a transition criterion. The solution obtained interacts strongly with the inviscid result. Thus, XFOIL is also the name of an interactive program for the design and analysis of subsonic isolated airfoils. This program XFOIL has been useful to know in detail the existence of a non-linearity in the lift curve as a function of the angle of attack that will be discussed in detail in the next section regarding Unmanned Aerial Vehicles.

1.3.4 Finite wings

So far, only two-dimensional flow has been taken into account. In a real wing, there is always an end of the (span) section where the intrados and extrados are unified. At this point, the high-pressure flow from the bottom contacts with the low-pressure flow from the top, and the flow begins to roll into a (wingtip) vortex. The change in speed produced by this vortex, modifies the actual angle between the local speed and the wing, so it is necessary to make a correction to the two dimensional theories seen previously to take into account the aspect ratio of the wing: the Prandtl's lifting line theory. The calculation of the circulation and the effective angle of attack along the wingspan is necessary to obtain the total lift of a real wing, the base algorithm is summarized as follows

1. A spanwise circulation distribution $\Gamma(y)$ leads to the shedding of a streamwise vorticity sheet.

2. Each filament of the (continuous) sheet induces a velocity at the location of the wing, which is directed in the vertical direction (see Fig. 1.8).

UNIVERSIDAD DE MÁLAGA

3. The sum of these induced velocities changes the direction of the effective velocity seen by the wing in each section. This modification produces the variation of the local effective angle of attack and therefore modifies the circulation distribution.

4. The circulation distribution compatible with this situation is a solution of Prandtl's equation of the finite-wing theory:

$$\Gamma(y) = \pi c \left(U\alpha - \frac{1}{4\pi} \int_{-b/2}^{b/2} \frac{d\Gamma/dy'}{y-y'} dy' \right) \tag{1.34}$$

   where b is the span length, y is the position where the circulation is being calculating and y' is a variable that goes along the entire span.

5. The total lift is obtained by the integration of local lift coefficient given by the Kutta-Joukowsky's theorem along the entire span:

$$C_L = \int_{-b/2}^{b/2} \rho v \Gamma dy' . \tag{1.35}$$

Prandtl's lifting line for an elliptic planform with constant airfoil shape gives an analytical solution for lift slope,

$$C_{L\alpha} = \frac{a_0}{\left(1 + \frac{a_0}{\pi AR}\right)}, \tag{1.36}$$

with a_0 the slope for the airfoil used at $\alpha = 0$ [12, 13]. In the case of a wing with both an elliptic planform and load distribution the value is a_0=2π.

The Prandtl's lifting line theory is also suitable to be used numerically by iterative methods.

Everything explained so far has been the pillars of Aeronautics throughout the 20th century. The predictions obtained with these inviscid theories have proved to be very accurate and extremely useful for the first stages of wing design, provided that regular airplanes fly at a regime that meets all the conditions required for this theory. Complications arise when we move to moderate Reynolds numbers. The increasing use of fixed wings for unmanned and micro aerial vehicles for which the Reynolds numbers of operation are significantly lower has driven interest in wing Aerodynamics research at moderate *Re* [14–16]. The results predicted by potential theory start to fail in the range of $Re \sim O(10^4)$-$O(10^5)$. The wide range of applications for smaller dimensions makes the understanding of the Aerodynamics at low *Re* numbers crucial. This will be one of the three important contributions of this research.

UNIVERSIDAD DE MÁLAGA

1.4 UAVS

The term Unmanned Aerial Vehicle (UAV) commonly known as drone, refers to a controlled aircraft without any human pilot. The recent development of this type of vehicle have attracted the attention of a large part of the society and the market due to its flexibility to perform different applications. Today these vehicles are widely use for aerial photography, search and rescue tasks or monitoring operations among many others. The possible applications are increasing incredibly fast, and many novel projects seem to indicate the immediate future, such as a network of drones providing wireless internet connection to remote locations[1] or automatic precision farming powered by drones [17–19].

There exist many different types of UAVs, see Fig. 1.9, and they can be organized according to different criteria such as size or purpose, but from an aerodynamic point of view, it makes sense to organize them by their flight mechanism as follows:

- Fixed wings: this type of UAV is similar to a commercial plane, see Fig. 1.9(a). There is an engine that generates the propulsion, and the lift is obtained as a result of the flow over the wings. These vehicles can be as large as a real plane but controlled remotely (especially for military uses, such as surveillance or precision attacks in conflict zones) or as small as a few kilograms, which among some applications, are very popular for model airplane.

- Rotor wings: these vehicles generate lift and propulsion using one or more rotors in a similar way to a helicopter. Probably the most extended type of UAV nowadays is the quadricopter, as the one shown in Fig. 1.9(b). This type of drone has many advantages such as the simplicity of use, the maneuverability, the great stability, and the ability to stay in the air in hovering configuration, which makes it useful for many applications such as taking pictures, videos, transporting small packages, etc.

- Bio-inspired: these vehicles are inspired by nature. They are usually much more complex, since they try to imitate the motion of insects, birds, as shown in Fig. 1.9(c), or fish. These types of drones are becoming increasingly interesting, and new models and applications are appearing. The biggest advantage of this type of device is the flexibility that offers, its movement and maneuverability could be in principle similar to the animals it imitates. The major complication is that the thrust and lift are obtained by the movement of the wings. This introduces a complex mechanism as non-stationary Aerodynamics, wing flexibility or active body mass balance must

[1] Internet.org project by Facebook

UNIVERSIDAD DE MÁLAGA

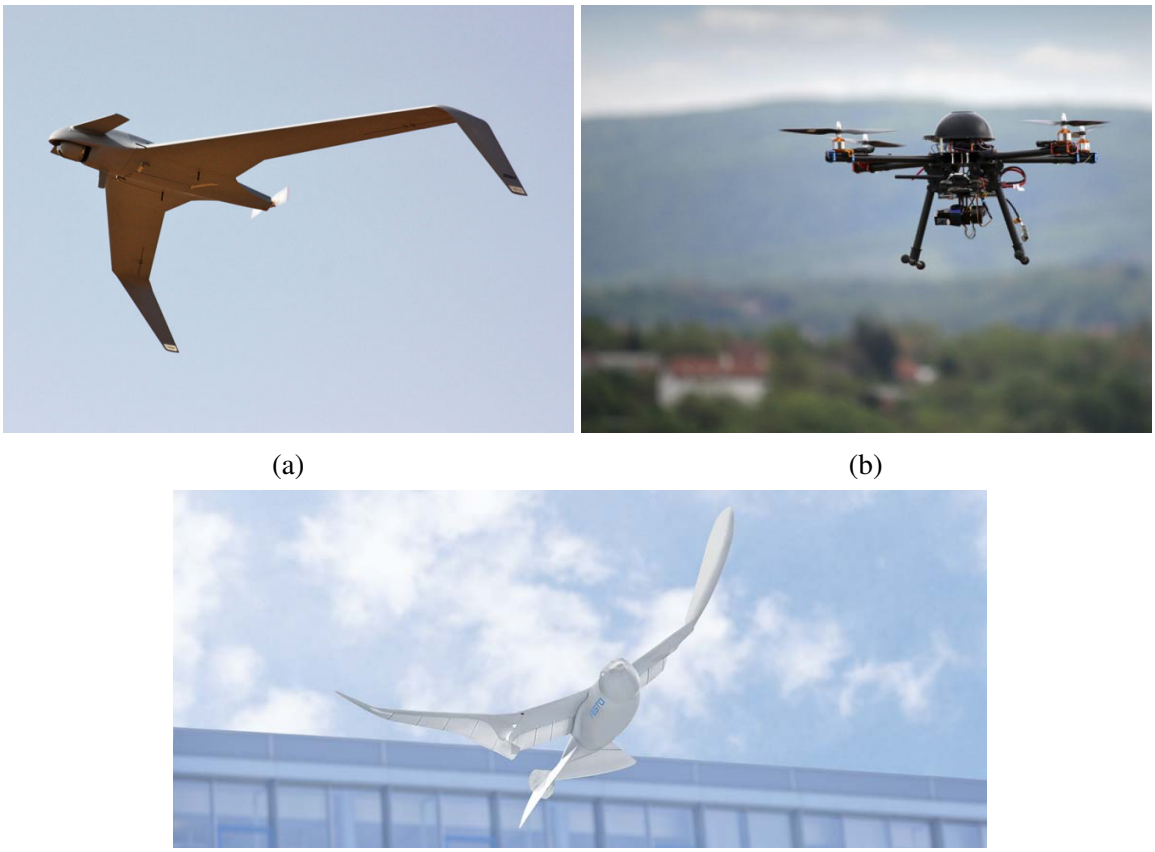

(a) (b)

(c)

Fig. 1.9 (a) Vigilance UAV of American Army for vigilance purpose[2], (b) Quadricopter[3], (c) Smart bird by Festo based on Seagulls[4].

be perfectly controlled to obtain the desired movement. Many examples are being developed based on this type of flight that imitates insects or birds [20, 21].

This type of vehicles has had a great impact on aerodynamic research. Traditionally, airfoil studies focused on the high Reynolds number (Re), a characteristic regime of commercial aircraft scales. However, the increasing use of these small robotic flying devices has focused attention on the moderate Re $(10^4 - 10^5)$ regime, which develops complex aerodynamics that cannot be explained by inviscid theory only. Flights at reduced Reynolds numbers are an open challenge and have prompted interest in researching wings under these conditions because of the possibility of reduction in power and size [14–16]. Two of these challenges will be addressed, the intricate performance of an airfoil when operating at low Reynolds numbers, and the complex flow patterns of non-stationary bio-inspired wings.

[1]Image from https://defense-update.com
[2]Image from https://estaticos.muyinteresante.es
[3]Image from www.Festo.com

UNIVERSIDAD DE MÁLAGA

We will now highlight two aspects dealt with in great depth in this work: (i) the appearance of a non-linearity in the lift curve as a function of the angle of attack and (ii) the determination of indirect methods to estimate the forces exerted in non-stationary aerodynamics at low Reynolds numbers.

1.4.1 Non-linearity

To have an accurate estimate of the lift in a 2D airfoil is important for any aerial vehicle that exists. It is obvious for a fixed wing vehicle, where the relationship between lift and angle of attack, and the pressure center point are the only variables needed for controlled flight, but this is also the case if the flight mechanism is a rotor, as in a helicopter or a quadricopter. Just to get an idea of the latter point a short introduction to the Blade Element Theory (BET) is needed, which is attributed to Drzewiecki [22]. This theory assumes each section of the wing as a 2D case, so there is a local angle of attack depending on the rotation of the wing at that point, allowing further optimization in the wing geometry. Of course, this theory is compatible with Prandlt's lifting line presented on Section 1.3.4, and the only modification is that the angle of attack will depend on the local rotation of the wing. If instead of a stationary fixed wing, we have a rotor, an analytical estimation is achieved using the theory of momentum. This have been developed by many authors since the 19th century, but the current most used model is probably the one given by Glauert [23]. In principle, it consists on apply the momentum equation assuming that the problem can be treated as a stream tube where the rotor is a constantly loaded actuating disc. Combining the loads given by BET (based on the local angle of attack), with the loads of given by the momentum theory (based on induced velocities on the stream tube), we obtain the Blade Element Momentum Theory (BEMT). Developed for the first time by Glauert [23], this theory allows to obtain the rotor performance by iteration, correcting the velocity over the airfoil in each step (for details of the theory see Leishman [24] or Sorensens [25]). Of course there are many variations and methods to improve this basic calculation and to go beyond its limits, such as corrections added directly to take into account different aspects, to include more complex wake models, or to correct the airfoil performance based on flexibility, among many others. Nerveless the lift over the airfoil at a fixed angle of attack is always the first necessary and almost trivial step for a full-scale airplane or helicopter can become a critical drawback for low-Reynolds UAVs.

The complexity of low and moderate Reynolds number aerodynamics has been known for decades as is evident from Lissaman's 1983 review [26], but the lack of direct applications, combined with the difficulties associated with measuring small forces, drove the scientific

UNIVERSIDAD DE MÁLAGA

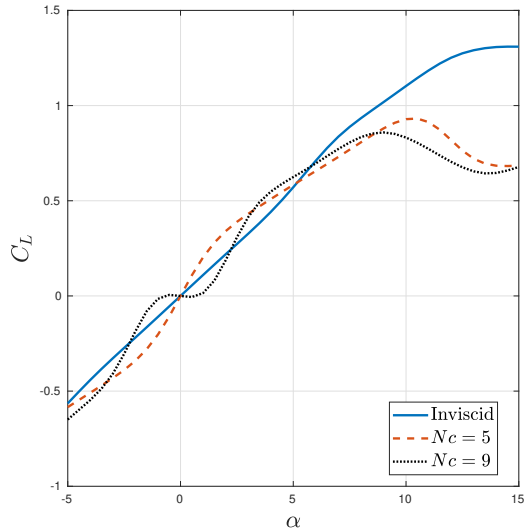

Fig. 1.10 Lift curve for a NACA0012 using software XFOIL at $Re = 50 \times 10^3$, for different configurations. Nc is a parameter for the coupling of the inviscid panel method with a boundary layer model.

community away from this range for a long time. Growing interest in UAVs has revived attention to this flow regime. We will discuss some of their intricacies.

First, the lift slope is no longer given by the potential theory, and the value decreases with the Reynolds number, this difference is not easily noticed for high Reynolds numbers (over 10^6), but it is substantial when it decreases.

The Prandtl's lifting line is based on strong assumptions such as semi-infinite potential vortices with no dissipation, which is approximately true for high Reynolds, low angles of attack, and limited aspect ratios. However, there is a gap when these conditions are pushed and the correction for a wing with some dimension is not so accurate.

To finish, depending on the specific geometry of the airfoil and even for very thin airfoils, the lift and the angle of attack no longer have a linear relationship. The inviscid flow assumption cannot predict this behavior which only appers in some geometries and even using the panel method does not work. Fig. 1.10 is shown this effect using XFOIL at Re=50×10^3, for inviscid and boundary layer coupled solution (the value Nc is the amplification factor of the most amplified frequency that triggers the transition in logarithmic scale). This is a somewhat complicated value to determine and only according to the documentation, the value Nc=9 would correspond to an average clean flow in a wind tunnel and Nc=5 to something more turbulent.

UNIVERSIDAD DE MÁLAGA

The importance of these particularities in the low Reynolds regime is very clear, an incorrect lift prediction for an airfoil will produce an erroneous behavior in the final design of the UAV, and even a catastrophic failure if the wings can enter in a negative lift regime.

1.4.2 Flapping

Bio-inspired vehicles are becoming increasingly popular and, as a result, small animal flapping has become one of the most relevant topics in Aerodynamics over the last few decades Dudley [27], Spedding and Hedenström [28], Shyy et al. [29], Mackowski and Williamson [30]. Such a complex bio-locomotion system is found in insects and birds, and their flying strategies are suitable for engineering systems. The basic idea of natural flyers is to generate a staggering vortex street similar to that of Von Karman's. If the set of vortices is reversed, the wake produces thrust; otherwise, drag appears. The physics of flight at the quasi-steady limit has been considered by several authors such as Weis-Fogh and Jensen [31], Lighthill [32], Childress [33], among others, but all the theories developed for this type of flight have some strong limitations and are only applicable for a reduced range of amplitudes, frequencies or Reynolds numbers. This increases even more the importance of CFD simulations and experiments in this field.

Of course, flapping flight is a more complex mechanism than fixed winged flight or the use of a rotor, and this complexity translates not only into the understanding of the flow, but also into its experimental study. The aerodynamic problem is strongly non-stationary, and the Reynolds number of flying insects and birds is very low $O(1-10^5)$, this means that the forces generated are time-dependent signals that can be quite small, so direct measurement of these forces can be a challenge. It is necessary to use expensive force sensors, and wing vibration, electromagnetic noise in the signal can easily make accurate force measurement impossible, so there is a real interest in non-intrusive (indirect) methods to experimentally estimate the force from the flow behavior. To that end, Particle Image Velocimetry can be applied to the flapping motion to record the velocity field, but the challenge would be the conversion of the velocity field into the force imposed on the non-stationary airfoil accordingly.

1.5 Objectives

This dissertation focuses on the characterization of low and moderate Reynolds number wing aerodynamics. The three main objectives of this work are:

- Characterization of the lift distribution in finite size wings models for different Reynolds numbers and aspect ratio in the application range of UAVs.

UNIVERSIDAD DE MÁLAGA

- Characterization of non-linearity appearing in symmetrical thin foils for moderate Reynolds numbers in the application range of UAVs.
- Development of advanced methods to evaluate aerodynamic forces over 2D foils for strong non-stationary flows, e.g. bio-inspired flight motions.

1.6 Structure

The structure of this dissertation is as follows: Chapter 1 describes the State of the Art and the main objectives of the thesis. Chapter 2 details the experimental devices used in this thesis. In Chapter 3 a heuristic model for the determination of the lifting force in simple wing models for different aspect ratios and Reynolds numbers is discussed. Chapter 4 characterizes the non-linearity present in the symmetrical NACA profiles. Chapter 5 present a novel implementation of the PIV procedure on a GPU for a dramatic increase in processing velocity fields. Chapter 6 presents the details of the indirect method for calculating the lifting force by PIV based on vortical impulse, testing the errors and comparing with the momentum balance. In Chapter 7 this technique is applied to a rectangular flat plate and in Chapter 8, the main conclusions of the work and future lines are indicated.

UNIVERSIDAD DE MÁLAGA

Chapter 2

Experimental Facilities

2.1 Introduction

This chapter provides a brief description of the two main experimental facilities that have been used. In the following chapters a more detailed view of the specific experimental facility and the techniques used are discussed.

2.2 Wind tunnel

All the experiments in chapters 3 and 4 were conducted in the wind tunnel of the Vehicle Aero-Hydrodynamics Laboratory at the Málaga University. A sketch of the closed subsonic wind tunnel is shown in Fig. 2.1. The flow is powered by four fans driven by four three-phase AC motors of 15 kW each and the wind tunnel is capable of working at velocities from 2 to 40 m/s.

This wind tunnel had a test section of 1x1 m^2. The turbines were placed on the top of the tunnel as shown in Fig. 2.1, and they pushed the air through a 2x2 m^2 duct. Before the test section there was a conditioning chamber where the flow was homogenized using a polycarbonate honeycomb followed by a stainless steel net. The 50 mm thick plastic honeycomb had cells of 8 mm of nominal diameter, as shown in Fig 2.2. The stainless steel net had 1 mm cross section holes and was installed after the honeycomb. These two elements made it possible to obtain a level of flow turbulence lower than 1% at any regime achieved with the installation. After this, the flow speed increases due to the presence of the contraction.

The fans speed are controlled using open-loop variable frequency excitation. A customized control system using National Instruments LabView software and hardware was used to

UNIVERSIDAD DE MÁLAGA

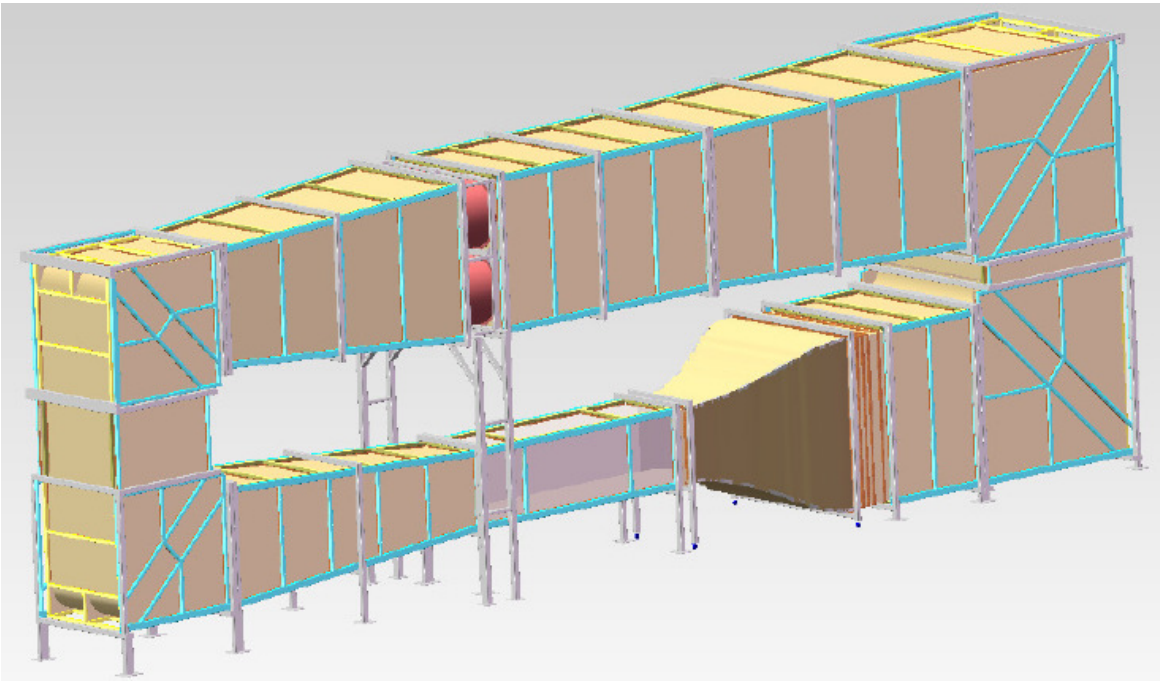

Fig. 2.1 Schematic of the wind tunnel at Málaga University.

monitor pressure, temperature, and speed within the test section in real time. The temperature was recorded with a PT100 probe and the free-stream velocity was measured with a hot wire anemometer.

On the lower surface of the test section there is a holder for fastening the test models. The forces on the models are measured using a 6-component force transducer. On the floor of the test section there is a hole that allows the models to be attached to the transducer using an aluminum disc that is used as a connector. The transducer is an ATI FTD-GAMMA SI-32-2.5. The characteristics of the transducer are shown in the table 2.1. The entire system (load cell together with model mounting) was connected to a servomotor with 10000 steps per revolution to control the angle of attack throughout the experiment. The transducer rotated in solidarity with the model, so that the forces obtained from the transducer were given in different coordinate system from that of the tunnel. Taking the position of null angle of attack, $\alpha = 0°$, where the x-axis of the transducer is aligned with the wind model, we could obtain the forces in a global coordinate system aligned with the wind direction using the following equations:

$$F_{xD} = F_x \cos(\alpha) - F_y \sin(\alpha) \,, \tag{2.1}$$

$$F_{yL} = F_x \sin(\alpha) + F_y \cos(\alpha) \,, \tag{2.2}$$

UNIVERSIDAD DE MÁLAGA

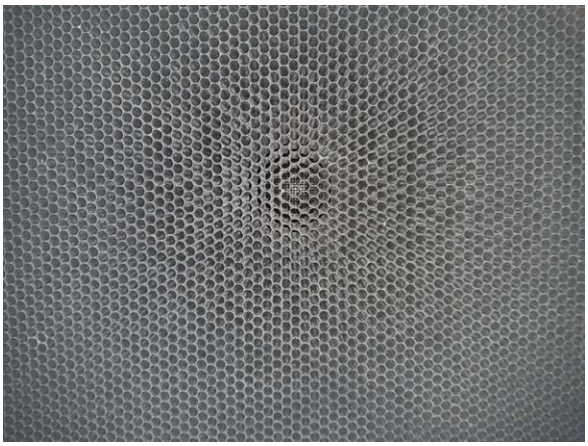

Fig. 2.2 Honeycomb the wind Tunnel in Málaga University.

Table 2.1 Characteristics of force sensor FTD-GAMMA SI-32-2.5

	Maximum Values			Accuracy		
	X	Y	Z	X	Y	Z
Force (N)	32	32	100	1/160	1/160	1/80
Torque (N/m)	2.5	2.5	2.5	1/2000	1/2000	1/2000

where α is the angle rotated by the system, F_x&F_y are the actual forces monitored by the transducer, and F_{xD}&F_{yL} are the projection of the forces on the wind tunnel reference coordinates. The complete system of the servomotor, the transducer and the wing model, are decoupled from the wind tunnel and fixed to the ground to avoid the noise in the force signal produced by the vibrations of the structure. We show in Fig. 2.3 a picture of this arrangement.

2.3 Towing tank

The experiments in chapter 7 have been performed using a towing tank at the Aero-Hydrodynamics Laboratory in Málaga University. This towing tank schematized in Fig. 2.4, was 10 m long and had a cross section of 0.5x0.5 m^2.

In this type of facility, the fluid rest and the aerodynamic model moved along the towing tank. In this case all the equipment is mounted on the same rails that move the model, if the reference frame is given centered on it and in consequence the free-stream velocity is actually the model velocity. The main advantage of this experiment is the extremely low levels of turbulence (almost zero), as long as the only speed variations observed upstream

UNIVERSIDAD DE MÁLAGA

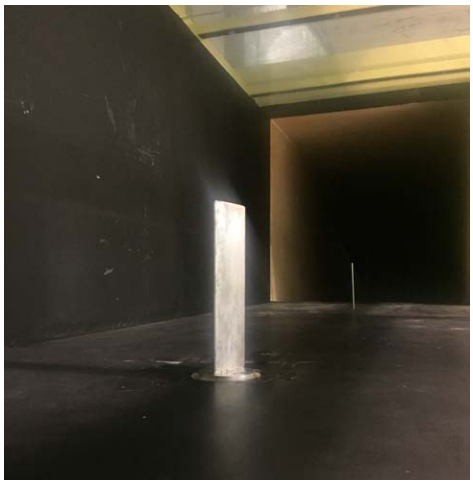

Fig. 2.3 Aerodynamic model in the test section of the wind tunnel.

Table 2.2 Characteristics of force sensor FTD-Nano 17 SI-12-0.12

	Maximum Values			Accuracy		
	X	Y	Z	X	Y	Z
Force (N)	12	12	17	1/320	1/320	1/320
Torque (N/mm)	120	120	120	1/64	1/64	1/64

were caused by buoyancy effects related to temperature differences in the water. For this reason, the temperature was monitored at three different depth levels and at three different sections along the length of the towing tank.

The tested aerodynamic models were attached to a guided rail driven by a computer-controlled step-motor, which allowed the speed to be controlled very precisely from 0 to 400 mm/s.

Two systems have been set up to record the experiment. Firstly, the forces were measured using a 6-axis force sensor Schunk FTD-Nano 17 SI-12-0.12, whose characteristics are shown in table 2.2. Secondly, the velocity field was obtained from Particle Image Velocimetry (PIV). The PIV equipment consisted of a high-speed camera, a laser source and tracers particles. These three components are described below. All the equipment was mounted on the guided rail, so that the reference system was centered on the object under study.

The high-speed camera shown in Fig. 2.5 is a Fast-CAM Photron SA3 which recorded images of 1024 by 1024 pixels up to 1000 FPS although only 125 frames per second have been used in this work, see Fig 2.5. This camera had 4GB of internal storage and was connected to the computer by an Ethernet cable. We used a Nikon 105 *mm* lens (model AF Micro Nikkor 105 *mm*) and f/2.8.

UNIVERSIDAD DE MÁLAGA

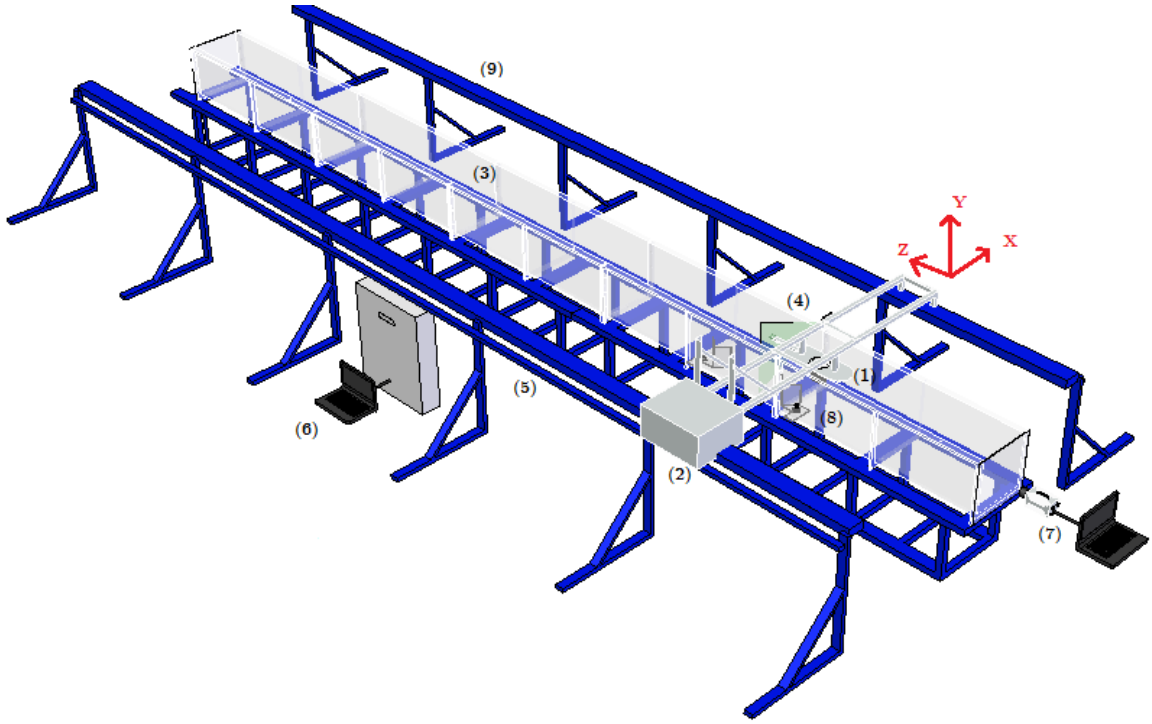

Fig. 2.4 3D sketch of the towing tank: flapping flat plate (1), system drive motor (2), transparent towing tank (3), continuous laser sheet (4), support structure (5), speed control computer (6), high-speed camera (7), integrated force sensor and rod-crank shaft system (8), and rail guide (9). The whole system consists of (1)-(2)-(4)-(8) and moves together from right to left in the schedule in the forward flight configuration.

To obtain the laser sheet we have used three continuous lasers of 500mW each, with a set of cylindrical lenses of -6.25 *mm* focal length to generate a 1 *mm* thick sheet. The lasers were aligned to generate a single plane. There was a mirror under the towing tank to reflect the laser sheet by increasing the intensity, and also helped to overcome possible shadows due to the correct angular position of the lasers.

The tracers for the PIV were silver-coated hollow glass spheres of $10\mu m$. The 2D laser plane was placed at $0.65L$ along the wing's direction of motion. All the equipment for the experiment was mounted on the rails of the towing tank, as shown in Fig 2.6. Thus, the wing model (1) and (8), the camera (7), and the lasers (4) moved forward during the flight configuration experiment. The associated cartesian coordinate system was defined as follows: y and z-coordinates are spanwise and transverse (wall-normal) directions, respectively. The x-coordinate is the streamwise direction defined along the free stream.

UNIVERSIDAD DE MÁLAGA

Fig. 2.5 Camera Photron SA3.

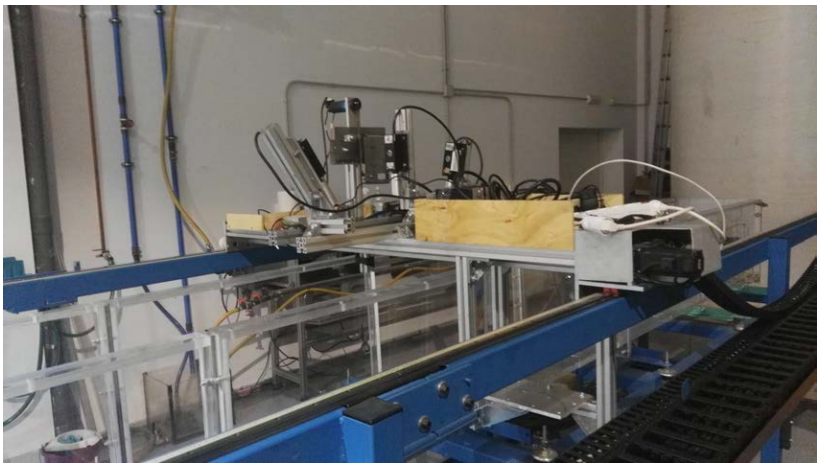

Fig. 2.6 Snapshot of the experiment setup.

We obtained the velocity field using the multi-pass with windows deformation Matlab based software DPIVSoft, developed by Meunier and Leweke [34], that has been tested in rotating flows successfully Lagrange et al. [35], Albrecht et al. [36], García-Ortiz et al. [37].

UNIVERSIDAD DE MÁLAGA

Chapter 3

Lift slope for a flat plate configuration

3.1 Background

One of the simplest models of wings used as a reference for the study of aerodynamics is the rectangular flat plate [9], even tested at ultra-low Reynolds numbers [38]. Since the early 20th century, the flat plate has been used to estimate the lift with bounded parallel walls to mimic the wind tunnel configuration, finding that the corrections of lift for a flat plate and aerofoil are almost identical at small incidence angles [10]. Later, lift corrections at the zero thickness limit were reported for an elliptic cylinder [11]. Interest in flat plates has not diminished since then, and it has been used as a test case for many applications at low *Re* in different areas of research. Some of the most direct applications relate to imitating a pair of winglets [39], to simulate a cascade of blades [2] or to study the stability of fluttering [40]. Others are inspired by the small flyers present in nature, such as comparing rigid and membrane wing models [41], analyzing pitching movements [42], or finding bio-inspired corrugated airfoils [43]. Furthermore, flat plates have also been used to study control-related problems such as the active control for providing lift enhancement [44] or determining the frequency of vortex shedding [45], even at ultra-low *Re* [46, 47]. Moreover, flat plates have also attracted the attention of other branches of engineering and have been used, for example, to analyze the behavior of bridges [48] or to correlate the turbulence intensity and length scale with the unsteady lift force in an atmospheric boundary layer flow [49].

One of the most significant parameters to characterize the aerodynamics of any object is the lift coefficient, C_L and its linear variation with the angle of attack, α. Thus, obtaining the lift coefficient slope ($C_{L\alpha}$) is essential for any wing design. Comparisons between flat plates and other aerofoils such as NACA0012 have been carried out, finding similar lift coefficients at angles of attack equal to 6.5° [9]. It is worth mentioning that we chose a flat plate wing model to study the dependence of $C_{L\alpha}$ for the sake of simplicity since some

UNIVERSIDAD DE MÁLAGA

other symmetrical aerofoils such as NACA0012 would lead to multiple slopes at low *Re* and low angles of attack [9] together with some non-linearities manifested in the form of the presence of negative lift for positive attack angles close to zero [50]. Some authors analyzed the influence on the lift coefficient slope showing that it depends not only on *Re* but also on the aspect ratio for low *Re* in a NACA0012 wing model. Specifically, a correlation was proposed to estimate the lift coefficient slope for each aspect ratio and Reynolds number pair comparing results obtained from several authors [51].

Focusing on the case of a flat plate, the first approximation was theoretically predicted for the case of a two-dimensional object at high *Re*, the so-called potential theory as we introduced on Section 1.3.1. The slope of the lift coefficient,

$$C_{L\alpha} = \left.\frac{dC_L}{d\alpha}\right|_{\alpha_0} \approx a_0, \tag{3.1}$$

being a_0=2π at small angles of attack in the inviscid limit. Kutta-Joukowsky's theorem has been also proved to obtain the circulation experimentally but for lower *Re* [8]. The second correction to this thin-airfoil theory taking into account the wing aspect ratio, and using Prandtl's lifting line (see Section 1.3.4) for a rectangular wing with elliptic loading showed that

$$C_{L\alpha} = \frac{a_0}{\left(1+\frac{a_0}{\pi AR}\right)}, \tag{3.2}$$

instead of a_0 [12, 13]. A rectangular wing with a more general lift loading provides similar results,

$$C_{L\alpha} = \frac{a_0}{\left[1+\frac{a_0}{\pi AR}(1+\delta)\right]}, \tag{3.3}$$

with δ constant of value approximately $\delta \approx 0.024$. This simple approximation takes into account the induced lift, and also that the flow in a finite flat plate remains attached to the leading edge and sides at small angles attack [52]. In fact, it is reported that there are two important ranges of angles of attack differing by the extent of flow separation on the upper surface [53]. At angles of attack below about 8°, flow separation and reattachment occur, and the well-known thin-airfoil theory is adequate for predicting the lift and normal force on the plate. Similar results were noted for other thin airfoil sections. Conversely, for angles of attack above about 8°, flow separation at four sides forms a complex wake structure. Following with other theoretical correlations, and assuming an elliptic span loading

UNIVERSIDAD DE MÁLAGA

Helmbold derived the third equation that is widely used for wing design

$$C_{L\alpha} = \frac{a_0}{\sqrt{1 + \left(\frac{a_0}{\pi AR}\right)^2} + \frac{a_0}{\pi AR}}, \tag{3.4}$$

for a finite flat-plate or low-aspect-ratio straight wings [54]. However, none of these expressions take into account the dependence of the lift with the pair *Re*, *AR* since they are typically used in the limit of high *Re*. The present research provides a general expression for the slope of the lift coefficient for moderate *Re* and for *AR* between 1 and 8.

The curve lift slope $C_{L\alpha}$ depends experimentally at low *Re* on several parameters such as the Reynolds' own value, *AR* [55, 56], roughness surface of the aerofoil ε [14], turbulence intensity $\%I$ [57], thickness, and edge shape of the aerofoil [58, 59], and Mach number *M* [60], among others. The pioneer experiment for a large flat plate wing model (*AR*=14.1) with small and high angles of attack was carried out in 1927 [61]. More recently, the first relevant (experimental) study characterizing the aerodynamics of different flat and cambered plane wings at moderate Reynolds number ($60 \times 10^3 \leq Re \leq 200 \times 10^3$) and low aspect ratio was presented in 2000 by Pelletier and Mueller [1] and it is considered a key reference in this area of study. In this work, they provide results for flat plate aerodynamic coefficients in infinite (2D) and finite wings (3D). This investigation was later extended focusing on the lowest *AR* in Torres and Mueller [62]. Later, other authors have reported more information regarding low-aspect-ratio cases at low *Re* not only experimentally but also through numerical simulations [63, 43]. Other authors have pointed out experimentally how the maximum lift decreases as *AR* increases [64, 59]. Finally, Ananda *et al.* [65] measured the aerodynamic coefficients of different rectangular and tapered plate wing models at low Reynolds numbers taking into account the three-dimensional phenomena in the range of *AR* between 2 and 5, finding important differences with the two-dimensional case.

The wide range of applications for smaller dimensions makes the understanding of the aerodynamics at low *Re* numbers crucial. Due to the importance of the lift coefficient in general and of the slope of the lift coefficient in particular, we have designed different experiments to be able to propose a correlation taking into account not only *AR* but also *Re* for the simplest model of an airfoil, a flat plate. Using this correlation would facilitate the dimensioning of wings for aerial vehicles with working conditions in the low *Re* regime. Therefore, this work could be the base to extend the results to other more realistic aerodynamic profiles.

UNIVERSIDAD DE MÁLAGA

Table 3.1 Measured turbulence level using Hot-Wire Anemometer for each Reynolds number used for the study.

Re	$40e3$	$80e3$	$120e3$	$160e3$	$200e3$
Turb. (%)	0.8	0.5	0.35	0.35	0.35

3.2 Experimental arrangement

We have measured the lift coefficient in rectangular flat plates in the pre-stall region and small values of geometric thickness to chord ratio (t/c=0.0133), along with low turbulence levels under subsonic conditions (Mach numbers below 0.06). The experimental tests were performed using rounded rectangular aluminum plates in the closed low-speed wind tunnel of the Micro aerial Vehicle Laboratory at the University of Malaga.

The wind tunnel has a 4 m long closed test section, 1x1 m is cross-section and free stream velocity can vary from $U_\infty = 4\ to\ U_\infty = 40\ m/s$, (in this work, 23 m/s have been reached for the highest Reynolds number). Each experiment was characterized by its chord-based Reynolds number Re, defined as

$$Re = \frac{U_\infty \cdot c}{\nu}, \tag{3.5}$$

where ν is the kinematic viscosity at the wind tunnel conditions. We used rectangular plates with chord of 150 mm and thickness of 2 mm. The length of the profiles, l, varies from 75 mm to 600 mm, so the aspect ratio $AR = 2l/c$ is between 1 and 8. The turbulence intensity has been measured using hot-wire anemometry obtaining values of turbulence intensity lower than 0.8% for all the studied Reynolds (see Table 3.1).

The aerodynamic forces were measured using a precise six axis force/torque sensor ATI FTD-GAMMA SI-32-2.5 sensor of accuracy $\pm 0.006\ N$, whose main characteristics were reported in chapter 2. This force sensor was fixed to a stepper motor to control the angle of attack, and the assembly has been screwed to the floor outside the wind tunnel to avoid structural vibration noise that would affect the walls of the test section. The plate was attached firmly to an aluminum base, which was joined to the top of the force sensor and leveled with the floor of the wing tunnel. A scheme of the experimental setup is shown in Fig. 3.1.

To use force measurements to calculate lift and drag coefficients, some considerations are needed. Since the z axis of the transducer has the direction of the gravity force, the aerodynamic forces only act in the (x, y)-plane. The wing chord was aligned with the x-axis of the force sensor and the system is turned rigidly with it, thus creating a local coordinate system centered in the wing. To obtain the forces in a global coordinate system aligned

UNIVERSIDAD DE MÁLAGA

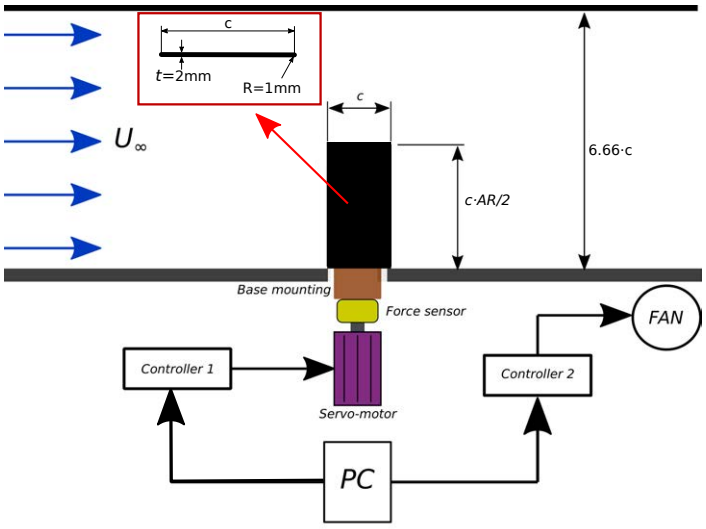

Fig. 3.1 Experimental setup scheme. The inset represents the cross-section of the flat plate to highlight the rounded leading and trailing edges.

with the wind direction, (that is to say, to compute the lift and drag forces), the following transformation was used:

$$F_{xD} = F_x \cos(\alpha) - F_y \sin(\alpha), \tag{3.6}$$

$$F_{yL} = F_x \sin(\alpha) + F_y \cos(\alpha). \tag{3.7}$$

In these equations, we have already subtracted the offset of the force signals, F_x and F_y. The non-dimensional forces in the global coordinate system are given by

$$C_D = \frac{2F_{xD}}{\rho U_\infty^2 A}, \qquad C_L = \frac{2F_{yL}}{\rho U_\infty^2 A} \tag{3.8}$$

where ρ is the air density at wind tunnel conditions, and A is the aerodynamic area as a rectangular model $A = c^2 \cdot AR/2$ (see Fig. 3.1).

A servomotor at 10000 steps per revolution controlled the angles of attack during the experiments allowing small variations in α. The measurements were taken with steps of 1°. For each angle of attack, the force was obtained by collecting data for 8 seconds. Each experiment was repeated three times for each range of angles of attack to check repeatability and to obtain the average value and standard deviation of lift and drag curves with α.

We did not observe any relevant tunnel blockage effects since it had a maximum value of 1.36% for $AR = 8$. The angle of attack, lift and drag corrections due to curvature streamlines are computed using the formulas provided by Barlow *et al.* [66] and by McAlister and Kenneth [67]. The angle correction is almost zero and thus the lift corrections. The drag

UNIVERSIDAD DE MÁLAGA

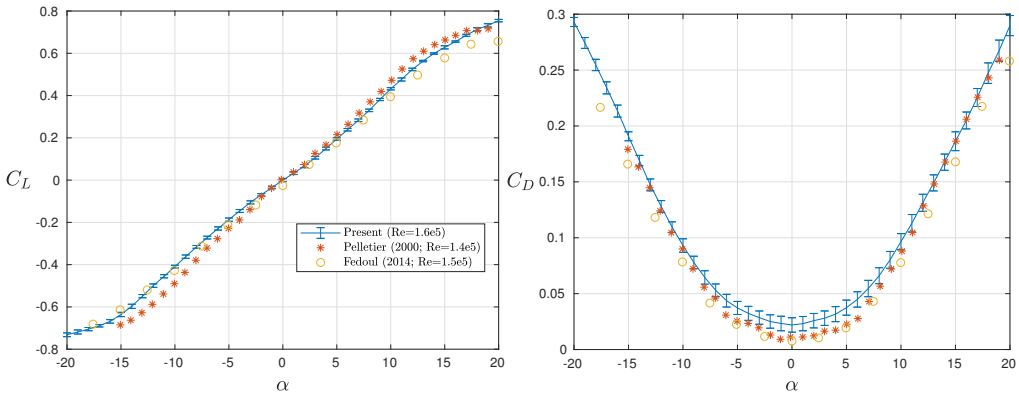

(a) (b)

Fig. 3.2 Validation of force measurements for a flat plate at $Re = 160 \times 10^3$ and $AR = 2$ comparing with Pelletier & Mueller [1] at $Re = 140 \times 10^3$ and Fedoul *et al.* [2] 150×10^3.

correction is found to be at most 1% of its value around $\alpha = \pm 15°$ and decreasing as the angle of attack is decreasing. These values are consistent with the junction study presented by Bernstein & Hamid [68] reported also in Malik [69] for the case of a NACA0015 but in that case the influence of the corrections are amplified due to the higher *Re*. In our case, all these corrections are so small that were neglected.

3.3 Experimental measurements

3.3.1 Validation

A flat plate of $AR = 2$ at $Re = 160 \times 10^3$ was used to compare the results with the well-known, established results of Pelletier and Mueller [1]. In Fig 3.2, lift and drag coefficients versus the angle of attack are compared with those provided by Pelletier and Mueller [1] for a flat plate of $AR = 2$ at $Re = 140 \times 10^3$ finding good agreement with our results. Additionally, data from Fedoul *et al.* [2] with a slightly higher *Re* (nearest to our value) are also superposed as second validation.

3.3.2 Results

To better understand each experiment, we depict in Fig 3.3 how the force $F_y(N)$ and C_L evolves in time for $\alpha = 7°$, $AR = 8$, and $Re = 200 \times 10^3$. These results correspond to the raw data obtained from the sensor during eight seconds at 1000Hz. We observe that the oscillations in the measurements do not correspond to a square (or step) signal in the range

UNIVERSIDAD DE MÁLAGA

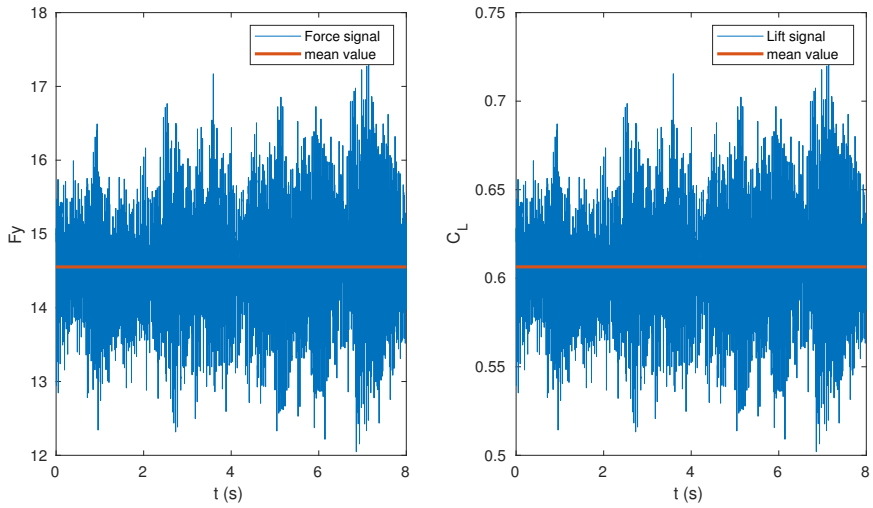

Fig. 3.3 Force signals for $\alpha = 7°$, $AR = 8$, $Re = 2e5$

of $\pm 0.006N$ which is the accuracy of the sensor, but to a noisy signal. Note also that using our data and computing the standard deviation of each individual experiment, the minimum required sample points to obtain a 0.999 confidence probability in the averaged value is around 400 samples, see [66], and we are using 8000 sample points and thus the noise effect is negligible.

We performed experiments to measure C_L on flat plates for different angles of attack, Re, and AR. Figs. 3.4(a)-(e) display C_L for five different Re in the range of $40 \times 10^3 \leq Re \leq 200 \times 10^3$. Each of them contains results corresponding with four different AR in the range of $1 \leq AR \leq 8$ with a resolution $\Delta\alpha = 1°$.

For small AR, the value of C_L is increasing with approximately the same rate of change for every angle of attack, as shown in Fig. 3.4. However, for bigger AR, there exist two different slopes, a steeper one for the range of small angles of attack and a softer one for the bigger angles of attack. See for example Fig. 3.4(a) focusing on $AR = 8$, purple curve, where the change in slope is evident around $\alpha \approx \pm 8°$. Also, one can observe that the measurements show a more significant error for the case of $Re = 40 \times 10^3$ and small AR since the forces in these cases are close to the lower limit of our measuring equipment.

Since the curves are approximately linear in the range of small angles of attack, we can calculate their slope, $C_{L\alpha}$, using a linear fit as proposed by [51]. Therefore, we calculate the slope for the range of smaller α ($-7° \leq \alpha \leq 7°$) for each Re, AR pair. Note that in this range, the data is so linear that the same value of $C_{L\alpha}$ is obtained when computing a second-degree polynomial approximation to the lift and considering $C_{L\alpha}$ to be the linear coefficient as reported by [62]. Fig. 3.5(a) shows all the computed $C_{L\alpha}$ with respect to Re

UNIVERSIDAD DE MÁLAGA

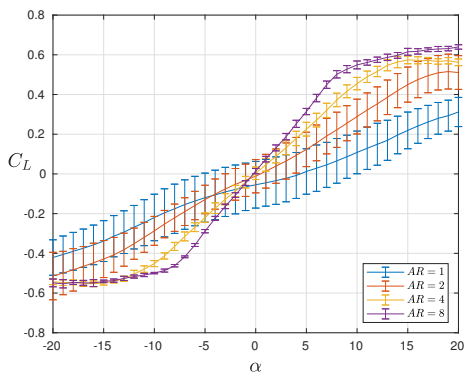

(a) $Re = 40 \times 10^3$

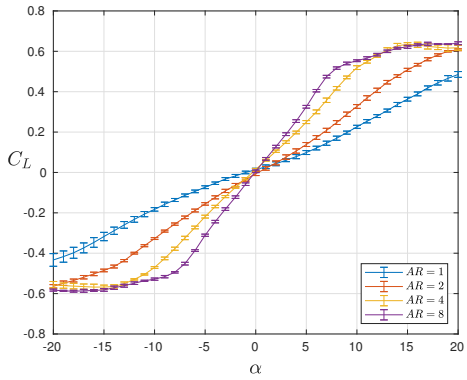

(b) $Re = 80 \times 10^3$

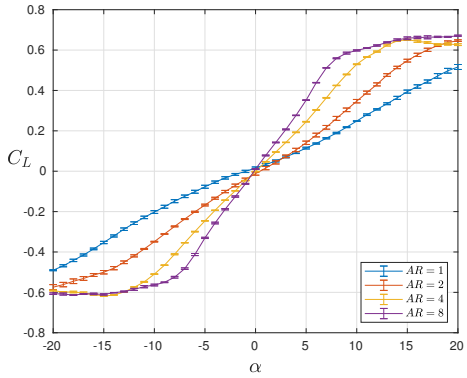

(c) $Re = 120 \times 10^3$

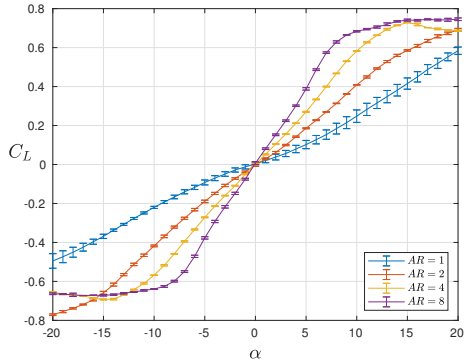

(d) $Re = 160 \times 10^3$

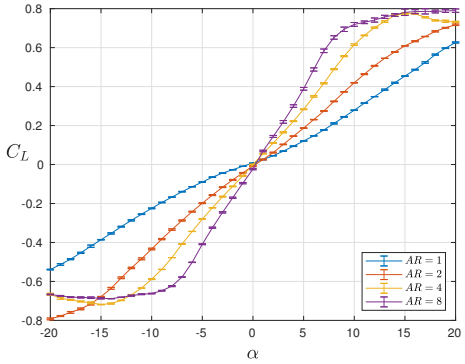

(e) $Re = 200 \times 10^3$

Fig. 3.4 Variation of C_L versus α for different AR for the following cases: (a) $Re = 40 \times 10^3$,(b) $Re = 80 \times 10^3$, (c) 120×10^3, (d) $Re = 160 \times 10^3$, (e)$Re = 200 \times 10^3$.

UNIVERSIDAD DE MÁLAGA

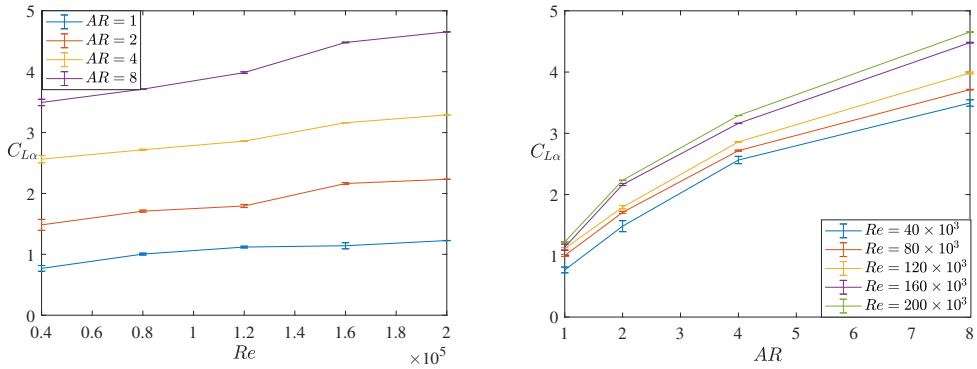

(a) (b)

Fig. 3.5 Variation of the measured $C_{L\alpha}$ with respect to Reynolds number (a) and aspect ratio (b).

along with the errors based on the standard deviation of three experiments. We can observe how $C_{L\alpha}$ increases with the aspect ratio and with Re, but the influence of Re on the variation of $C_{L\alpha}$ is less noticeable in the figure for the smallest Re values. To visualize better this influence, Fig. 3.5(b) represents all the measured slopes with respect to AR. The increment of $C_{L\alpha}$ when increasing the aspect ratio and Re is clear. The same weak influence of the Reynolds numbers on $C_{L\alpha}$ and the growth of $C_{L\alpha}$ with AR has been reported previously by Ananda *et al.* [65], showing a precise experimental methodology again.

3.4 Correlation between $C_{L\alpha}$, aspect ratio and Re

As mentioned above, the lift slope is a key criterion for any initial wing design. Therefore, we aim to find a correlation to obtain $C_{L\alpha}$ as a function of the aspect ratio and the Reynolds number. The literature presents several studies obtaining this slope for specific AR and Re pairs but, to the best of our knowledge, no one has offered a correlation including both parameters. As mentioned in the background section of this chapter, there are several correlations for the lift slope depending only on the AR and being valid for high Re. Following the idea of Prandtl's lifting line but including the influence of Re for moderate values, we propose the following correlation:

$$C^*_{L\alpha} = \left(\frac{2\pi}{1+\alpha_1 * AR^{-1}}\right)\left(\frac{\alpha_2}{1+10^6/Re}\right)^{1/5} \tag{3.9}$$

with $\alpha_1 = 5.21$ and $\alpha_2 = 14.61$.

UNIVERSIDAD DE MÁLAGA

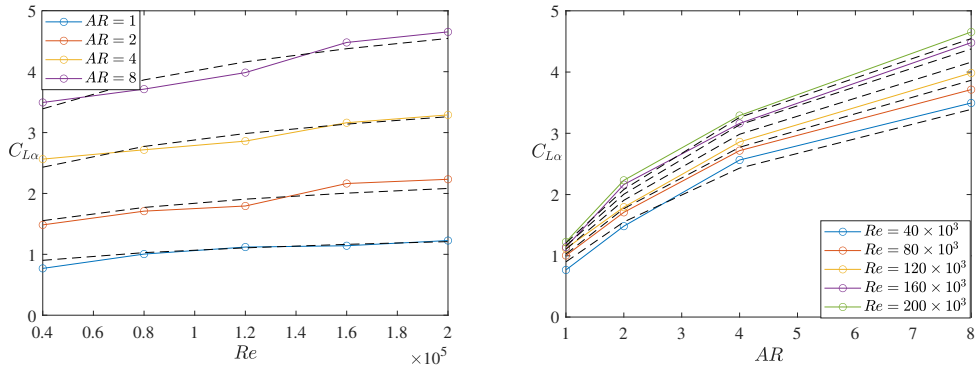

(a) (b)

Fig. 3.6 Variation of the measured $C_{L\alpha}$ with respect to Reynolds number (a) and aspect ratio (b). Superposed in dashed lines the computed $C_{L\alpha^*}$ values using the correlation in equation (9).

Fig. 3.6 represents in dashed lines the computed $C_{L\alpha^*}$ using the correlation superposed with the measured values shown in Fig. 3.5 to follow the trends of the correlation in equation (3.9).

To quantify the accuracy of the proposed correlation, Fig. 3.7(a) displays $C_{L\alpha}$ obtained directly as the slope for every Re and AR together with the computed slope, using the proposed correlation, $C^*_{L\alpha}$, showing excellent agreement. Fig. 3.7(a) also presents two red dashed lines, which represent the confidence interval of 5% to help the visualization. When computing the error for each Re, AR, and averaging them, we obtain a mean error of 4.1%. Thus, we can conclude that the proposed correlation is a good approximation for $C_{L\alpha}$ for a flat plate in our study range.

Furthermore, we have analyzed the errors for each Re, AR pair individually. Fig. 3.7(b) shows the relative error for each $C^*_{L\alpha}$ when comparing it with $C_{L\alpha}$ directly measured in each experiment ($e_1 = |\frac{C^*_{L\alpha} - C_{L\alpha}}{C_{L\alpha}}|$). It is noticeable how the accuracy of the correlation, even though is good for every value, it is not consistent for all the aspect ratios having peaks for some Re, AR pairs and extremely good agreement for some others (including some values with an error below 2%). Note that there is one value showing a relatively high error for $Re = 40 \times 10^3$ and $AR = 1$, but that is also the value with more uncertainties in the measurements. If that measured value is neglected, the average error would be even smaller. In general, the error decreases as AR and Re increase.

Focusing on the literature for small aspect ratio wings, we could also consider the idea of computing a correlation related with the value of $C_{L\alpha}$ proposed by Helmbold [54] for a finite

UNIVERSIDAD DE MÁLAGA

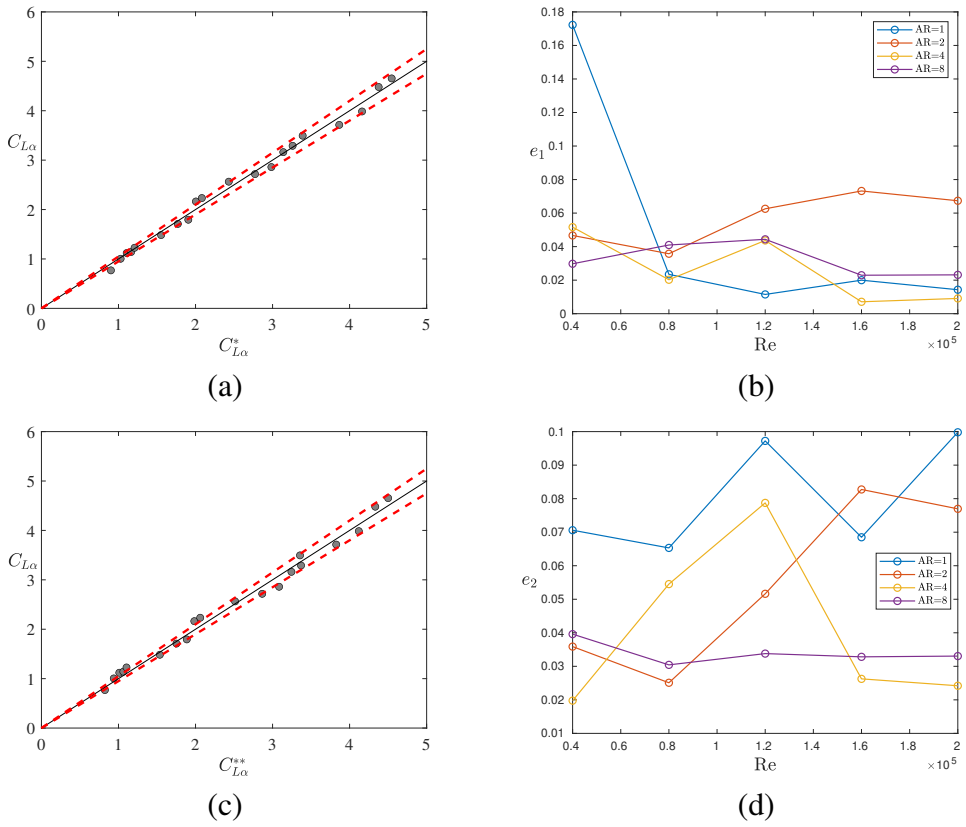

Fig. 3.7 Computed $C^*_{L\alpha}$ and $C^{**}_{L\alpha}$ using the correlations in equations (9)-(10) versus measured $C_{L\alpha}$ obtained directly as the slope for different Re and AR, in (a)-(c) respectively. Relative error when computing $C^*_{L\alpha}$, $e_1 = |\frac{C^*_{L\alpha} - C_{L\alpha}}{C_{L\alpha}}|$, (b) and relative error when computing $C^{**}_{L\alpha}$ (d) for each Re, AR value.

flat-plate low-aspect-ratio straight wings, see equation (3.4). Therefore, we provide a second correlation of the form of:

$$C^{**}_{L\alpha} = \left(\frac{\alpha_1}{\sqrt{1 + [\alpha_1/(\pi AR)]^2} + \alpha_1/(\pi AR)} \right) \left(\frac{\alpha_2}{1 + 10^6/Re} \right)^{1/5} \tag{3.10}$$

and fitted the results with $\alpha_1 = 3.79$ and $\alpha_2 = 44.53$.

Fig. 3.7 (c) displays the comparison between the estimated and measured $C_{L\alpha}$ obtaining a good agreement. In fact, this correlation is only slightly worst than the previous one, with an average error of 5.23%. However, when looking at the details of the error for each Re, AR pair, see Fig. 3.7(d), we can appreciate how the error is less consistent for each AR. Furthermore, for the highest Re, the errors of the two smaller AR are bigger than for $AR = 4$ and $AR = 8$. Therefore, for the following, we have used the correlation defined by eq. (3.9).

UNIVERSIDAD DE MÁLAGA

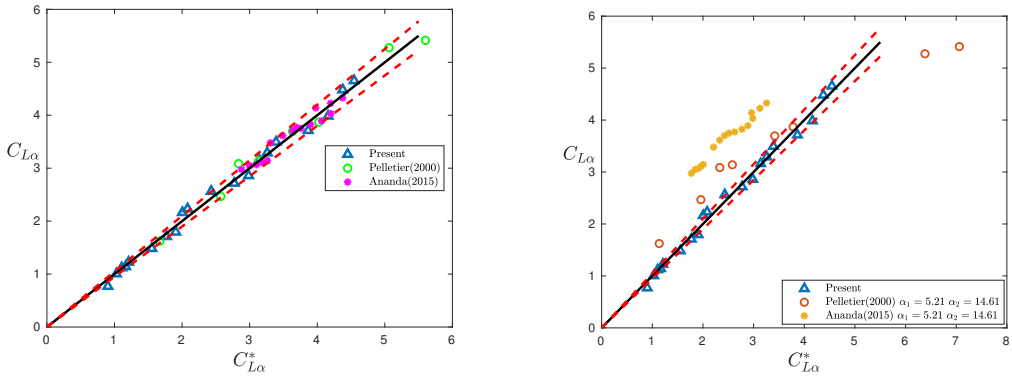

(a) (b)

Fig. 3.8 Computed $C_{L\alpha^*}$ using the correlation in equation (9) with (a) their corresponding parameters α_1 and α_2 for each author and (b) $\alpha_1 = 5.21$ and $\alpha_2 = 14.61$ versus the measured $C_{L\alpha}$ obtained directly as the slope for different *Re* and *AR* for different authors.

3.5 Comparison with previous results presented in the State of Art

We have presented a correlation in the range of $40 \times 10^3 \leq Re \leq 200 \times 10^3$ and $1 \leq AR \leq 8$ derived from our own measurements. There are two other studies in literature by Pelletier and Mueller [1] and Ananda *et al.* [65] which contain several measured values in the same range of *Re* and *AR*. We have used our correlation to fit their data and we have obtained $\alpha_1 = 2.35$ and $\alpha_2 = 4.58$ for Pelletier and Mueller [1] and $\alpha_1 = 2.20$ and $\alpha_2 = 11.15$ Ananda *et al.* [65]. Fig. 3.8(a) represents $C_{L\alpha}$ versus $C^*_{L\alpha}$ for both of those studies together with our data. In all cases, a good agreement is clear. Thus, we can conclude that all of them follow the same kind of dependence with *AR* and *Re*. Results of computed values using our experimental parameters $\alpha_1 = 5.12$ and $\alpha_2 = 14.61$ are shown for quantitetive comparison in Fig. 3.8(b). The differences in the correlation parameters are expected since the actual value of $C_{L\alpha}$ slightly depends on some other characteristics such as the roughness, thickness and edge shape of the aerofoil of the wing that not considered explicitly in the correlation. These characteristics are different in each of the three studies. For example, our flat plates have both endings rounded equally, but the plates considered in Pelletier and Mueller [1] have rounded leading edge and tapered edge and the ones in Ananda *et al.* [65] are both rounded but not symmetrically. See table 3.2 for a summary of the other main characteristics of each study. Note also that the study of Pelletier and Mueller [1] includes 2D values, outside our study range. We have also used our correlation to analyze those values corresponding to the higher circle values in Fig. 3.8 (a), and it correlates them correctly.

UNIVERSIDAD DE MÁLAGA

Table 3.2 Main parameters from various studies.

Study	thickness t/c	%I of turbulence	Re	AR
Present	0.0133	$I\% \leq 0.8$	$40-200\times10^3$	$1 \leq AR \leq 8$
Pelletier and Mueller (2000)	0.0193	$I\% \leq 0.05$	$80-140\times10^3$	$1 \leq AR \leq \infty$
Ananda *et al.* (2015)	0.026	$I\% \leq 0.1$	$60-160\times10^3$	$2 \leq AR \leq 5$

3.6 Conclusions

We have measured the lift coefficient for several flat plates with different aspect ratios varying the Reynolds number in a range of $40\times10^3 \leq Re \leq 200\times10^3$ and the aspect ratio $1 \leq AR \leq 8$. For small angles of attack, the variation of the lift coefficient is linear and, therefore, it can be defined simply by knowing the slope of the function $C_{L\alpha}$. We have proposed a correlation to provide this slope for different Re and AR that contains two free parameters: α_1, α_2. The proposed correlation contains two parts, one that modifies the value of $C_{L\alpha}$ taking into account the use of finite wings and that behaves similarly to the results predicted by Prandtl's lifting line theory. The second part only depends on the Reynolds number. The proposed correlation is able to predict the value of $C_{L\alpha}$ within an average error of 4.1% in the studied range. Lastly, we have shown how we could extrapolate the values of other authors following the same kind of fitting. This correlation provides accurate results, even outside the AR study range.

We believe that this same type of semi-empirical correlations can be extended to be used in more realistic wing profiles, and in addition, are capable of describing its behavior up to the limit situations of 2D flow ($AR \to \infty$) in some cases. Finally, the dependence of the correlation with respect to the Reynolds number is completely heuristic and leaves open the possibility of obtaining physical scale laws for the calculation of this slope dependence with respect to Re, together with a plausible theoretical explanation of the exponent 1/5.

UNIVERSIDAD DE MÁLAGA

UNIVERSIDAD
DE MÁLAGA

Chapter 4

Non-linearity in a NACA0012 wing model

4.1 Background

NACA0012 [70] is a standard test case for wing profiles and therefore focuses many articles describing different details of the flow around it in the *Re* regime $\mathscr{O}(10^4 - 10^5)$. Some of the most relevant characteristics analyzed in recent studies regarding NACA0012 are: control of the downstream flow [71–75], influence of the turbulence intensity [76, 77], aerodynamic load responses of airfoils undergoing dynamic stall [78–80] or the effects of an oscillatory motion [81–84] together with the study of trailing vortices [85–88, 37] and its stability [89–92].

Another characteristic observed in this range of *Re* is the change in sign of the lift coefficient for small angles of attack. Mueller and Batill [93] was the first team to describe a negative lift coefficient in a wing model. Specifically, their experiments were performed using a NACA $66_3 - 018$ [94] aerofoil at $Re = 130 \times 10^3$. This effect also exists in the NACA0012 profile, but the experimental difficulties associated with the small forces and small turbulence involved in the problem has prevented the scientific community from seeing this effect in many pieces of research. Note also that this effect only occurs over a minimal range of angles of attack, and that the resolution when varying this parameter was not sufficient to capture the non-linear effect in some of the published studies.

Nevertheless, only a few articles described this effect in a NACA0012 profile. Ohtake *et al.* [4] experimentally studied the non-linearity in the lift coefficient developed at low angles of attack for low and moderate Reynolds numbers using a low-speed, low turbulence wind tunnel. They showed that this non-linearity can inverse lift's sign at very low angles of

UNIVERSIDAD DE MÁLAGA

attack. Later, Yonemoto *et al.* [95] numerically investigated the negative lift observed in the experiments by Ohtake *et al.* [4], and proposed that a reversed flow at the trailing edge of the upper surface could accelerate the corresponding boundary layer at the lower surface, thus producing the negative lift.

In 2017, Tank *et al.*[3] observed both experimentally and numerically the sign switch in the lift coefficient. When comparing their results with other studies, they have pointed out the lack of agreement of the scientific communities on some details of the flow features observed in our range of *Re* numbers due to the associated difficulties described above. However, they suggested that careful experiments with the most smooth and symmetric aerofoil with sufficient thickness, will show a negative lift coefficient for certain *Re*, depending also on the surface finish and the level of environmental turbulence. After presenting their results, they proposed a physical explanation of this phenomenon based on the displacement of the separation point.

It is worth to mention that aside from the difficulties of capturing this effect experimentally, reproducing it numerically is also intricate (see [96] for a state of the art review about hybrid RANS-LES methods for turbulent flows and its applications). For example, Winslow and his collaborators were able to capture the non-linear effect for small angles of attack by RANS simulations, but they have not predicted the negative lift [97]. They also identified the need for further assessment of turbulence models for low-Reynolds-number flows. In a very recent paper, Pranesh *et al.* [98] reported a negative lift coefficient when performing two-dimensional numerical simulations on a NACA0012 wing using a laminar-turbulent transition model. They have focused their detailed explanation of the negative lift over the trailing edge of the wing.

To investigate the negative lift, we have conducted experimental and numerical investigations of the lift coefficient at small angles of attack using Reynolds numbers in the range $\mathscr{O}(10^4 - 10^5)$ for three semi-aspect ratios of the wing model between 1 and 3. First, we describe in what range of *Re* and aspect ratio the non-linearity and negative lift are experimentally perceptible and compare our results with the literature. Second, we run numerical simulations to analyze the physical mechanism behind this negative lift. Unlike other studies that explain this negative lift paying their attention on the boundary layer separation in the upper surface and subsequently in the wake generated behind the trailing edge, we propose a novel physical explanation based on the pre-alignment of the upstream flow that affects the leading edge due to the change of sign in the overall circulation over the airfoil.

UNIVERSIDAD DE MÁLAGA

Table 4.1 Measured turbulence level using Hot-Wire Anemometer for each Reynolds number used for the study.

Re	$4e4$	$5e4$	$6e4$	$8e4$	$9e4$	$1.2e5$
Turb. (%)	0.35	0.35	0.35	0.25	0.25	0.23

4.2 Experimental Arrangement

We mainly employed the same setup described in Chapter 3 but using NACA0012 instead of flat plates. These NACA0012 wing models are made of aluminum with a very polished surface. The length of the profiles varied from 100 to 300 *mm*, so the semi-aspect ratio $sAR = l/c$ was between 1 and 3. We have tested the NACA 0012 wing models for $Re = 40 \times 10^3$, $Re = 90 \times 10^3$ and $Re = 120 \times 10^3$ in a range of angles of attack, α. The turbulence level of the wing tunnel measured with Hot-Wire anemometer was always below 0.5% (see table 4.1).

To check repeatability and obtain the standard deviation of lift and drag curves with α, each experiment was repeated six times for each range of angles of attack. In particular, three repetitions were performed by increasing and decreasing the angle of attack, thus following the same strategy given in Tank *et al.*[3]. Finally, we did not observe any relevant tunnel blockage effects since it had a maximum value of 0.8% for sAR=3.

4.3 Numerical setup

The incompressible and bi-dimensional (2D) equations of the flow around the NACA0012 airfoil are discretized and solved using a turbulent model with the commercial package Ansys®-Fluent v19.1, a finite volume-based solver. All simulations are performed using a transient, pressure-based, coupled solver with absolute velocity formulation. The least-squares cell-based method is applied to compute the gradients of the transport quantities on the cell faces. A second-order method is used for the spatial discretization of the pressure term, and a second-order upwind for the continuity, momentum, and $k-\omega$ transport equations. The explicit relaxation factors of pressure and momentum are set as 0.75, whereas the under-relaxation number of 0.9 is applied to turbulence quantities. The temporal derivatives are discretized by using a second-order implicit formulation. Each time step is considered converged when the absolute residual values are smaller than 10^{-3}, 10^{-5}, and 10^{-7} for continuity, momentum, and turbulence quantities, respectively. The unsteady simulations are started from the rest (pressure and velocity equal to zero).

UNIVERSIDAD DE MÁLAGA

Table 4.2 Details of the three meshes for the grid convergence study. $Re = 40 \times 10^3$ and $\alpha = 2^o$. Temporal evolutions of 90 time units and average values calculated over the last 30.

	#cells	profile's #cells	1st cell height (mm)	$\overline{C}_L$	y^+_{max}
#1	152345	250	0.4	0.186	1.63
#2	284885	500	0.2	0.178	0.81
#3	509819	1000	0.1	0.173	0.39

In particular, the turbulence is modeled with the four equations of the transition (γ-Re_θ) SST model. This model was developed for transition flows. It is a combination of SST k-ω additionally coupled with intermittency γ and transition onset Reynolds number, Re_θ, which is the critical Reynolds number where the intermittency starts. Therefore, four transport equations are solved: the first two equations are similar to SST k-ω (see Langtry *et al.* [99]), and the equations for intermittency and transition momentum thickness Reynolds number were developed in Langtry *et al.* [100] and Malan *et al.* [101]. This model was successfully used in recent papers concerning NACA profiles [102], including a study for our precise geometry and range of Re and α. Tank *et al.* [3] found that the transition SST model correctly predicts both the lift and drag for a NACA0012 airflow with $Re = 50 \times 10^3$ and attack angles below 8°. Additionally, Gorji *et al.* [103] used direct numerical simulations to compare different turbulence models for the case of unsteady flows and low Reynolds numbers, reporting that γ-Re_θ is one of the few models suitable for unsteady flow. Note also that we are simulating very polished surfaces which assure a hydraulic smooth regime.

The analyzed airfoil has a unitary chord, c, and its angle of attack angle α is counted positively clockwise, see Fig. 4.1(a). The airfoil is placed into a rectangular computational domain, as shown in Fig. 4.1(b). This domain is sufficiently large to impose the inlet/outlet boundary conditions without perturbing the flow close to the wing, as it was demonstrated by Tank *et al.* [3]. Note that the inlet velocity U is horizontal, i.e., it is aligned with the x-axis ($\hat{i}$) of the absolute frame $0xy$ not with the x-axis of the relative frame $0_1x_1y_1$ which is aligned with the chord ($\hat{i}_1$), see Fig. 4.1.

To validate the accuracy of the grid, we have performed a sensitivity analysis using three meshes. Table 4.2 shows their main characteristics. The table also includes the values of the average lift coefficient with an angle of attack of 2° and a $Re = 40 \times 10^3$, which is the most unfavorable case analyzed in the present study. Although the relative error in the lift between meshes #2 and #3 is below 3%, the mesh #3 guarantees a y^+ substantially below 1. Having $y^+ < 1$ is a necessary condition to reproduce with accuracy the velocity profile in the viscous sublayer in order to correctly capture the adverse pressure gradients. Therefore, we

UNIVERSIDAD DE MÁLAGA

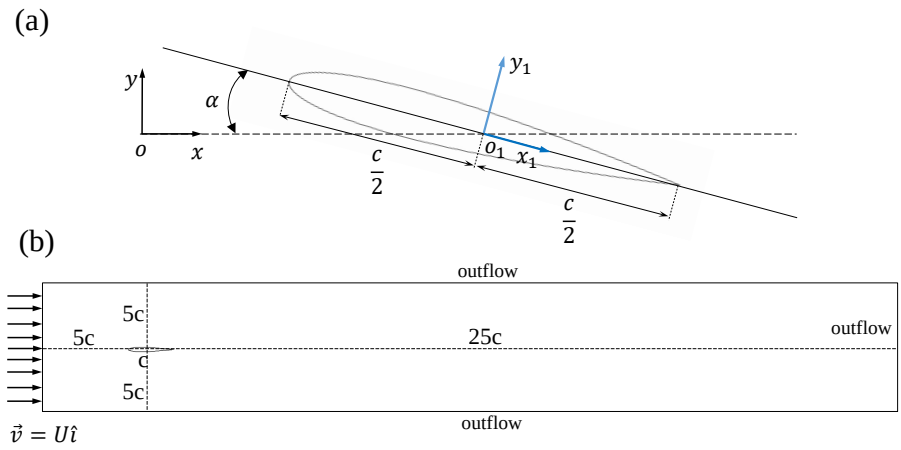

Fig. 4.1 Sketch of the NACA 0012 airfoil and relevant quantities (a). Computational domain and boundary conditions (b).

have selected mesh #3 to perform all the computations included in the following sections. Different details of this mesh are included in Fig. 4.2. Notice that special care was taken to build the mesh close to the trailing edge. This quasi-structured mesh of quad-cells has a good mesh quality with a maximum skewness below 0.65.

To perform the simulations in Fluent we set: $U = 1\ m/s$ with a turbulence intensity 0.5%, $c = 1\ m$ and $\rho = 1\ kg/m^3$. Thus, for a given Reynolds number, $Re = \rho U_c/\mu$, the dynamic viscosity is directly $\mu = 1/Re$ kg/(ms). Finally, the dimensionless time step was set $U\Delta t/c = 5 \times 10^{-4}$ to keep the Courant number below 5 in all simulations.

4.4 Experimental results

To validate the experiment setup avoiding the discrepancies found between different experimental results on NACA 0012 profiles, we started testing the wind tunnel measurements using a flat plate that has a well-known solution. In order to check repeatability and obtain the standard deviation of lift and drag curves with the angles of attack α, each experiment was repeated three times. Fig. 4.3 shows the lift and drag coefficient compared with those reported by Pelletier [1] for a flat plate of $sAR = 3$ at $Re = 80 \times 10^3$ finding an excellent agreement.

After verifying the accuracy of the wing tunnel, we have conducted experiments around the NACA 0012 to analyze the non-linearity of the lift for the small angles of attack, α. We have first measured the lift coefficient for $Re = 40{\pm}0.5{\times}10^3$, $90{\pm}3.2{\times}10^3$, and

UNIVERSIDAD DE MÁLAGA

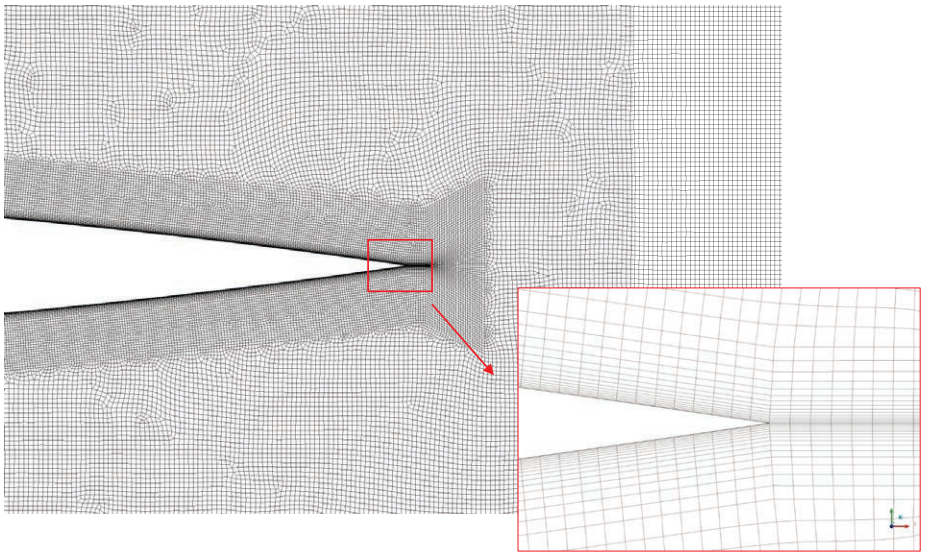

Fig. 4.2 Quasi-structured mesh#3 around the profile with a zoom of the trailing edge region.

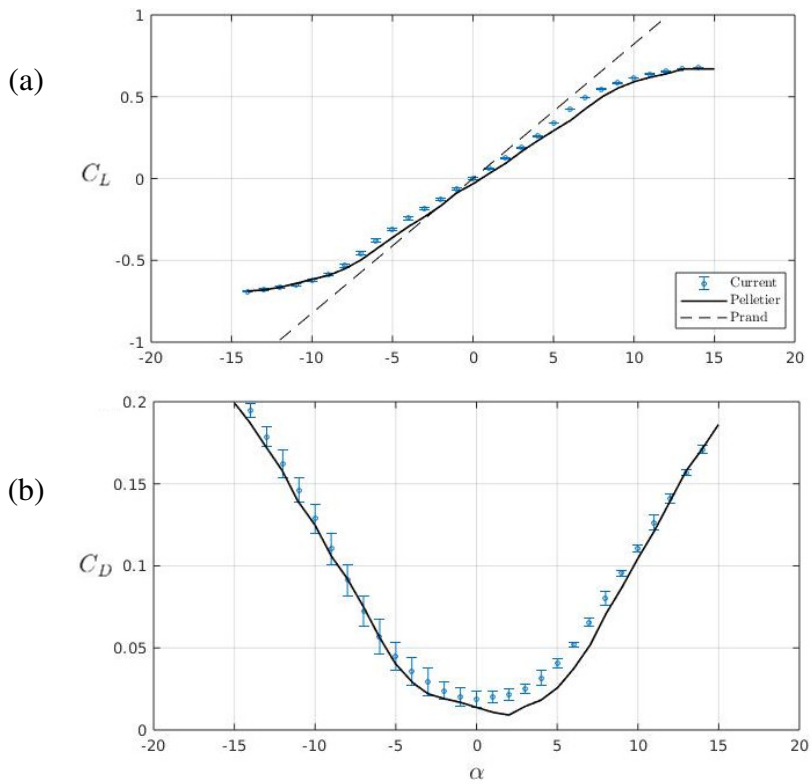

Fig. 4.3 Validation of force measurements comparing with Pelletier & Mueller [1] for a flat plate at $Re = 80 \times 10^3$ and $sAR = 3$ using both lift (a) and drag (b) coefficients.

UNIVERSIDAD DE MÁLAGA

(a)

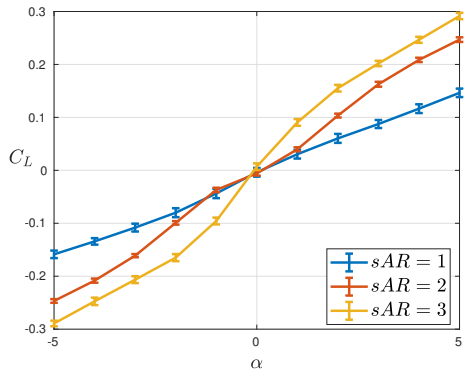

(b)

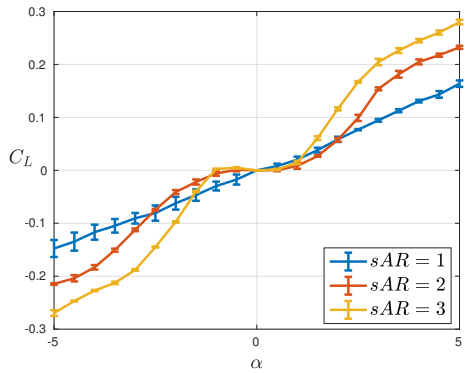

Fig. 4.4 Lift coefficient (C_L) by means of angle of attack for a NACA 0012 at $Re = 90 \times 10^3$ (a) and $Re = 40 \times 10^3$ (b) with semi-aspect ratio sAR from 1 to 3.

UNIVERSIDAD DE MÁLAGA

$120 \pm 4 \times 10^3$ using an angle resolution of at most $\Delta\alpha = 1°$, to corroborate that the non-linearity only appears for a certain range of Re. For $Re = 90 \times 10^3$, see Fig. 4.4(a), there is no evidence of the non-linearity that produces the change of sign in C_L. A similar (not shown) result was obtained for $Re = 120 \times 10^3$. This dependence of C_L as a function of α is consistent with the range of Re at which some other authors have reported seeing the non-linearity. For example, Ohtake et al. [4] detected experimentally the non-linearly in the range of $25 \times 10^3 \leq Re \leq 70 \times 10^3$ and Yonemoto *et al.* [95] numerically reported a range $30 \times 10^3 \leq Re \leq 70 \times 10^3$ or Pranesh *et al.* [98] a range of $20 \times 10^3 \leq Re \leq 75 \times 10^3$. Note that in some of the previous lift studies conducted in these ranges of Re the resolution $\Delta\alpha$ was not enough to capture the non-linear effect. Thus, their lack of reporting the effect does not contradict its existence. The lift performance change dramatically for $Re = 40 \times 10^3$, see Fig. 4.4(b), where the non-linearity is evident and the change of sign is subtly visible. Note that the non-linear effect does not appear in the case of $sAR = 1$, but for $sAR = 2$ or higher. For $sAR = 3$, the non-linearity is more evident, and we measured negative lift coefficients. Having negative lift coefficients for the highest sAR suggests that the change in sign is mainly a bidimensional effect. In fact, Ohtake *et al.* [4] reported the existence of experimental negative lift using a NACA 0012 (2D) profile while our results or those given by Tank *et al.* [3] correspond to a (3D) wing model. Therefore, we have experimentally analyzed in detail our highest aspect ratio and performed two-dimensional numerical simulations to explore the physics behind this effect further.

Fig. 4.5 represents the experimental results obtained for $Re = 40 \times 10^3$ and semi-aspect ratio $sAR = 3$. For this high-resolution acquisition, we report α from $-1.75°$ to $1.75°$ in increments of $\Delta\alpha = 0.25°$ going in the positive direction in red and going backwards in blue. We can see how there exists a small hysteresis when performing the experiments with a small deviation of around $0.1°$. Nevertheless, the switch in the sign of C_L is noticeable in both directions and more obvious by the eye in the negative direction.

4.5 Numerical results

In Fig. 4.6 we compare our numerical results with the only experimental published results that were able to capture the negative lift, Tank *et al.* [3] and Ohtake *et al.* [4]. There exists a good agreement between results. In all the cases, the lift becomes negative for angles of attack $\alpha \leq 1°$ having its minimum value around $\alpha = 0.5°$. The graphs also agree on the tendency of C_L when increasing the angle of attack. Note that the Re number considered in our case is $Re = 40 \times 10^3$ whereas it is $Re = 50 \times 10^3$ in their case. Therefore, differences between the actual simulated values of C_L are expected. Note here also that the experimental

UNIVERSIDAD DE MÁLAGA

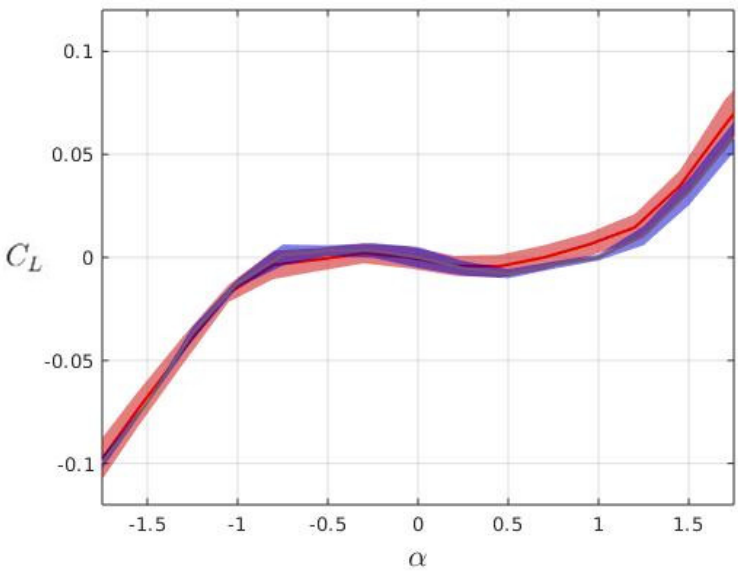

Fig. 4.5 Lift coefficient (C_L) for small angles of attack at $Re = 40 \times 10^3$ and semi-aspect ratio $sAR = 3$. Measures from $-1.75°$ to $1.75°$ in increments of $\Delta\alpha = 0.25$ going in the positive direction in red and going backwards in blue.

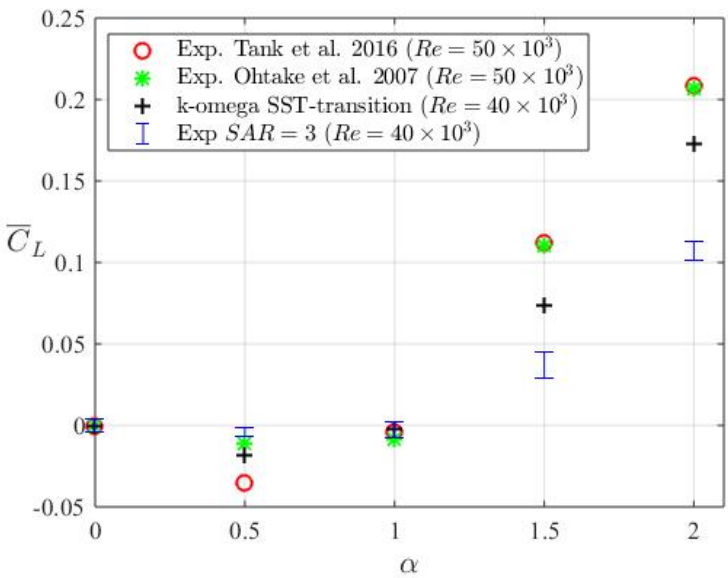

Fig. 4.6 Comparison of our averaged C_L obtained numerically and experimentally with the published results of Tank *et al.* [3] and Ohtake *et al.* [4].

UNIVERSIDAD DE MÁLAGA

results reported are not symmetrical with respect to the $y-axis$, whereas the numerical results are symmetrical. Therefore, an averaged value for the data reported in $-\alpha$ and α was used for comparison (changing the sign when it is necessary). Lastly, Fig. 4.6 also displays our experimental results obtained for $sAR = 3$, similar to $AR = 6.4$ used by Tank *et al.* [3]. Discrepancies between reported experimental values at α=1.5 or 2° are due to the differences in turbulence intensity and the rounded edge at the end of the wing model. As reported in Tank *et al.* [3], there are uncertainties in the experimental measurement while measuring the same NACA0012 aerodynamic profile. In addition, Laitone [76] and Kay *et al.* [77] predicted strong variations in the lift coefficient by applying changes in the turbulence intensity. However, our experimental results also follow the expected tendency for the C_L values having a smaller absolute value that the numerical results since they are computed in the two-dimensional limit.

4.6 Physical interpretation of the negative lift

To better understand the physical mechanism behind the non-linearity that produces negative lift coefficients, we analyzed the whole fluid field obtained numerically (not only the region near the trailing edge that was the focus of some of the previous explanations). To illustrate the physics behind it, we focus on two representative cases: $\alpha = 0.5°$, with negative C_L and $\alpha = 2°$, with positive C_L. Fig. 4.7 shows the streamlines in the zone near to the leading edge. Hereafter, the figures show dimensionless magnitudes. For the case of $\alpha = 0.5°$, Fig. 4.7(a) shows that the upstream streamlines are aligned with the chord direction, $\hat{i_1}$, and not with the horizontal direction of the absolute reference, $\hat{i}$, which is the direction of the free stream imposed as the inlet boundary condition. The first consequence of this upstream alignment of the flow is that the stagnation point (S) coincides with the leading edge (L). However, for the case of $\alpha = 2°$, Fig. 4.7(b), the flow has changed significantly. The streamlines are not aligned with the chord anymore. This deviation displaces the stagnation point (S) in the anti-clockwise direction ending in the bottom part of the NACA0012 profile, moving away from the leading edge.

Focusing on the dimensionless static pressure field near the stagnation point for a case with negative lift, Fig. 4.8(a), we observe the maximum pressure gradient ∇p_{max} pointing to the right in the chord direction. Hence, the application of this pressure gradient creates a very small negative net vertical force component in the global reference system. This force is responsible for the formation of a negative lift. However, for the case of $\alpha = 2°$, see 4.8(b), the local pressure gradient forms an angle of φ with the horizontal inducing a positive

UNIVERSIDAD DE MÁLAGA

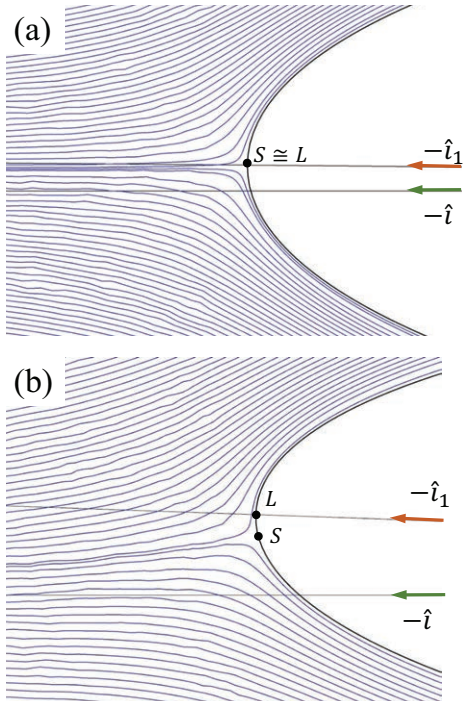

Fig. 4.7 Streamlines at $Re = 40 \times 10^3$ for $\alpha = 0.5°$ (a) and $\alpha = 2°$ (b).

vertical component producing the positive lift. Note that in both cases, with positive and negative lift, the local maximum pressure gradient is passing through the stagnation point.

To this point, we have investigated the phenomenon locally. However, a global analysis is needed to explain the mechanism that produces the flow behavior near the leading edge for both cases. The Kutta-Joukowski's theorem relates the negative lift on an airfoil with the induced circulation around it. Using the Stokes' theorem, the circulation, Γ, around the airfoil can be computed as a function of the vorticity, $\vec{\omega}$ as

$$\Gamma = \oint_L \vec{v} \cdot d\vec{l} = \int_S \vec{\omega} \cdot d\vec{s}, \tag{4.1}$$

where $\vec{\omega} = \nabla \times \vec{v}$. The closed line L enclosing the airfoil is followed in the positive (anti-clockwise) direction. That closed line can be any line far enough of the airfoil where exists potential flow field. In the case of a bidimensional velocity field, $\vec{v} = v_x\hat{\imath} + v_y\hat{\jmath}$, the vorticity has a unique component defined as,

$$\omega_z = \frac{\partial v_y}{\partial x} - \frac{\partial v_x}{\partial y}. \tag{4.2}$$

Fig. 4.9 shows contours of vorticity, ω_z, at an instant $t = 90$. The positive vorticity values (white color) correspond to local anti-clockwise rotation and the negative vorticity values

UNIVERSIDAD DE MÁLAGA

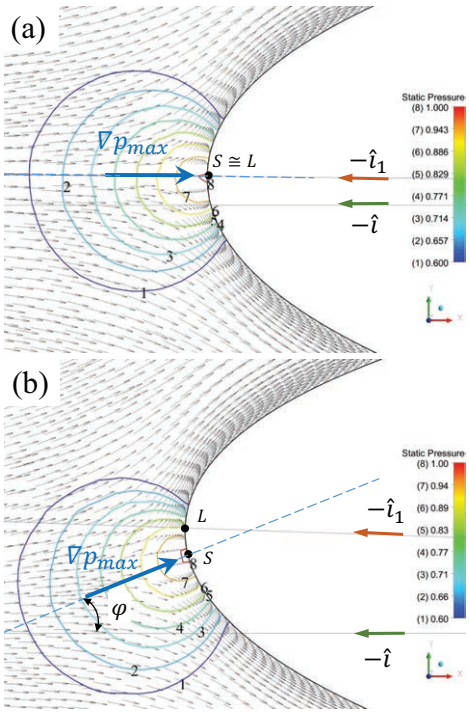

Fig. 4.8 Pressure field near the tip of the wing for a case of $Re = 40 \times 10^3$, $\alpha = 0.5°$ (a), $\alpha = 2°$ (b).

to local clockwise rotation. For the case of $\alpha = 0.5°$, Fig. 4.9(a), the wake is practically horizontal exhibiting a von Karman vortex street. However, for the case of $\alpha = 2°$, Fig. 4.9 (b), the wake has a slight deviation upwards. Note here that the non-dimensional vorticity contours were selected in both cases in the range of $-8 \leq \omega_z \leq 8$ to illustrate the wake. Conversely, the vorticity values in the zone near the leading edge of the airfoil are two orders of magnitude higher. Specifically, for the case of $\alpha = 0.5°$, $-1145 \leq \omega_z \leq 1099$ being almost symmetrical due to the pre-alignment. Whereas for the case of $\alpha = 2°$, the vorticity is more asymmetric and varies in the range of $-1317 \leq \omega_z \leq 956$.

To compute the circulation in both cases, the surface integral of the vorticity eq. 4.1 was solved using the whole domain as the integration surface S. Therefore, the line L corresponds to the exterior contour of the computation domain, where the vorticity has already decayed to zero (note that Fig. 4.9 is a zoomed version of the area around the airfoil and not the whole computational domain. The value of the circulation obtained for the case of $\alpha = 0.5°$ is $\Gamma = 0.0032$ indicating a net anti-clockwise circulation. An arrow was included in Fig. 4.9 to represent the circulation direction. This positive sign in the (small) circulation is the key point that causes the pre-alignment in the wing profile, as commented above. However, for the case of $\alpha = 2°$ the circulation is $\Gamma = -0.045$ corresponding to clockwise direction. It is important to remark that the circulation is an integral phenomenon closely related to the

UNIVERSIDAD DE MÁLAGA

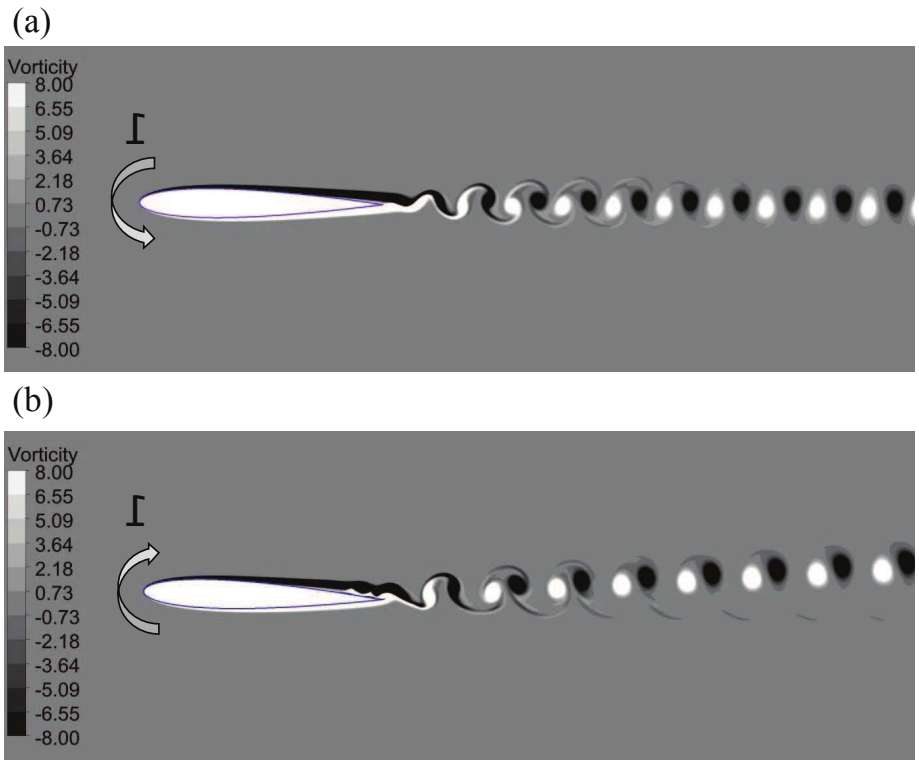

Fig. 4.9 Contours of ω_z at $t = 90$ for $Re = 40 \times 10^3$. $\alpha = 0.5°$ and $\Gamma = 0.0032$ (anti-clockwise, a); $\alpha = 2°$ and $\Gamma = -0.045$ (clockwise, b).

pre-alignment of the flow in the leading edge and the boundary layer separation in the trailing edge.

To analyze the influence of the circulation found in both cases, Fig. 4.10 represents velocity isocontours around the airfoil. In both cases, the maximum velocity is found very close to the top part of the wing (isoline-7). However, for $\alpha = 0.5°$, the isocontours of velocity in Fig. 4.10(a) show that the anti-clockwise circulation induces higher velocities in the bottom part of the profile. In other words and, broadly speaking, the flow moves faster in the bottom part of the wing. Whereas for $\alpha = 2°$, the velocity field displayed in Fig. 4.10(b) shows that the clockwise circulation induces to the flow to move faster in the top part of the profile. The effect on the field of static pressures is the opposite. Fig. 4.11 shows static pressure isocontours along the wing profile. For $\alpha = 0.5°$, the isobars move more downstream below the profile than above it (see isobar-8 as an example). Therefore, the static pressure over the top part of the profile is bigger than the static pressure in its bottom part, producing a negative net vertical force. Conversely, for $\alpha = 2°$, see Fig. 4.11(b), the resulting net vertical force is positive.

UNIVERSIDAD DE MÁLAGA

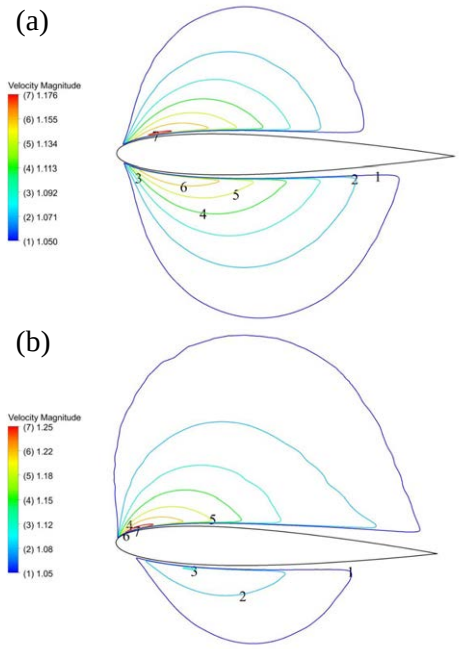

Fig. 4.10 Velocity contours for a case of $Re = 40 \times 10^3$, $\alpha = 0.5^\circ$ (a), $\alpha = 2^\circ$ (b).

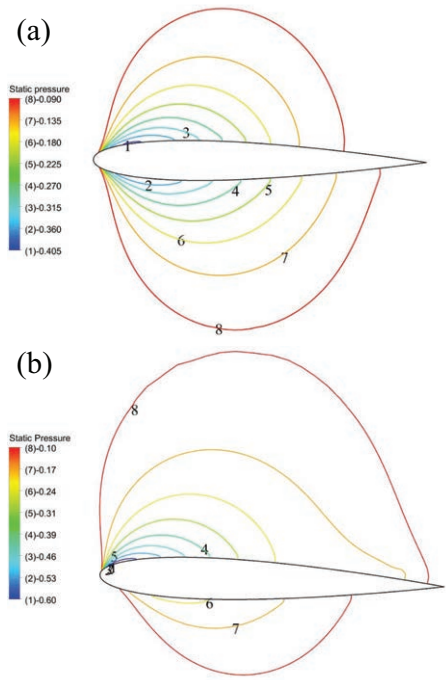

Fig. 4.11 Contours of static pressure for a case of $Re = 40 \times 10^3$, $\alpha = 0.5^\circ$ (a), $\alpha = 2^\circ$ (b).

UNIVERSIDAD DE MÁLAGA

As previously described, the flow has qualitatively some periodic spatial patterns that are not identical. To analyze the influence of the circulation on the temporal vortex emission, Fig. 4.12 represents the temporal evolution of the lift coefficient in both representative cases. The case of $\alpha = 0^\circ$ is also included in the figure as reference. For the case of $\alpha = 0^\circ$, C_L is oscillating around zero, see Fig. 4.12(a). However, the temporal evolution of the C_L is always negative for $\alpha = 0.5^\circ$and positive for $\alpha = 2^\circ$. We observed that the amplitude of the oscillations is equal for $\alpha = 0^\circ$ and $\alpha = 0.5^\circ$, but is an order of magnitude higher for $\alpha = 2^\circ$. Besides, the period for $\alpha = 0^\circ$ and $\alpha = 0.5^\circ$ is practically equal. This can be better understood in the normalized Power Spectral Density $P(St)/P_{max}$ presented in Fig. 4.12(b), where P_{max} is the maximum of the Power Spectral Density. The value of the Strouhal number (St=$f \cdot c/U$, f being the frequency of the periodic signal) is practically equal for $\alpha = 0^\circ$ and 0.5° ($St \approx 4.5$). However, it decreases to $St \approx 3.4$ for $\alpha = 2^\circ$ and displays a small harmonic of about 0.5% of the peak value at $St \approx 6.85$. Note that the vertical scale in Fig. 4.12(b) was amplified and has its maximum at 0.1, whereas the maximum value of the magnitude is 1.

(a)

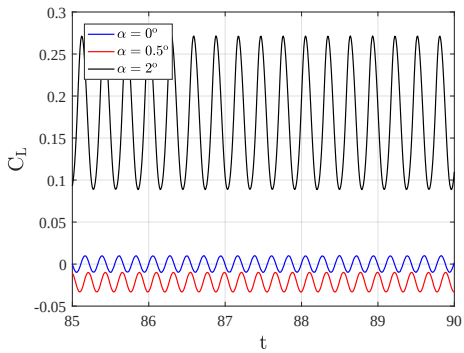

(b)

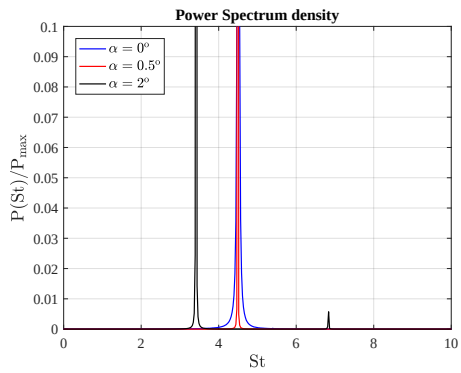

Fig. 4.12 Temporal evolution of C_L obtained at $t = 90$ for $Re = 40 \times 10^3$ and $\alpha = 0^\circ, 0.5^\circ$ and 2° (a), Power Spectral density for the same cases (b).

UNIVERSIDAD DE MÁLAGA

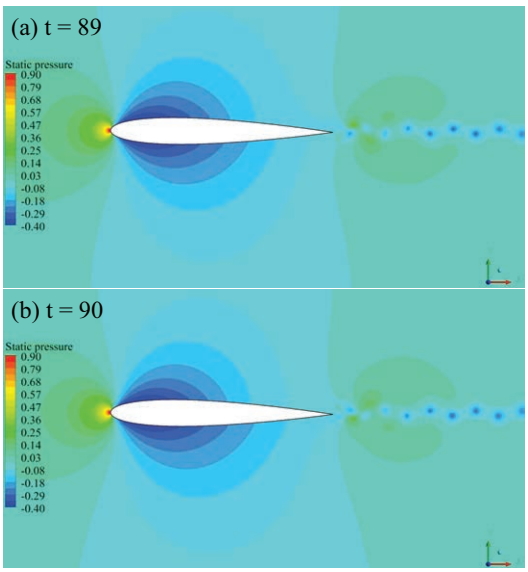

Fig. 4.13 Contours of static pressure for a case of $Re = 40 \times 10^3$, $\alpha = 0.5°$ $t = 89$ (a), $t = 90$ (b).

Last, Fig. 4.13 displays the static pressure at two different instants for the case of $Re = 40 \times 10^3$ and $\alpha = 0.5°$ to illustrate the general flow movement with negative lift. The pre-alignment upstream the leading edge is stationary, whereas the flow around the profile and near the trailing edge is not, producing the periodic behavior of the solution. Note that in both snapshots, the anti-clockwise circulation generates a faster net flow in the bottom part of the airfoil producing the negative lift.

4.7 Conclusions

We have analyzed the apparition of negative lift around a NACA 0012 profile for small angles of attack at Reynolds ($\mathscr{O}10^4$). Using a low turbulence wind tunnel, we observe that the non-linearity around the zero angle of attack occurs only for big enough aspect ratio. Specifically, for $sAR = 1$, the flow is full three-dimensional, and C_L is linear, for $sAR = 2$ we capture a low non-linearity and for $sAR = 3$ we were able to capture clearly the negative lift. To understand the origin of this phenomenon, we have performed two-dimensional numerical simulations using a SST transition model implemented in Ansys®-Fluent v19.1. We have validated our results with the previous research studies that were able to reproduce the negative lift obtaining a good agreement. In all of them, the negative lift occurs for angles of attack approximately lower than 1°, reaching its minimum ($C_L = -0.025$ in our simulations) at 0.5° approximately. Since the negative lift appears experimentally for an

UNIVERSIDAD DE MÁLAGA

aspect ratio relatively big, and the two-dimensional simulations (equivalent to infinite aspect ratio) are able to reproduce negative lift too, the onset of negative lift seems to be related mainly by both temporal and spatial two-dimensional periodic patterns.

The numerical simulations have also revealed that the existence of the negative lift for the case of $\alpha < 1^\circ$ at $Re = 40 \times 10^3$, is directly connected with the net anti-clockwise circulation around the airfoil. This circulation produces a faster velocity field in the bottom part of the airfoil, decreasing its static pressure in that region, generating a negative lift force. Another characteristic feature of the cases with negative lift force is a pre-alignment of the flow upstream the airfoil resulting in a maximum gradient of pressures with a negative vertical component near the leading edge, promoting the negative lift. For cases with positive lift, the computed net circulation around the airfoil is clockwise, producing a positive lift as predicted by the Kutta-Joukowski's theorem.

UNIVERSIDAD DE MÁLAGA

UNIVERSIDAD
DE MÁLAGA

Chapter 5

GPU computed PIV

5.1 Background

In chapter 2 concerning the two large experimental facilities used in this thesis, the details related to the use of the two-dimensional particle image velocimetry (PIV) technique have not been referred. Only the use of the software DPIVSoft developed at the Institut de Recherche sur les Phénomènes Hors Equilibre in Marseille (France) was mentioned [34]. We describe in this chapter a graphic processing unit (GPU)-accelerated PIV algorithm using DPIVSoft as the basis for this development. We rigorously validate the algorithm using synthetically generated images and experimental data. Our final goal is to ensure that the software is freely distributed and easy to use. Thus, this combination of DPIVSoft and GPUs has been the basis for the analysis of the synthetic images in chapter 6, and for non-stationary aerodynamics experiments that will be presented in chapter 7.

As mentioned, it has been considered appropriate to develop in this chapter and the following one a fundamental tool in this thesis. The implementation of the software DPIVSoft on GPUs to accelerate the obtaining of results. This aspect will be dealt with in this chapter while the knowledge of the results according to the typical parameters of the PIV will be dealt with in the following two chapters. The reader should note that all this set of tools has the purpose of one of the contributions of this thesis: the development of indirect force measurements by means of the velocity field in a (bounded) window of images with tracer particles.

The software DPIVSoft performs a two-pass algorithm with window deformation and sub-pixel accuracy that has proven to faithfully reproduce a wide variety of vortex flows with high velocity gradients [34]. Even though this program worked very well in rotating flows [35–37], we found two drawbacks that could be improved. On one hand, it is written in Matlab, which is a proprietary software with a high price per license. Therefore, although

UNIVERSIDAD DE MÁLAGA

the software is open source, the proprietary platform required for its use may prevent many researchers from using it. On the other hand, despite the high calculation speed provided by this software, it is not optimized for parallelism and use on GPUs, but given the nature of PIV algorithms and GPUs accessible today, the performance increase can be overwhelming, so it seemed to make sense to develop a new PIV software based on the software DPIVSoft (which have given us great results), but written in open languages (Python & OpenCl) and capable of using all the power of the GPU.

Nowadays, it is clear that with the advance of parallel computing on GPUs, the accuracy of obtaining a velocity field using PIV does not have to be sacrificed for the speed of computing. Historically, one of the first research projects to use GPUs for PIV was in 2004 [104]. In this work, an efficient FFT algorithm was used to accelerate a basic PIV algorithm based on a single pass of interrogation windows and cross-correlation. It is evident that in 2004, the development of GPUs was not so incipient since user-developed programs were not yet being built. Parallel computing was also on the rise and what was later called general purpose computing on GPUs (GPGPU) emerged. It was 6 years later when Tarashima and its collaborators [105] executed multiple GPUs to accelerate image processing with up to 256 x 256 pixels^2 on the order of 120 times, reaching 30 PIV processing in a second in some image sizes. Later, Champagnat and his collaborators [106] took a different approach by using a gradient-based cross-correlation algorithm so-called FOLKI (French acronym for Iterative Lucas-Kanade Optical Flow, [107]) and achieved a 50-fold acceleration using higher spatial resolution images. This software is similar to the one developed by Meunier [34], but as indicated DPIVSoft is more suitable for flows with high rotation such as the ones studied in chapters 6 and 7.

In relation to existing free software, the OpenPIV source code, also written in Python [108], has pioneered the use of GPUs in its algorithm and is actively developing it over the last few years. OpenPIV allows pre-processing, speed calculations and post-processing of PIV data. This software architecture is based both on the rapid development of Python itself, and on fast and efficient execution. The GPU-accelerated PIV algorithm has been added as a module for OpenPIV, and can be used with any NVIDIA GPU system. One can use the PyCUDA API to interface the OpenPIV Python source code with a GPU [109]. Finally, it is worth mentioning that Lavision also includes from 2015 a PIV uncertainty calculation accelerated on GPU with the software DaVis 8.2.3 version.

UNIVERSIDAD DE MÁLAGA

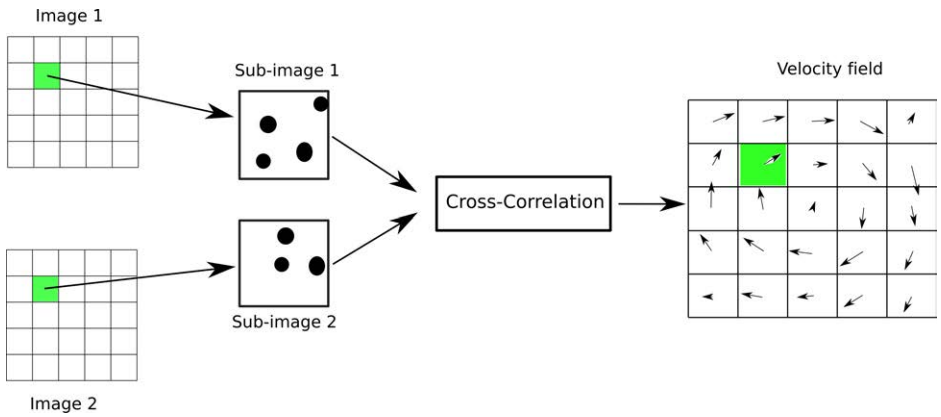

Fig. 5.1 Outline of the basic functioning of PIV.

5.2 Particle Image Velocimetry with windows deformation

The PIV technique consists of a laser sheet in the plane of interest that is recorded with a camera. The flow must have tracer particles that follow the movement of the fluid and are illuminated by the laser. The images are processed by pairs to determine the displacement of the particles and, in combination with the known time between images, to obtain the velocity field.

The images are divided into smaller interrogation windows, in each window is performed the cross-correlation with is homologous in the next image, the peak of the cross-correlation gives the average velocity of the particles within that window as outlined in Fig. 5.1.

There exist many limitations in this process [5]. In the first place, an optimum number of particles (between 8 and 20) in each window is required to obtain good results from the cross-correlation. The displacement of the particles needs to be less than 2/3 of the size of the windows to be able to find the peak, so it's needed to play with both, size of the windows and time between frames. The final problem is that the velocity obtained is the linear average of the windows, the relative movements inside the windows are discarded so the resolution achieved is critical to describe the flow.

Being I and I' the intensity of light in the first and second image, direct cross-correlation is given by equation (5.1), which essentially consist of a linear shift of the I template around the I' template without extending over edges of I' (must be notice that I needs to be smaller than I'). The maximum position of this operation will give the average displacement of the tracers in that interrogation window between two frames.

$$R_{II'}(x,y) = \sum_{i=-K}^{K} \sum_{j=-L}^{L} I(i,j) I'(i+x, j+y). \tag{5.1}$$

UNIVERSIDAD DE MÁLAGA

This operation can be performed much faster using the correlation theorem that allows calculating the cross-correlation as the complex conjugate multiplication of its Fourier transforms, as schematized in Fig. 5.2. This approach changes the complexity of the problem from $O\left(N^4\right)$ to $O\left(N^2 \log_2 N\right)$, with a corresponding increase in performance.

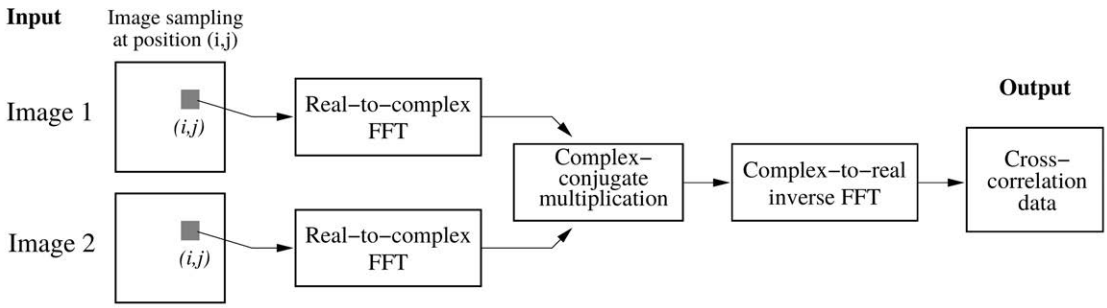

Fig. 5.2 Cross-Correlation process using the correlation theorem [5].

.

The common values for the sizes of the interrogation windows are typically 16x16, 32x32, and 64x64, and they can overlap by 50%. It is not unusual to find 1, 2 or 4 Mpx cameras, so the number of interrogation windows computed for each pair of images can range from 4024 to 254016 or even more. Each interrogation window is independent of the other ones, so all operations can be performed in parallel (and can be further parallelized within each window). All this justify the need to use GPUs in this type of processing.

The specific algorithm used in DPIVSoft is as follows. In the first step, the pair of images are divided into large interrogation windows, and a cross-correlation is performed on each window to obtain the average displacement. Sub-pixel precision is achieved by a three-points Gaussian fit estimator ([110]). The resulting velocity field is filtered to remove outliers and interpolated into a new, finer mesh with smaller interrogation windows. Next, each interrogation window is deformed according to the previously calculated velocity field, so that the new cross-correlation will be centered more or less in the middle point, preventing that the 2/3 of the window limit is exceeded in the second iteration with smaller windows. The process of deforming the image and performing a new cross-correlation can be used several times to improve accuracy, even without changing the size of the cross-correlation windows. The full algorithm is schematized in Fig. 5.3.

5.3 GPU acceleration

Once the algorithm of the software DPIVSoft is clear, we will explain the implementation on the GPU. This implementation have been written using OpenCL, which is an open language

UNIVERSIDAD DE MÁLAGA

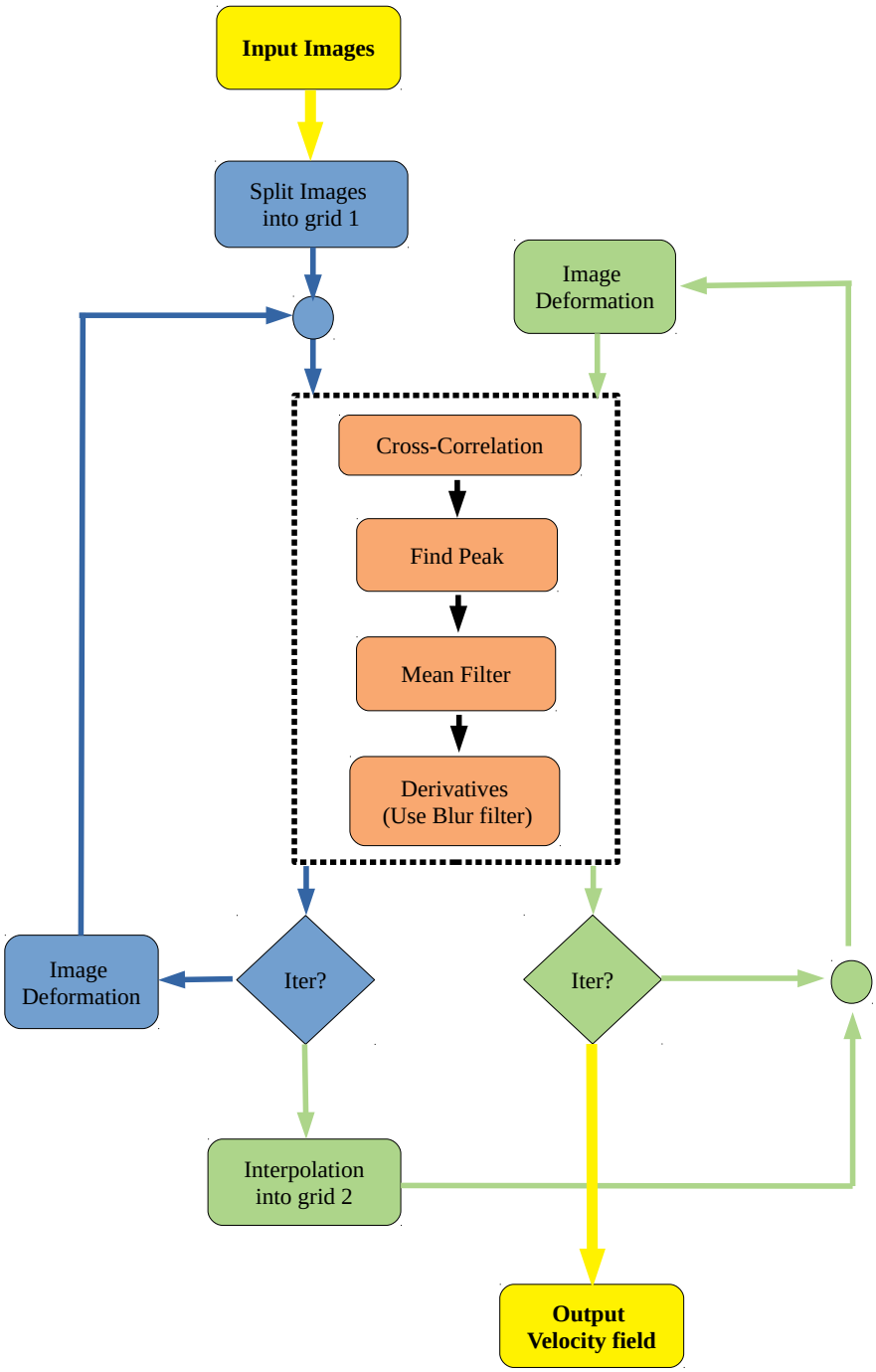

Fig. 5.3 DPIVSoft algorithm scheme.

UNIVERSIDAD DE MÁLAGA

and allows parallelization on AMD and Nvidia GPUs [111], but the same code can even be run in parallel on CPUs without changing the code. The hosting platform used in the CPU is Python, which is an increasingly popular language with wide library support and, unlike its competitor Matlab, is open-source. Besides, to perform the necessary FFTs transformations in the GPU, the not so used library Reikna has been chosen. This library have the advantage that it can be used not only with OpenCL but also with CUDA, so it will give even more possibilities to change the code in the future.

Every calculation is made with simple precision to not compromise performance. The two pairs of images are sent to the global memory of the GPU. No further communication with the CPU is needed until the algorithm is finished, so all calculations are performed on the GPU for maximum reduction of communication time between the host and the device. Sub-images are stored in NxNxK arrays, which represent k sub-images of NxN pixels with the value being the intensity of the light on the greyscale. Four arrays are required, two for the first step and two for the second. Each pixel of the sub image is overwritten on the parallel matrix using the GPU.

As soon the matrices are filled into memory, the cross-correlation is performed. The peak is found, and the velocity field is filtered using a mean filter. After that, the velocity derivatives are calculated and interpolated into the finest mesh, to perform the image deformation and repeat the process. OpenCL allows asynchronous communication, that is, if no communication is needed, the CPU can be doing operations while the GPU is running. We take advantage of this capacity to save the results without increasing the calculation time. When several fields have to be processed, and once a pair of images are loaded in the GPU, the CPU starts writing the results of the previous pair while the GPU is running. This is how the time needed to write to the hard disk is concealed in the real processing time.

5.4 Results and performance

The GPU used for the test is an AMD Radeon RX 580 Series with a POLARIS10 chip. The most relevant characteristics are 8GB of GDDR5 RAM and 2034 stream processors divided in 36 calculation units. The computations have been executed in OpenCL 1.2 which is the most modern version that supports this GPU.

The code has been tested using synthetic images of 1024x1024 pixels. The tracers are placed randomly along the image with a density of 0.03 particles/pixel. The particles are described by a Gaussian intensity profile as follows

UNIVERSIDAD DE MÁLAGA

$$I(x,y) = I_o \exp\left[-\frac{(x-x_o)^2+(y-y_o)^2}{d_\tau^2/8}\right] , \tag{5.2}$$

where d_τ is the diameter of the particle located at (x_o, y_o) with a peak intensity of I_o.

Two canonical problems have been selected to test the algorithm. The first one is the 2D (laminar) Hagen-Poiseuille flow between two parallel flat plates. We consider that the maximum axial velocity U_{max} in the center of these two parallel flat plates is related to the axial velocity distribution $u(y)$ using the analytical solution in a Cartesian frame

$$u = U_{max} y (h-y) , \tag{5.3}$$

where h is the total height of the image.

The second flow used for this test is a two-dimensional vortex given by the following expression Scully [112]

$$u_{theta} = \frac{\Gamma}{2\pi}\frac{r}{R^2+r^2} , \tag{5.4}$$

being u_θ the azimuthal component of velocity, and r the radial position. The parameters introduced to generate the desired vortex are the position of maximum tangential velocity R and the circulation Γ.

To compare the basic function of the algorithm, the above two velocity fields have been obtained using the same settings for the CPU and GPU versions of the PIV with a single iteration in the first and second grid. All parameters are shown in Table 5.1.

Parameters	1° sweep	2° sweep
Correlation box size in x	64	32
Correlation box size in y	64	32
Nº of boxes in x	30	60
Nº of boxes in y	30	60

Table 5.1 PIV parameters

Before moving on to the results and performance, there are two limitations on the current state of the algorithm version on the GPU, in comparison with the Matlab version of the DPIV Soft [34], which should be noted. The first point is that filtering between steps is not done at the edges of the PIV field. A satisfactory solution for making this exception in parallel without compromising GPU performance has not been implemented yet. The second point is that no weighting method has been developed for the GPU either.

In Fig. 5.4, we compare the resulting flow velocity fields obtained by each algorithm with those provided by the exact solution that have been used to generate the synthetic images. We

UNIVERSIDAD DE MÁLAGA

observe very subtle differences in these vector representations, which will then be quantified by calculating the normalized error with respect to the analytical solution.

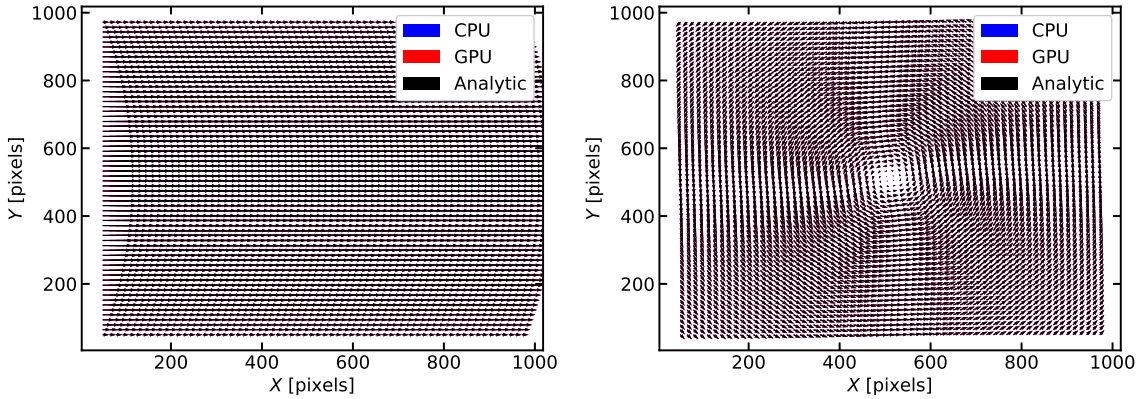

(a) (b)

Fig. 5.4 Velocity fields obtained with the new implementation of PIV for two different synthetic flows: the 2D (laminar) Hagen-Poiseuille flow (a) and 2D vortex (b).

Regaining to the vortex case, it is more interesting to compare the accuracy of the algorithm using some standard characterization of the vortex in polar. In this case, we compare the azimuthal velocity along the radius of the vortex impose with the one obtained using each PIV algorithm in Fig. 5.5.

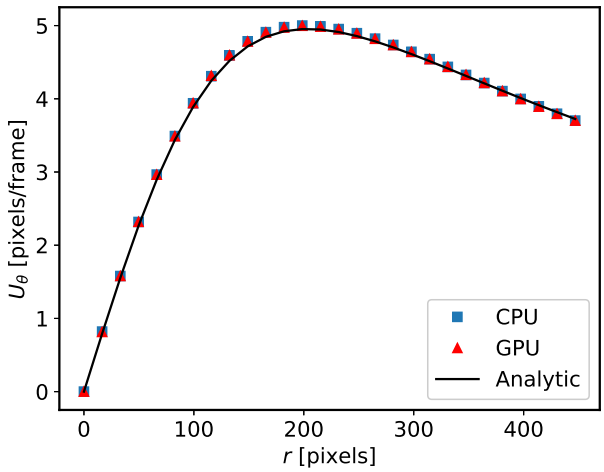

Fig. 5.5 Azimuthal velocity of vortex as function of radius.

The error ε given in % at each point in the mesh committed by each method (CPU versus GPU) has been calculated and normalized to the magnitude of the average speed using the equation (5.5). The value of the error is represented in Fig. 5.6 for both flows using the CPU

UNIVERSIDAD DE MÁLAGA

(a, b) and the GPU (c, d). The mean and maximum errors are summarized in Table 5.2. One can observe that the differences in accuracy are very small and can be assumed taking into account the enormous increase in computation time that will be analyzed below.

$$\varepsilon = \frac{\sqrt{(u_u_{real})^2 + (v - v_{real})^2}}{mean\left(\sqrt{u_{real}^2 + v_{real}^2}\right)} \times 100 \,, \tag{5.5}$$

Table 5.2 PIV error in %

PIV error	Poiseuille		Scully	
	max	mean	max	mean
CPU	1.19	0.44	5.06	1.62
GPU	1.12	0.44	5.27	1.63

To finish this chapter, we check the performance increase that is achieved with this GPU acceleration. Fig. 5.7 (a) shows in logarithmic scale the computation time of each image pair for different total number of correlation boxes in the second sweep using the CPU or the GPU. In all cases, the sizes of the correlation boxes are 64x64 and 32x32 for the first and second sweeps, respectively. In general, the number of correlation boxes in the first sweep is the square of the root of the total boxes in the second sweep for the GPU implementation. Furthermore, Fig. 5.7 (b) shows how the GPU dramatically increases the PIV processing speed by a factor between 90 and 320 times the CPU performance depending on the size of the data. This means that even for very large images, we are able to obtain a few fps, which opens the possibility of real-time processing while performing the experiments.

To summarize the achievements of this chapter, we have translate an already widely used PIV algorithm (DPIVSoft) into Python, which has the advantage of being an open platform. After that, the code has been prepared to GPU acceleration capabilities on OpenCL to can be used with GPU of different manufacturers. We test the algorithm using synthetic images in two canonical flows, a Poisson flow and a Scully vortex. Our GPU implementation demonstrates the same accuracy than the original source. On the other hand, a huge increase in performance is achieved, which increases with the number of interrogation windows of the PIV. The drawback of this implementation is the big amount of VRAM needed to run all calculations on GPU without communication with the host, this makes that on the GPU tested with 8GB of VRAM. Using 64x64 and 32x32 pixel interrogation window for first and second sweep, we observe a drop in the speed up for 2^{15} interrogation windows boxes on the second sweep, which is related to the lack of memory, so the calculations need to be split

UNIVERSIDAD DE MÁLAGA

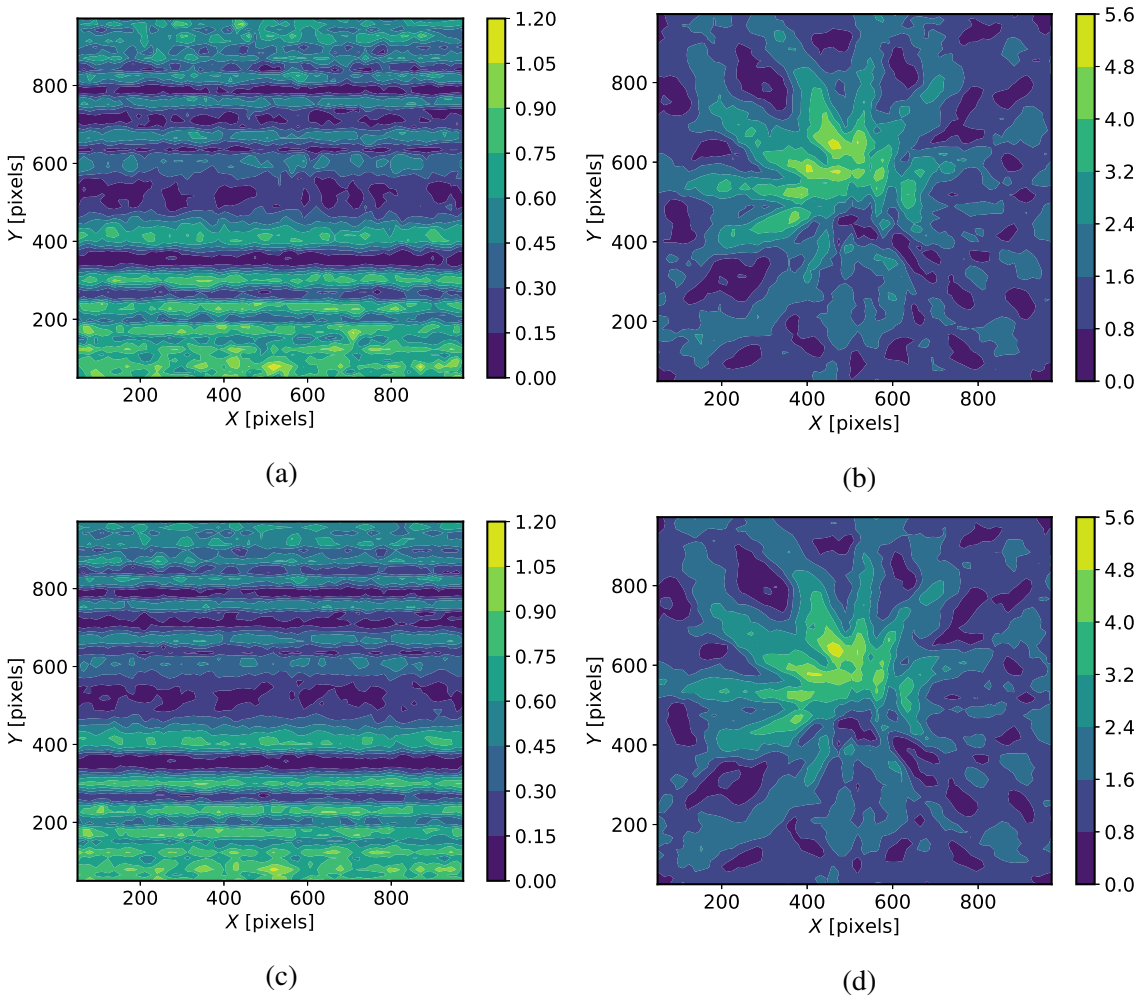

Fig. 5.6 On the left and right columns the 2D Hagen-Poiseuille flow and the Scully vortex, respectively, with the contours of the normalized error on the CPU (a, b) and the GPU (c, d).

UNIVERSIDAD DE MÁLAGA

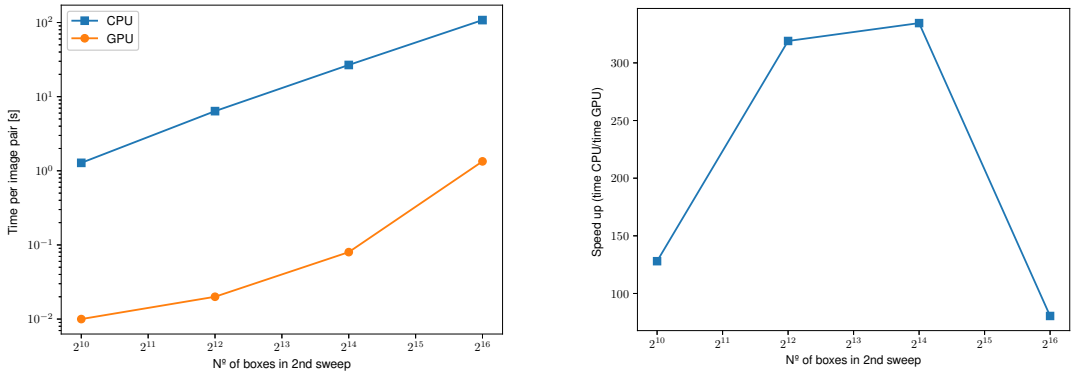

(a) (b)

Fig. 5.7 Comparison on performance of the GPU implementation compared with CPU. (a) Computational time per image pair, (b) CPU computational time divided by GPU one.

and some communication with CPU occurs. Anyways, even in this situation, the speedup of GPU implementation is substantial.

UNIVERSIDAD DE MÁLAGA

UNIVERSIDAD
DE MÁLAGA

Chapter 6

PIV Forces

6.1 Background

Obtaining forces from indirect measurements on a submersed body is one of the most potentially useful applications of PIV for Aerodynamics research. The idea is clear, if we have the velocity field around the body which is interesting by itself, we could obtain the forces that act on this body using only this information, without the need to include additional expensive and difficult to use instrumentation, such as force or pressure sensors as they will add complexity and limitations to the design of the experiment.

The experimental velocity fields can be obtained from the PIV measurements introduced in the Chapter 2, but obtaining the forces from it can be more intricate because the error sensitivity of differential and integral quantities needed to calculate the forces. There are several works related to PIV-2D estimation of aerodynamic forces, see details in Lin and Rockwell [113], Noca et al. [114], Unal et al. [115], Noca et al. [116], van Oudheusden et al. [117, 118], Spedding and Hedenström [28], Jardin et al. [119], van Oudheusden [120], Gharali and Jonhson [121], Siala and Liburdy [122], among others. From the data obtained in these works, the following aspects related to the numerous disadvantages linked to the indirect calculation should be highlighted. Either large dimensions are required around aerodynamic profiles to accurately calculate the forces or details of the velocity field are needed very close to their surfaces, which is a very complicated task to achieve for PIV measurements. Besides, it is necessary to derive the pressure from the velocity field by directly applying the Navier-Stokes equations (DeVoria et al. [123]), although Noca et al. [116] developed a formulation that avoided this calculation. However, Noca's momentum equation gives good results for the lift, but not for the drag coefficients (Albrecht et al. [124]). In this research work, we show two other PIV-2D-based formulations that do not require

UNIVERSIDAD DE MÁLAGA

pressure calculation, and we also provide reasonably good results using a spatially delimited domain where 2D-PIV measurements are performed.

It is well known that the noise introduced into the equations due to the PIV measurements is an essential source of error in the indirect estimation of the forces (see in detail Rival et al. [125]). Besides, the problem of instantaneous forces calculation could be very complicated, depending on the unsteady flow analyzed. Specifically, Guissart et al. [126] performed non-stationary load measurements on a flat plate with high angles of attack using the approximation of the moment equation. This indirect calculation proves to be reasonably accurate. However, there are difficulties associated with (i) the dark areas of the PIV-2D that are avoided by imposing symmetry on the problem, and (ii) the lack of pressure related data provided by the calculation using the Poisson's equation [127, 124]. This last limitation is especially critical in the wake of the body, where there must be an iterative process to correct the errors. In our case, we will use the correction in the wake proposed by Martín-Alcántara and Fernandez-Feria [128] to match the terms on the output surface of the control volume.

The impulse formulation can be applied to 2D-PIV measurements, and it has the advantage of not calculating the pressure. Graham et al. [129] used the 2D-PIV method to determine the forces based on the impulse formulation on a moving flat plate with a constant angle of attack. They presented a novel technique in which the incomplete experimental vorticity field was coupled to a theoretically calculated vortex-sheet in the body. Thus, the force was computed as the sum of the vortex-sheet and the experimental contributions. The experimental procedure developed in this work may be applied to any configuration of flapping flat plate to estimate the forces exerted on its surface. However, the spatio-temporal resolution of the 2D-PIV must be accurate near the boundary layer. Besides, McClure and Yarusevych [130] reported the common problems responsible for the inconsistent estimates of the instantaneous and mean sectional loads of the three-dimensional flows using control volume methods. Limacher et al. [131] compared the decomposition of fluid-dynamic forces into Generalized Added Mass and Circulatory (GAMC) with those obtained from the standard impulse formulation (SIF). They found that the measured and filtered drag force was greater than the calculated forces, but the trends were largely the same. Also, the forces calculated by the GAMC formulation were less sensitive to random error in velocity than the SIF and lastly, the GAMC was much more tolerant of the omission of near-body vorticity data. Recently, Siala and Liburdy [122] found that LEV achieved optimal formation in the lift force generated by a sinusoidally heaving and pitching airfoil during dynamic stall using SIF. They reported that SIF could be simplified in two terms: (i) the rate of temporal change of vortical structures within the control volume, and (ii) the contribution of vortical structures outside the control volume. Finally, they pointed out that the error was amplified at the lower limit

UNIVERSIDAD DE MÁLAGA

of the control volume and that the proposal of Kang et al. [132] to use a minimum-domain impulse formulation was very limited by the field of view provided by the PIV imaging system.

In this chapter, we present the indirect calculation of the dimensional force using the numerical or experimental velocity fields in a limited domain. The formulations we will use will be the force balance equation and the impulse formulation. These two approaches will be presented for an inertial and non-inertial reference system. We will see the numerical example of a square-shaped object with an incident flow (inertial system) in this chapter, while in the following one we will consider the examples of a non-inertial system (moving flat plate) in the forward flight and hovering configurations.

6.2 Force formulations

6.2.1 Momentum balance

The first intuitive idea to calculate the forces acting on a body from the velocity field, is to use the (dimensional) integral form of the conservation of momentum as follows

$$\frac{d}{dt}\int_V \rho\vec{v}dV + \int_S \rho\vec{v}\vec{v}\vec{n}dS = -\int_S p\vec{n}dS + \int_S \bar{\bar{\tau}}'\vec{n}dS + \int_V \vec{f}_m dV\,, \tag{6.1}$$

where on the left side of the equation, all integrals can be computed directly from the velocity field. The forces acting on the body are pressure and viscosity evaluated on the body surface S_b. So substituting it and taking into account that velocity on the body is null due to the non-slip condition, one can obtain the total force in the following manner

$$\vec{F} = -\frac{d}{dt}\int_V \rho\vec{v}dV - \int_{S_o} \rho\vec{v}\vec{v}\vec{n}dS - \int_{S_o} p\vec{n}dS + \int_{S_o} \bar{\bar{\tau}}'\vec{n}dS + \int_V \vec{f}_{mass}dV\,, \tag{6.2}$$

where S_o are the four surfaces within the control volume (S_o=S_1+S_2+S_3+S_4 depicted in Fig. 6.1), in other words, the surfaces corresponding to the boundaries (excluding the body surface S_b shown in grey in Fig. 6.1). For a two dimensional and incompressible flow, the viscosity tensor $\bar{\bar{\tau}}'$ is given by

$$\bar{\bar{\tau}}' = \mu\left(\nabla\vec{v} + \nabla\vec{v}^T\right) = \mu\begin{pmatrix} 2\frac{\partial u}{\partial x} & \frac{\partial u}{\partial y}\frac{\partial v}{\partial x} \\ \frac{\partial u}{\partial y}\frac{\partial v}{\partial x} & 2\frac{\partial v}{\partial y} \end{pmatrix}, \tag{6.3}$$

The mass forces $\vec{f}_{mass}$ are relative to the system reference frame, and are given by

UNIVERSIDAD DE MÁLAGA

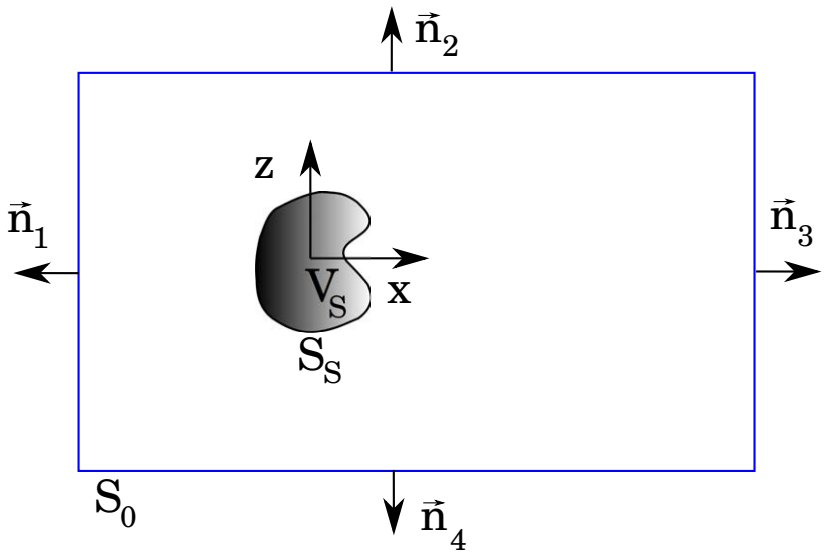

Fig. 6.1 Scheme of the body and surfaces of the control volume.

$$\vec{f}_{mass} = -\vec{a}_o - \frac{d\vec{\Omega}}{dt} \wedge \vec{x} - \vec{\Omega} \wedge \left(\vec{\Omega} \wedge \vec{x}\right) - 2\vec{\Omega} \wedge \vec{v}, \tag{6.4}$$

being $\vec{a}_0$ and $\vec{\Omega}$ the linear acceleration and angular velocity of the reference frame. Of course, this last term will only be non-zero for a non-inertial frame of reference. Therefore, from a velocity field of the PIV measurements, the only term to be calculated indirectly is the surface pressure at the domain boundaries. This can be done using the differential form of the Navier-Stokes equation:

$$\nabla p = -\rho \frac{\partial \vec{v}}{\partial t} - \nabla \cdot (\rho \vec{v}\vec{v}) + \mu \nabla^2 \vec{v} + \rho \vec{f}_m. \tag{6.5}$$

A common method to compute this equation is to perform the divergence operator on both sides, which will give us a laplacian equation for pressure:

$$\nabla^2 p = \rho \left[\left(\frac{\partial u}{\partial x}\right)^2 + 2\frac{\partial v}{\partial x}\frac{\partial u}{\partial y} + \left(\frac{\partial v}{\partial y}\right)^2 \right]. \tag{6.6}$$

Both approaches (6.5)-(6.7) introduce big errors into the solutions, but we will try to reduce them as much as possible. In a first stage, to obtain the pressure it is necessary to implement an integration scheme, which will be very sensitive to errors. Another problem comes from the fact that it is not so easy to integrate the pressure around a body, as long as the values of the mesh positions for the body do not interfere with the solution and do not step forward to generalize for any object shape within an equi-spaced standard PIV mesh. In our case we will generate an unstructured mesh by surrounding the body using *Gmsh*. We

UNIVERSIDAD DE MÁLAGA

will interpolate the velocity field into that mesh to integrate the laplacian pressure (6.7) using the finite difference scheme with Neumann and Dirichlet boundary conditions for the body surface and the domain boundaries, respectively. The pressure field will be interpolated back into the PIV mesh to perform the closed-surface integral of the pressure using (6.2).

Finally, and for the sake of simplicity in interpreting the results, we will name the force obtained by the balance equation (6.2) as $\vec{F}_m$ (subscript m referring to the momentum balance equation), so that this equation can be rewritten as the sum of the different integral terms as follows:

$$\vec{F}_m = \vec{F}_{mV} + \vec{F}_{mSo} + \vec{F}_{mp} + \vec{F}_{m\mu} + \vec{F}_{mmass}\,, \tag{6.7}$$

and the lift and drag coefficients (C_{Lm} and C_{Dm}) are given by:

$$C_{Dm} = \frac{F_{mx}}{\frac{1}{2}\rho U_\infty^2} = \frac{F_{mVx} + F_{mSox} + F_{mpx} + F_{m\mu x} F_{mmassx}}{\frac{1}{2}\rho U_\infty^2} =$$

$$C_{DmV} + C_{DmSo} + C_{Dmp} + C_{Dm\mu} + C_{Dmmass}\,, \tag{6.8}$$

$$C_{Lm} = \frac{F_{mz}}{\frac{1}{2}\rho U_\infty^2} = \frac{F_{mVx} + F_{mSox} + F_{mpx} + F_{m\mu z} + F_{mmassz}}{\frac{1}{2}\rho U_\infty^2} =$$

$$C_{LmV} + C_{LmSo} + C_{Lmp} + C_{Lm\mu} + C_{Lmmass}\,. \tag{6.9}$$

6.2.2 Impulse Formulation

Another option to obtain the force contributions is to use the impulse formulation (IF) developed by Wu et al. [133, 134, 135]. This theory is well known for decomposing the force into circulatory and non-circulatory contributions, together with the linear dependence of vorticity. There are two main limitations to force measurements using this method, (i) the finite control volume, and (ii) the velocity measurements near the boundary layer at both the leading and trailing edges. To solve the first problem, we use the formulation proposed in Martín-Alcántara and Fernandez-Feria [128], where the contribution of vortices leaving the domain is corrected by adding a new term $\vec{F}_{io}$. For a control volume that is non-inertial and bounded, it can be expressed as follows in a dimensional form (subscript i referring to impulse formulation):

$$\vec{F}_i = \vec{F}_{iv} + \vec{F}_{iI} + \vec{F}_{io} + \vec{F}_{iRe} + \vec{F}_{iV}\,, \tag{6.10}$$

where:

UNIVERSIDAD DE MÁLAGA

$$\vec{F}_{iv} = -\rho \int_{V_c} \mathscr{L} dV \,, \tag{6.11}$$

$$\vec{F}_{iI} = -\rho \int_{V_c} \vec{x} \wedge \frac{\partial \vec{\omega}}{\partial t} dV \,, \tag{6.12}$$

$$\vec{F}_{io} = -\rho \int_{S_o} \vec{x} \wedge (\vec{n} \wedge \mathscr{L}) \, dS \,, \tag{6.13}$$

$$\vec{F}_{iRe} = \mu \int_{S_o} [\vec{\omega} \wedge \vec{n} - \vec{x} \wedge (\vec{n} \wedge \bigtriangledown \wedge \vec{\omega})] \, dS \,, \tag{6.14}$$

$$\vec{F}_{iV} = \rho \frac{d}{dt} \int_{V_s} \vec{V} dV \,, \tag{6.15}$$

and V=V_c+V_s, and V_s is the solid volume (grey in Fig. 6.1), S_o are the four surfaces within the control volume (S_o=S_1+S_2+S_3+S_4), and $\mathscr{L}$ is the Lamb's vector ($\mathscr{L} = \vec{\omega} \wedge \vec{v}$ scaled with $\hat{U}^{*2}/\hat{c}$, where U^* is the dimensional velocity). Developing each term in the surfaces limiting the volume control depicted in Fig. 6.1, we obtain the contribution to lift and drag coefficients as the contributions in the x and z coordinates, respectively:

$$F_{ivx} = \rho \int_{V_c} \omega v_z \vec{e}_x dV \,, \tag{6.16}$$

$$F_{iIx} = -\rho \int_{V_c} \frac{\partial \vec{\omega}}{\partial t} z \vec{e}_x dV \,, \tag{6.17}$$

$$\begin{aligned} F_{iox} = \rho \int_{S_1} v_x \omega z \vec{e}_x dz - \rho \int_{S_2} v_z \omega z \vec{e}_x dx \\ - \rho \int_{S_3} v_x \omega z \vec{e}_x dz + \rho \int_{S_4} v_z \omega z \vec{e}_x dx \,, \end{aligned} \tag{6.18}$$

$$\begin{aligned} F_{iRex} = -\mu \int_{S_1} z \frac{\partial \omega}{\partial x} \vec{e}_x dz - \mu \int_{S_2} \left(\omega - z \frac{\partial \omega}{\partial z} \right) \vec{e}_x dx \\ + \mu \int_{S_3} z \frac{\partial \omega}{\partial x} \vec{e}_x dz + \mu \int_{S_4} \left(\omega - z \frac{\partial \omega}{\partial z} \right) \vec{e}_x dx \,, \end{aligned} \tag{6.19}$$

$$F_{iVx} = \rho V_s \frac{d^2 h_x}{dt^2} \vec{e}_x \,, \tag{6.20}$$

$$F_{ivz} = -\rho \int_{V_c} \omega v_x \vec{e}_z dV \,, \tag{6.21}$$

UNIVERSIDAD DE MÁLAGA

$$F_{iIz} = \rho \int_{V_c} \frac{\partial \vec{\omega}}{\partial t} x \vec{e}_z dV \,, \tag{6.22}$$

$$\begin{aligned} F_{ioz} = & -\rho \int_{S_1} v_x \omega x \vec{e}_z dz + \rho \int_{S_2} v_z \omega x \vec{e}_z dx \\ & + \rho \int_{S_3} v_x \omega x \vec{e}_z dz - \rho \int_{S_4} v_z \omega x \vec{e}_z dx \,, \end{aligned} \tag{6.23}$$

$$\begin{aligned} F_{iRez} = & -\mu \int_{S_1} \left(\omega - x \frac{\partial \omega}{\partial x} \right) \vec{e}_z dz - \mu \int_{S_2} x \frac{\partial \omega}{\partial z} \vec{e}_z dx \\ & + \mu \int_{S_3} \left(\omega - x \frac{\partial \omega}{\partial x} \right) \vec{e}_z dz + \mu \int_{S_4} x \frac{\partial \omega}{\partial z} \vec{e}_z dx \,, \end{aligned} \tag{6.24}$$

$$F_{iVz} = \rho V_s \frac{d^2 h_y}{dt^2} \vec{e}_z \,, \tag{6.25}$$

where the lift and drag coefficients (C_{Li} and C_{Di}) are given by:

$$C_{Di} = \frac{F_{ix}}{\frac{1}{2}\rho U_\infty^2} = \frac{F_{ivx} + F_{iIx} + F_{iox} + F_{iRex} + F_{iVx}}{\frac{1}{2}\rho U_\infty^2} = C_{Div} + C_{DiI} + C_{Dio} + C_{DiRe} + C_{DiV} \,, \tag{6.26}$$

$$C_{Li} = \frac{F_{iz}}{\frac{1}{2}\rho U_\infty^2} = \frac{F_{ivz} + F_{iIz} + F_{ioz} + F_{iRez} + F_{iVz}}{\frac{1}{2}\rho U_\infty^2} = C_{Liv} + C_{LiI} + C_{Lio} + C_{LiRe} + C_{LiV} \,, \tag{6.27}$$

The original IF is based on the whole volume without limits, as we can see in (6.10)-(6.15). Therefore, there is an additional problem when evaluating the contribution of the vortex strength that depends not only on the intensity of the vortex generated near the solid but also on the distance between the object and the location of the vortex. Hence, the definition of $\vec{F}_{io}$ (6.13) implies that weak vortices should have a large impact on the force calculation if they were far from the object. This implication has already been reported (see, for example, Graham et al. [129]), and the most common approach is to use only the data before the first vortex leaves the (experimental) spatial domain. This limitation does not allow us to use this technique in many interesting problems (as shown in the forward flight configuration). For this reason, experimentalists must use large domains that will claim an increase in image resolution to obtain good results, which makes this sometimes unrealistic for any experimental configuration. This problem is solved by adding the term $\vec{F}_{io}$ presented in Martín-Alcántara and Fernandez-Feria [128], making this theoretical approach suitable for any bounded spatial domain, as shown in Fig. 6.1. Finally, the reader must note that the term $\vec{F}_{iVz}$ is obtained by processing the images from the recording in our calculations, and

UNIVERSIDAD DE MÁLAGA

later we use $\vec{F}_{iVz}$ to synchronize the signals from different experiments. This is valid only for a non-inertial frame of reference.

The different surface integrals (lines) used to compute the terms C_{Lio} and C_{Dio} have been calculated through the Simpson rule. In contrast, the integral of the impulse formulation terms, containing $\partial\omega/\partial t$, has been computed using the slope of a linear fit in five instants around the current time value (two before and two after) at each point in space. This calculation avoids any noise source from 2D-PIV measurements or any error from 2D numerical simulations.

6.3 CFD

We used the software OpenFoam to numerically calculate the unsteady and laminar flow over a square cylinder in water with an incident velocity equivalent to a Reynolds number of 100, defined on the square side length L,

$$Re = \frac{UL}{\nu}, \tag{6.28}$$

where U is the incident velocity and ν the kinematic viscosity. OpenFoam solves the Navier-Stokes equations using the finite volume method. The method used is second-order accurate in space and to solve the time evolution, a Crank-Nicholson method is used which has a second-order precision. The computational domain is shown in Fig. 6.2. It is centered in the center of the square cylinder and has a region of $3L$ upwards and $10L$ downwards. The upper and lower limits of the domain are placed at a distance of $3L$ from the square. On the left side, a fixed velocity U is imposed, whereas at the rear side we impose an outlet boundary condition. The boundary conditions at the upper and lower sides allow slipping of the fluid. The meshes are created in *Gmsh*, and are defined in such a way that the finite volume cells are regular squares. To allow comparison between meshes, we have used the number of squares (n) per length L. In Fig. 6.2 we show the mesh for the case where we discretize for a value of $n = 10$, that is to say, 10 divisions per L together with the different boundary conditions.

To check the accuracy of the simulation we obtain the values of the drag D and lift L forces produced on the square cylinder. The results for the $n = 30$ mesh, that is the one used in the following sections, are presented in Fig. 6.3. The drag produced over the cylinder reaches a permanent oscillation between $[D_{min}, D_{max}]$ and the lift between $[L_{min}, L_{max}]$ with a null average. The non-dimensional time is defined as

$$\tau = \frac{tU}{L}. \tag{6.29}$$

UNIVERSIDAD DE MÁLAGA

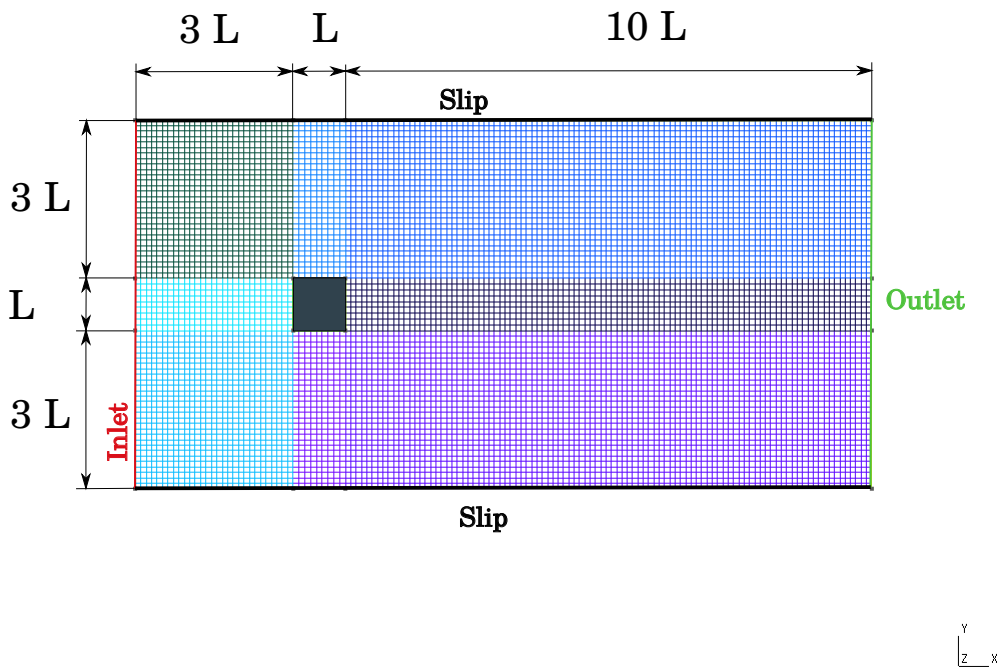

Fig. 6.2 Sketch of the geometry defined for the problem. It is also shown the square mesh created for the case of 10 divisions per L.

Finally, we compare these results for different meshes in Fig. 6.4. It can be observed that the results for the $n = 30$ mesh is able to predict those values with an error of less than 0.25% for the drag, and 0.45% for the lift. We finally will choose this mesh for the rest of the analysis.

The resulting numerical velocity fields are interpolated into the mesh that will be used to mimic the (limited) spatial domain in which we perform virtual 2D-PIV measurements. This grid can range from the same resolution used to perform the CFD ($L/30$) to more coarse grids for testing the influence of this parameter in the force calculations. The domain size is also modified to check the robustness of the indirect force calculation on the square along with the optimal size of the interrogation windows used in 2D-PIV. The flow patterns present for Re=100 shows the characteristic Von Karman Vortex street, where the free shear layers behind the square roll up and form eddies as depicted in Fig. 6.5.

UNIVERSIDAD DE MÁLAGA

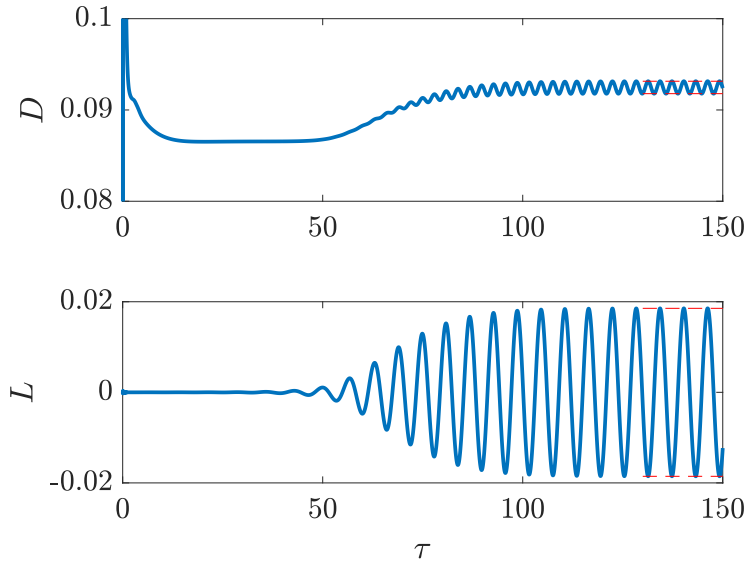

Fig. 6.3 Drag and lift on the square cylinder versus time, for the mesh with $n = 30$ divisions for each L. In dashed red line are marked the values to calculate the maximum and minimum drag and lift, $[D_{min}, D_{max}]$ and $[L_{min}, L_{max}]$ respectively, for $\tau \geq 130$.

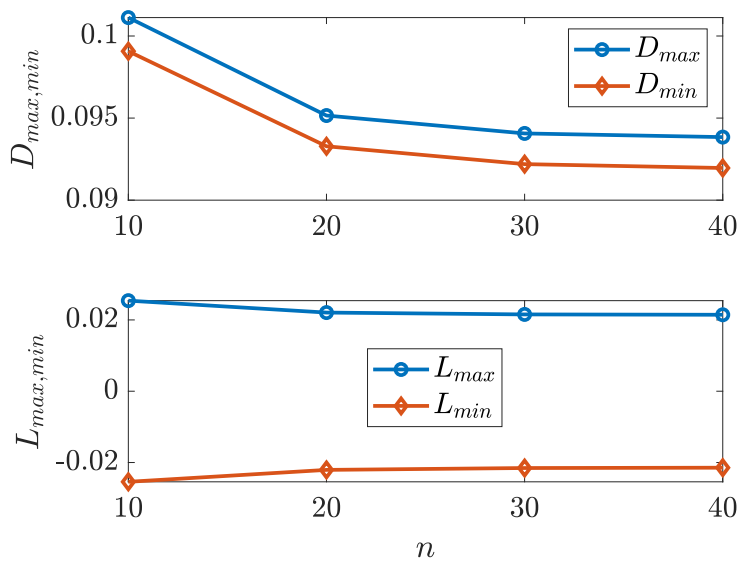

Fig. 6.4 Maximum and minimum drag and lift on the square cylinder, increasing the size of the mesh n.

UNIVERSIDAD DE MÁLAGA

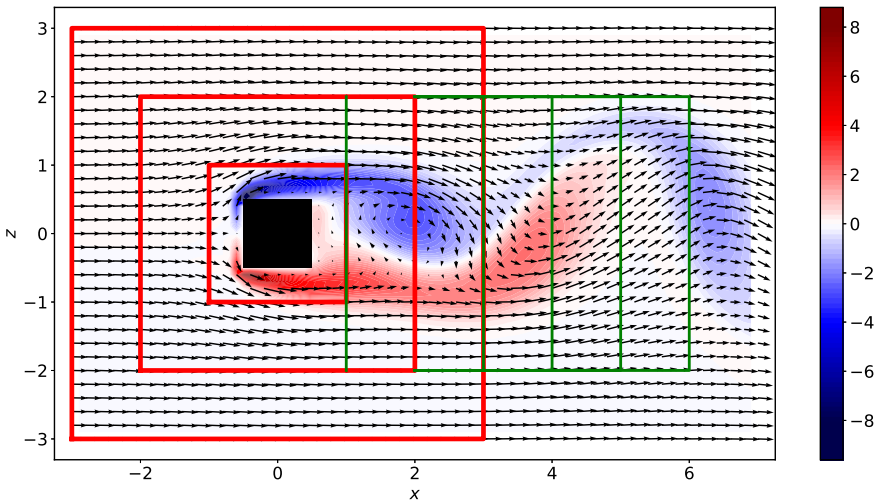

Fig. 6.5 Instantaneous flow field around square cylinder from CFD simulations, interpolated on $h = 0.1c$ grid. For the sake of clarity only one every two velocity arrows are shown. Colors indicates non-dimensional vorticity computed using circulation method [5]. Red and green rectangles indicates computational domains for Figs. 6.6 and 6.7.

6.4 Results

For the calculation of the pressure in the formulation of the moment balance, the pressure is obtained from the numerical calculation but not from the Laplacian operator. We then compare the numerically calculated forces in the flow domain with the approximations of the forces provided by the momentum balance and the impulse formulation. This comparison is carried out for different grid resolutions and window domain sizes by computing the root-mean-square deviation (RMSD) value. This is useful to have a quantitative estimation of the error in the indirect measurement of the force by using the momentum balance and the impulse formulation. The RMSD is given by the following expression

$$\mathrm{RMSD} = \sqrt{\frac{\sum_{i=1}^{N} (\mathrm{PIV}_i - \mathrm{CFD}_i)^2}{N}} \tag{6.30}$$

where N is the total number of time steps, and the force obtained from the numerical simulation (CFD) is selected as the baseline to calculate the error.

First, Fig. 6.6 shows the variation of RMSD by varying the size of the side of the square centered on the object shown in red in Fig. 6.5. Secondly, Fig. 6.7 shows the variation of RMSD by varying the size of the largest side of the rectangle centered on the object shown

UNIVERSIDAD DE MÁLAGA

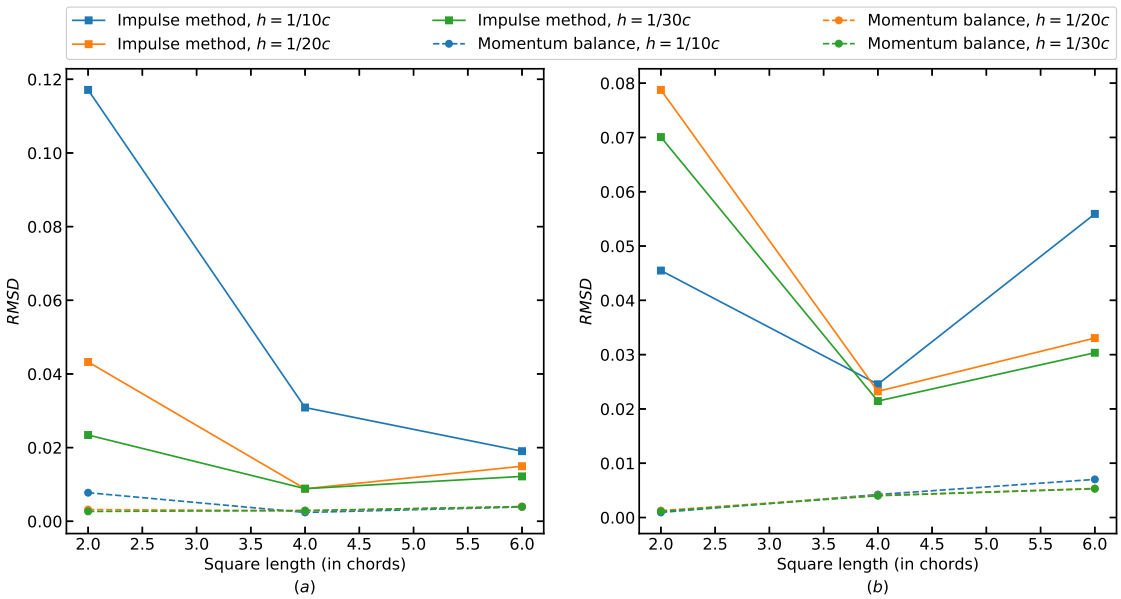

Fig. 6.6 RMSD of the drag (a) and lift (b) coefficients using the impulse formulation (solid line) and the momentum balance (dashed line) for different computational domains (red squares in Figure 6.5).

in green in Fig. 6.5 and starting at x=-2. In both Figs. in (a) the drag coefficient is presented and in (b) the lift coefficient.

One can observe in the Figs. 6.6 that the calculation of moment approximation obtains more precise results for the smallest computational domain, but it is practically independent of the size of the domain, and it works very well in all cases, as much for the case of the calculation of the drag as for the lift. The momentum approach gets its optimum for domain windows defined approximately between $-2 < x < 2$ and $-2 < z < 2$. We can also see how the force estimation becomes more accurate by increasing the grid resolution up to h=1/10c, except for one point not consistent in the lift calculation. The difference is not as large and almost negligible for more than 20 points per chord. Taking into account all this information, we recalculate the RMSD for a constant height domain $-2 < y < 2$, starting at x=-2. Thus, we change the position of the right limit to see if an increase in the domain only in the stream direction will increase the accuracy. This is shown in Fig. 6.7.

This may be counter-intuitive, but the predictions of the aerodynamic coefficients are better for the smaller spatial calculation domains that follow the direction of flow. This could perhaps be explained by the propagation of integral errors, but it is still a not very satisfactory answer for the impulse formulation, where predictions provide very good results. On one hand, the impulse formulation is more robust than the momentum balance regarding the size of the spatial calculation domain but, on the other hand, the former method is strongly

UNIVERSIDAD DE MÁLAGA

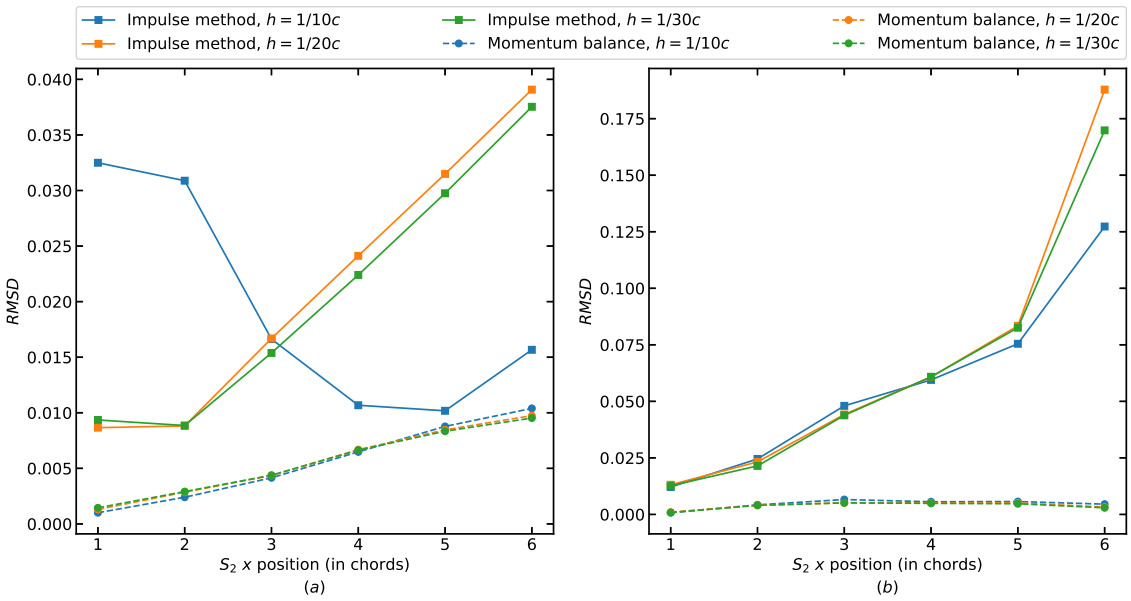

Fig. 6.7 RMSD of the drag (a) and lift (b) coefficients using the impulse formulation (solid line) and the momentum balance (dashed line) for different computational domains (green rectangles in Fig. 6.5).

dependent on distance. Increasing the resolution of the grid decreases the error in most cases, but we can find acceptable results even for the closest grid as can be seen in Fig. 6.8. In this figure the forces in both directions have been presented with the three approximations (momentum, impulse and numerical data) for a computational domain $-2 < x < 2$ and $-2 < z < 2$. It is seen that the difference in the absolute scale is very small for F_x and F_z. It must be taken into account that the differences of the force signals do not depend on time, and instead there is a small delay in the mean value of the magnitude F_z.

Using again the domain size $-2 < x < 2$ and $-2 < z < 2$ for h=1/20, both approaches give reasonably accurate results, however, as long as the momentum balance approach is more robust and gives less errors for all cases, it seems more appropriate to use. Besides, one feature should be noted: momentum balance has a higher computational cost than the impulse formulation because of the need to calculate the pressure.

In Fig. 6.9, we show each term for the momentum balance and the impulse formulation for this optimum domain size. If we pay our attention to the component F_x, in Figs. 6.9 (a) and (c) it is shown how the final result is the same as already seen in Fig. 6.8. The common component that contributes less to F_x is the viscous force in both approaches and neither contribute in both cases the terms with temporal derivatives which correspond to the impulse term F_{iI} and the non-stationary term of the momentum balance F_{mV}. However, there are terms that are similar in relation to the final (positive and negative) contribution. A positive

UNIVERSIDAD DE MÁLAGA

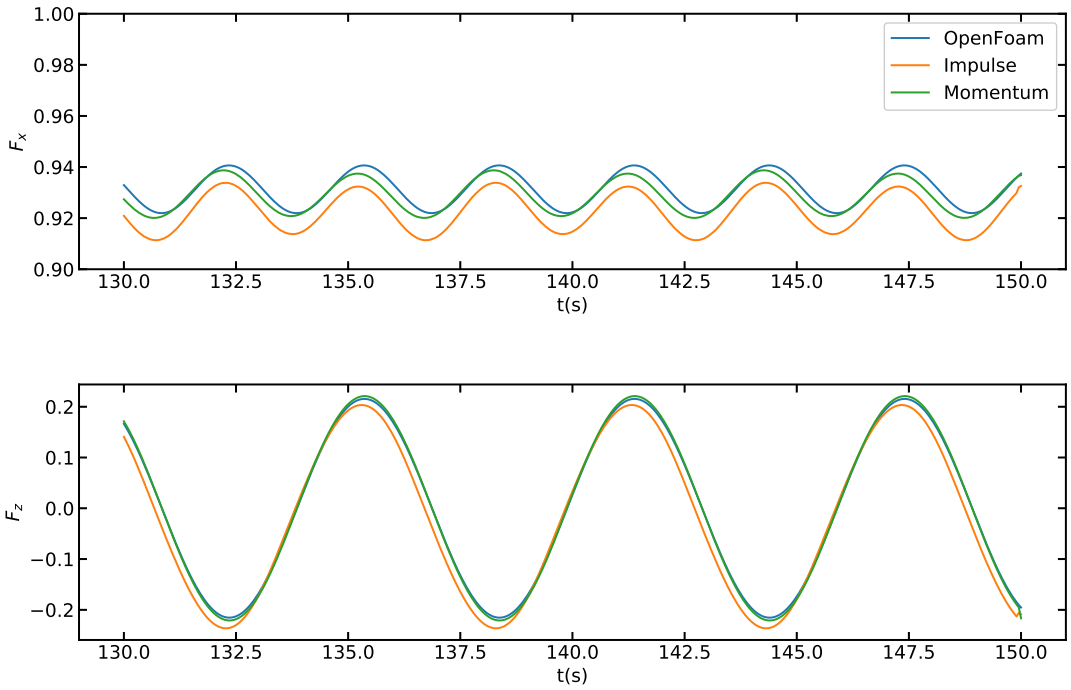

Fig. 6.8 Forces signal computed for h=1/20, and using the square domain $-2 < x < 2$ and $-2 < y < 2$.

contribution of the term F_{iI} in the case of the impulse formulation has its counterpart in the term of the output surface F_{io} where the wakes have a greater influence [128] and the term of pressure F_{mp} in the case of the formulation of the momentum balance. These two terms, F_{io} and F_{mp}, are considered key and must be well calculated for a good execution of both approaches. In addition, the main negative contribution of the impulse formulation is made by the Lamb's vector term that has its equivalent in the convective term of the approximation through the momentum balance. In relation to the force F_z it is observed in Figs. 6.9 (b) and (d) that the total contribution is represented in continuous black line, and the good agreement has already been seen in the detail shown in Fig. 6.8. As for the contribution of each term, a greater complexity is observed in the case of the impulse formulation versus the momentum balance. On the one hand, in the case of the momentum balance, the terms F_{mz} and F_{mV} are counterbalanced and the contribution of viscosity is practically negligible, the pressure term F_{mp} being the one that coincides almost 100% with the temporal evolution, that is, $F_{mz} \approx F_{mp}$. On the other hand, in the impulse formulation, a more complex combination is necessary because the term at the output F_{io} is greater and counteracts with a 180° delay to

UNIVERSIDAD DE MÁLAGA

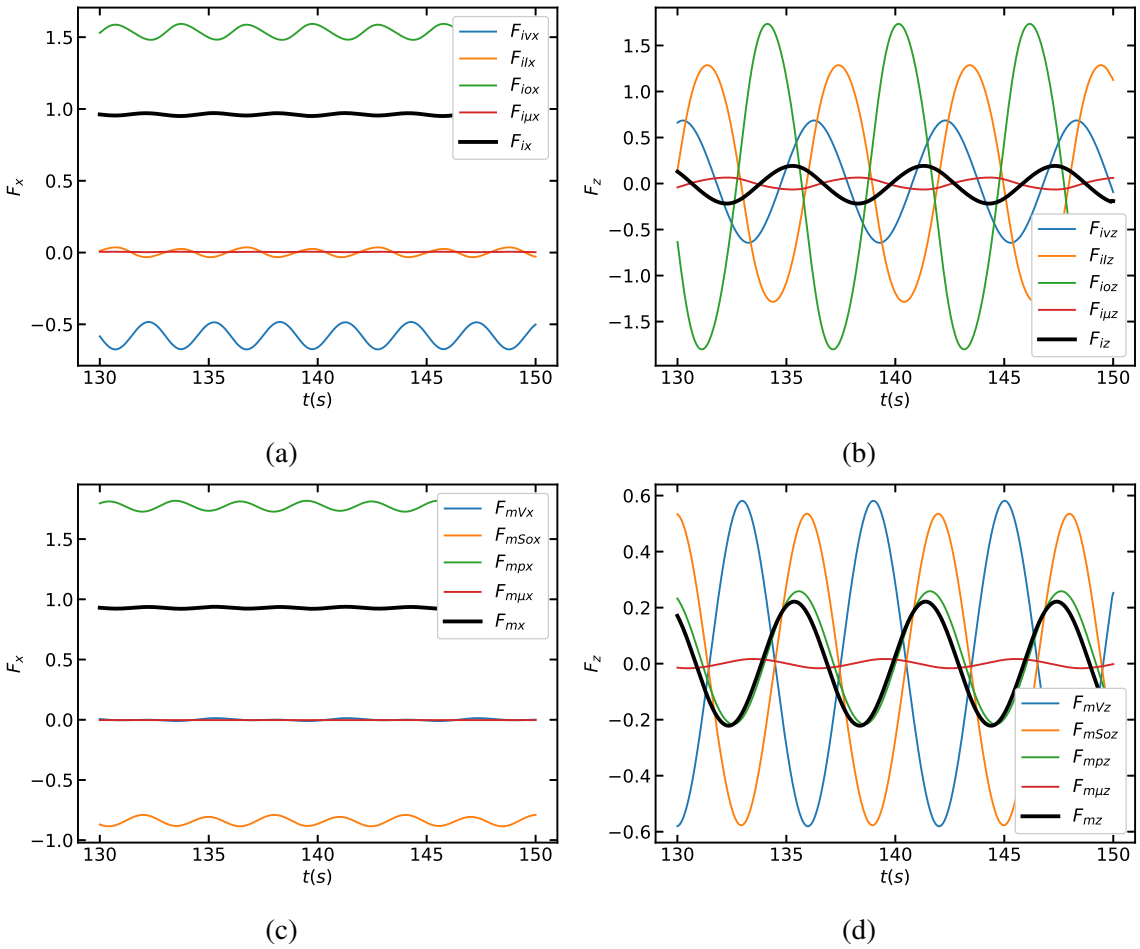

Fig. 6.9 Integral terms for drag and lift coefficients using the impulse formulation (a)-(b) and the momentum balance (c)-(d).

the impulse signal of the term F_{iI}, while the viscous term is almost negligible. It is precisely the remaining F_{io} that is again counterbalanced by the term F_{iv} this time with a 90° offset.

To address why the impulse method is so susceptible to the meshing used, we will discuss how each term performs in two different spatial domains where force prediction actually fails. Both configurations are shown in Figs. 6.10 (a) and (b). The first configuration is defined in the domain $-1 < x < 2$, $-1 < y < 1$, where vortices travel along the upper and lower surfaces without leaving the domain. For this reason, the higher magnitude F_{io} is not perfectly off-phase by 180° with the F_{iI} signal, nor by 90° with the temporal evolution of F_{iv}. For this reason, there is an increase in the value of F_{iz} with respect to that expected. The second configuration is defined with a spatial domain that has as limits $-3 < x < 5$, $-3 < y < 3$, where the vortices do not reach the upper and lower limits. In this case the signal is periodic but antisymmetric and, although it has the phase offsets at 180° (F_{io} and

UNIVERSIDAD DE MÁLAGA

F_{iI}) and 90° (F_{io} and F_{iv}) the final force F_{iz} is lower than expected because the contribution of the terms (and therefore the evaluation of the integral) is much higher in absolute terms. By having to subtract different terms with very large values, the accuracy of the final signal F_{iz} is decreased. In Fig. 6.10 (c) we also compared F_{iz} for both configurations against the calculated CFD reference.

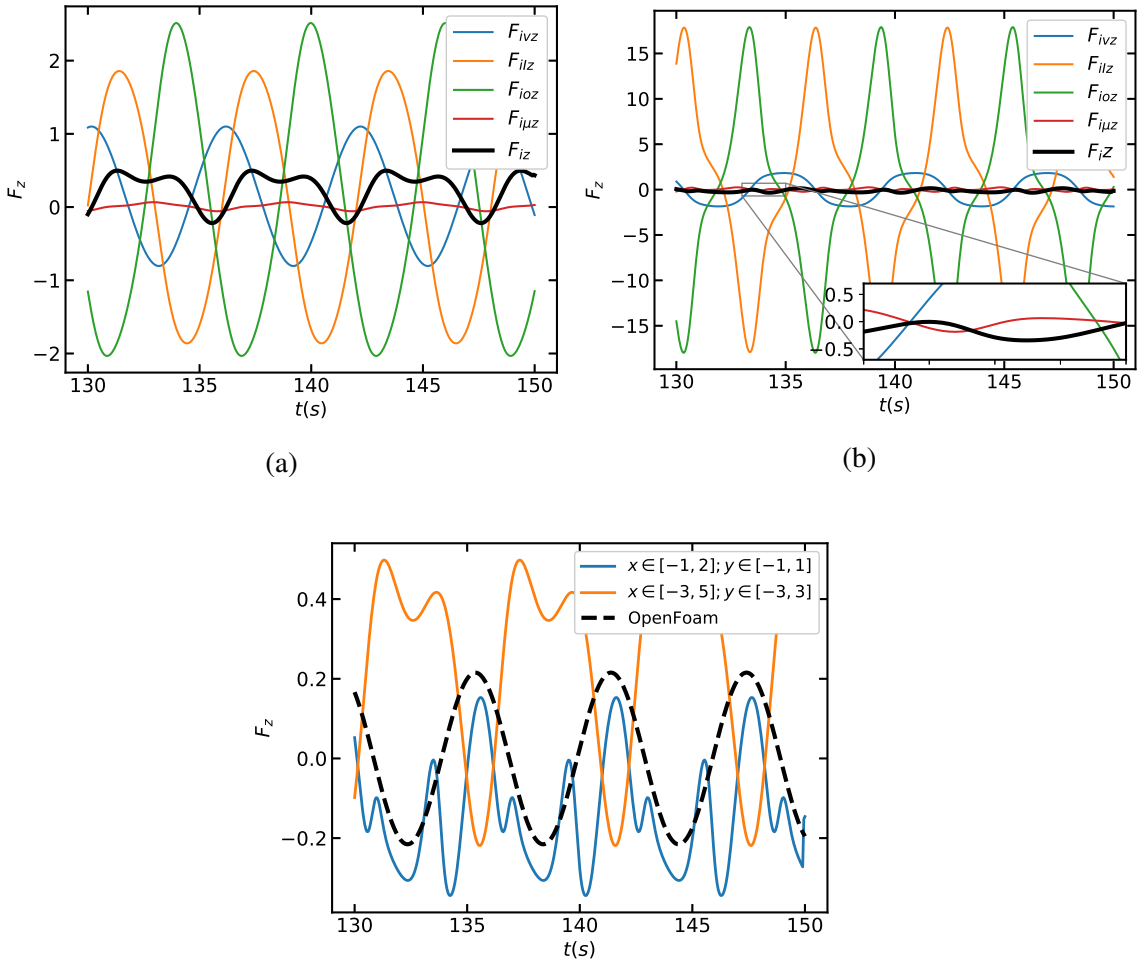

Fig. 6.10 Impulse integral terms for lift in two failing cases: (a) windows domain from $-1 < x < 2$, $-1 < y < 1$, and (b) $-3 < x < 5$, $-3 < y < 3$. In (c) both solutions are compared with Openfoam base signal.

As shown above, these two spatial domains correspond to two completely different situations. In the first case, $-1 < x < 2$, $-1 < y < 1$, the vortices are traveling along the upper and lower surfaces without completely leaving the domain, and this seems to generate invalid data in the integrals evaluated in it, which generates a non-sinusoidal resulting signal as can be seen in Fig. 6.10 (a). In the second case, $-3 < x < 5$, $-3 < y < 3$, the spatial

UNIVERSIDAD DE MÁLAGA

domain has a higher height to avoid vortices traveling along it ($-3 < y < 3$), and a distance in the direction x of the incident flow much higher. As a result, the value of F_{iI} and F_{io} increases as the domain does, but the real force does not, this means that the total force is two orders of magnitude less than the terms to be added causing a great increase of uncertainty.

6.5 Conclusions

We have computed the forces on a submerged body using two different approaches, the momentum balance and the impulse formulation, but taking into account the vortices coming out of the downstream domain to overcome the limitation of a restricted spatial domain.

In our test, the momentum balance proved to be a much more robust and accurate way to obtain forces on submersed bodies. The main drawback is the higher computational cost due to the need to solve the laplacian pressure for each time step and the possible sensitivity of the experimental noise that will surely affect this pressure assessment. On the other hand, the impulse method needs a careful selection of the window domain to work properly. If this selection is done rigorously, reasonably accurate results are obtained, but always slightly below the current balance.

Taking all this into account, the impulse formulation is more suitable for obtaining precise results. An additional advantage of this method is the ability to obtain information about the contribution of the vortex structures to the forces that evaluate the integers in terms of F_{iv} and F_{iI}. As an example, in the Fig. 6.11 we show the elevation integers of these two terms for the same time given in the Fig. 6.5.

UNIVERSIDAD DE MÁLAGA

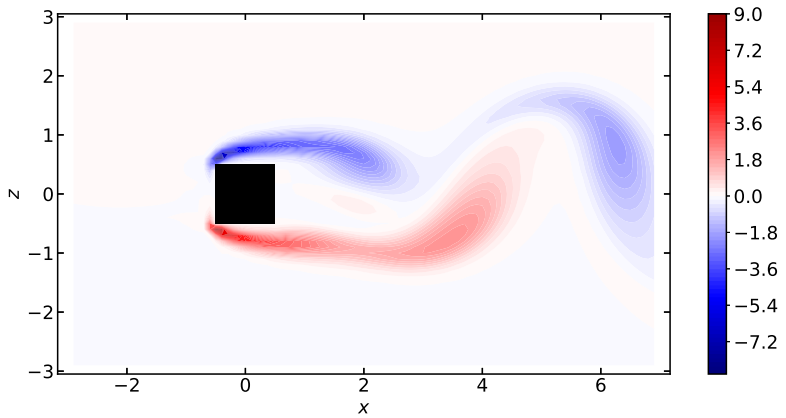

(a)

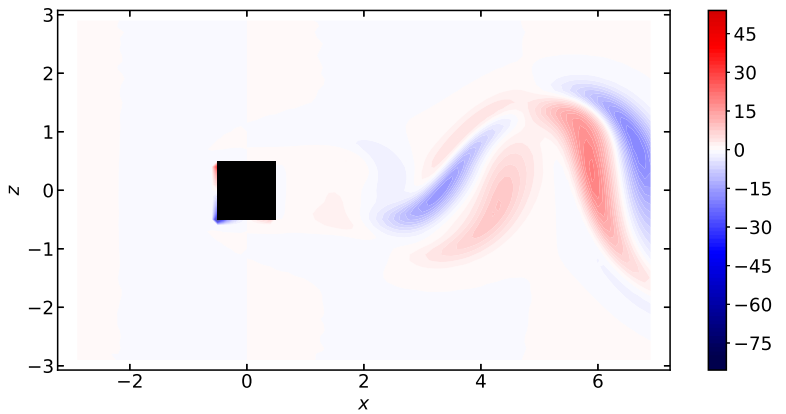

(b)

Fig. 6.11 Contours of vortical contribution to lift force in the impulse formulation: (a) F_{iv} and (b) F_{iI}.

UNIVERSIDAD DE MÁLAGA

Chapter 7

Application of the impulse formulation to an experimental flapping flat plate.

7.1 Background

As we have seen in the previous chapter, the impulse formulation approach has only given acceptable results within a certain range of limits associated with the spatial domain. The final spatial domain window chosen for this chapter was approximately the one that gave the best result in reducing the error made with the synthetic images of the numerical simulations, that is, from -0.8 $\leq x \leq$1.3 and -1.11 $\leq z \leq$1.11 (see the experimental setup description below).

The forces generated by a flapping wing in a uniform flow have been studied widely from theoretical, numerical, and experimental points of view [29]. The understanding of thrust generation by the simple idea of flapping a rigid plate with a zero angle of attack was first examined by Wang [136] using computational fluid dynamics (CFD). In that work, the Navier-Stokes equations are solved with a vorticity-velocity formulation for different values of St_a and St_c (characteristic frequencies of the movement, which are described in detail below), finding St_a=0.2 and St_c=0.7 the most efficient combination in the forward flight. Lewin and Haj-Hariri [137] developed a similar work. They conducted numerical simulations to reproduce the problem of a heaving airfoil, finding larger efficiency values than those given by Wang [136], for being an airfoil more aerodynamic than an elliptic wing. Surprisingly, the most efficient flight was again found for the same pair of values St_a and St_c given in Wang [136]. Furthermore, periodic, quasi-periodic, and aperiodic flow behaviors were distinguished in that work.

UNIVERSIDAD DE MÁLAGA

More recently, Martín-Alcántara et al. [138] found the Leading- and Trailing-Edge Vortex (LEV and TEV, respectively) contributing to thrust in the flow around a heaving ellipse. These structures were examined numerically in two dimensions employing a vortex-force decomposition by using the software OpenFOAM, and thrust generated was mainly formed during the development of the LEV and the shedding of the TEV. The influence of the average angle of attack is not relevant for efficiency, but for the flow dynamics. The most considerable efficiency is found at St_a=0.20 and St_c=0.81 for a null angle of attack which are very close to those reported in Wang [136]. Besides, other authors have been studying the impact of LEVs on flow patterns and instantaneous aerodynamic forces, see Hubel and Tropea [139], Moriche et al. [140], Martín-Alcántara and Fernandez-Feria [128]. Despite the application of digital sensors to measure the force, the fundamentals to determine the force from experimental velocity fields are still a challenge in fluid dynamics Wu et al. [135]. The main objective of this research is to present a good (2D) theoretical approach, with its disadvantage mainly related to drag estimation.

In summary, we use the IF formulation presented in Chapter 6 on a real 2D-PIV experiment on a rigid flat plate at zero angle of attack. This technique developed by Wu et al. [133, 134, 135], and which was already used numerically in Martín-Alcántara and Fernandez-Feria [128] with the correction vorticity leaving the domain, is applied into a real non-stationary PIV experiment for forward flight and for hovering case which has not been studied before in the State of Art. Our results are compared with those obtained by direct force measurements with a force sensor. This experimental procedure is a potential candidate to estimate instantaneous aerodynamic lift in both configurations.

7.2 Experimental setup

We performed the experiments using the towing tank University of Málaga with dimensions 500×500 mm^2 section area and 10000 mm length. We used a flat aluminum plate of $30 \times 300 \times 1.5$mm (chord, length, and width respectively) located horizontally at 250mm of depth. No structural flexibility was observed in the flapping flat plate within the reduced frequencies analyzed.

The oscillation movement of the flat plate was created using a stepper motor and a straightforward crank handle system, as depicted in the inset of Fig. 7.1. Forces were measured with a precise digital force sensor (Schunk FTD-Nano 17 SI-12-0.12) that holds the wing model from outside the water. The transducer (3) measures forces in three dimensions in the range of 12N$\pm$0.004N for x-direction and 17N$\pm$0.004N for z-direction.

UNIVERSIDAD DE MÁLAGA

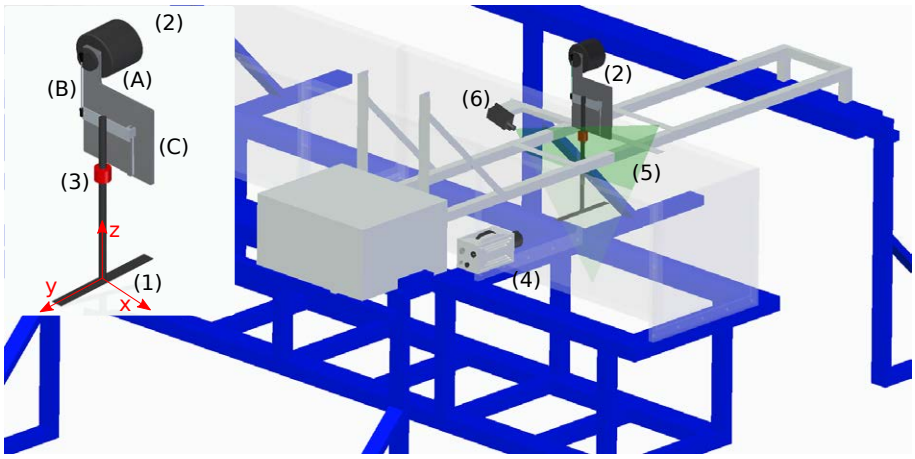

Fig. 7.1 Experimental setup layout: flapping flat plate (1), rod-crank shaft movement system (2), digital force sensor (3), high-speed camera (4), laser sheet (5), continuous laser source (6). A detail of the rod-crank shaft movement system (2) is given in the inset: DC motor (A), rod (B), and guide rail (C). The whole system (1)-(6) moves together from right to left in the schedule in the forward flight configuration.

To compensate inertia forces, we have repeated the identical experiment on air, so the force sensor directly measured inertial forces. The buoyancy force was obtained from water density, and the position of the flat plate was collected from the same images while performing 2D-PIV. We obtained aerodynamic loads by subtracting the inertia and buoyancy forces to those obtained from the experiment inside the water. Measured forces shown below were filtered with a cutoff frequency of 4 times the oscillation frequency and phase-averaged.

The PIV equipment consisted of a Fast-CAM Photron SA3 that recorded 1024 by 1024 pixels images up to 1000 fps though only 125 fps have been used in this work. Only one laser is shown in Fig. 7.1, but we made use of three continuous lasers of 500mW each, with a set of cylindrical lenses of -6.25 mm focal length to generate a sheet of 1 mm thick. We used a Nikon 105 mm lens (model AF Micro Nikkor 105mm) and f/2.8. The lasers were aligned to generate a single plane. The shadows generated by the wing were overcome with a mirror and the correct angular position of the lasers. The presence of the mirror also helped to increase sheet intensity. The tracers for the PIV were silver coated hollow glass spheres of $10\mu m$. The 2D laser plane was placed at $0.65L$ along the direction of the wing advance. All the equipment for the experiment is mounted on the towing tank's rails, as shown in Fig 7.1. Thus, the flat plate, camera, and lasers were moving forward during the flight configuration experiment. The associated cartesian coordinate system was defined as follows: y and z-coordinates are spanwise and transverse (wall-normal) directions, respectively. The x-coordinate is the streamwise direction defined along the free stream.

UNIVERSIDAD DE MÁLAGA

Velocity and acceleration of the moving flat plate were derived from the position signal. The trigger of the camera launched the force sensor with a 50 ms delay. There is no synchronization with the crank-rod system since the instantaneous position of the flat plate was obtained from the video recording, as mentioned above. The forward flight configuration started previously to the image recording during at least 50 periods along with the towing tank. In the hovering case, the record begins before the crank-rod system was activated, and we only made use of the two first cycles in our results.

We obtained the velocity field using a custom adapted version of the multi-pass with windows software DPIVSoft, developed by Meunier and Leweke [34], that has been tested in rotating flows successfully Lagrange et al. [35], Albrecht et al. [36], García-Ortiz et al. [37]. Different sizes of windows were used to optimize the results, and finally, we have chosen 32-pixel square correlation windows and 50% overlap. The time step between images was the inverse of the frame rate. The calibration gave a ratio of 94.3 μm/px and 72.6 μm/px in hovering and forward flight, respectively.

We define two Strouhal numbers to characterize the problem: one based its characteristic length on the heaving amplitude, $\hat{h}_0$, and the other on the chord, $\hat{c}$ (the 'hat' symbol is used for dimensional quantities). Both lengths depend on the frequency of the periodic movement that follows approximately equation $\hat{h}$=$\hat{h}_0 \sin\left(2\pi\hat{f}\hat{t}\right)$:

$$St_a = \frac{\hat{h}_0\hat{f}}{\hat{U}_\infty}, \tag{7.1}$$

$$St_c = \frac{\hat{c}\hat{f}}{\hat{U}_\infty}. \tag{7.2}$$

We imposed $\hat{h}_0$=7.4 mm and $\hat{f}$, the frequency of oscillation, was set to 0.501 and 1.020 Hz in the experiments. It must be noticed that our crank-rod system does not produce a perfect sinusoidal signal, but something very close, as shown in Fig. 7.2.

The Strouhal number St_a is also related to the parameter kh used in Lewin and Haj-Hariri [137] by kh=$2\pi St_a$. Scaling the non-dimensional coordinate $\vec{x} = (x,z)$ with the foil's chord length $\hat{c}$, and time with $\hat{c}/\hat{U}^*$ the non-dimensional movement equation is

$$h(t) = h_0 \sin(2\pi t) = h_0 \sin(2k\tau), \tag{7.3}$$

being $h_0 \approx 0.5$, $t = \hat{t}\hat{f}$, and $\hat{U}^*$ equals to $\hat{U}_\infty$ or $\hat{U}_{max}$ in the forward flight and the hovering configurations, respectively. $\hat{U}_{max}$ is the maximum hovering velocity ($\hat{U}_{max}$=$\pi\hat{f}\hat{h}_0$), and the reduced frequency, k (only valid for forward flight), can be defined as

UNIVERSIDAD DE MÁLAGA

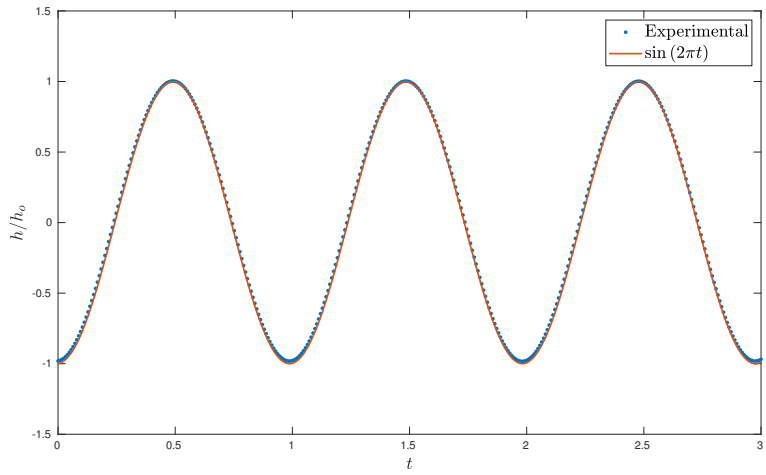

Fig. 7.2 Comparison between experimental tracked movement and a sinusoidal

$$k = \frac{\pi \hat{f} \hat{c}}{\hat{U}_\infty} = \pi St_c \,, \tag{7.4}$$

along with the non-dimensional time $\tau = \hat{t}\hat{U}^*/\hat{c}$.

The Reynolds number in the forward flight configuration is defined as

$$Re = \frac{\hat{U}_\infty \hat{c}}{\hat{\nu}} \,, \tag{7.5}$$

where $\hat{\nu}$ is the temperature dependent kinematic viscosity. Finally, we use the Reynolds number Re_h that corresponds to the hovering case:

$$Re_h = \frac{\hat{U}_{max} \hat{c}}{\hat{\nu}} = \frac{\pi \hat{f} \hat{h}_0 \hat{c}}{\hat{\nu}} \,. \tag{7.6}$$

We analyze four cases: (i) two in flight configurations for values (St_c, St_a, k, kh, Re) = (0.43, 0.11, 2.7, 0.67, 1000) and (0.85, 0.21, 5.4, 1.34, 1000) of great interest because they are near the largest efficiency Martín-Alcántara et al. [138] ; and (ii) two in hovering configuration for values Re_h= 335.2 and 668.7 appropriate for fruitflies, see Wang et al. [141]. Finally, we present all the indirect forces in their dimensionless form using the lift and drag coefficients:

$$C_L = \frac{2\hat{F}_z}{\hat{\rho}\hat{U}^{*2}\hat{c}} \,, \quad C_D \frac{2\hat{F}_x}{\hat{\rho}\hat{U}^{*2}\hat{c}} \,. \tag{7.7}$$

All experimental results are given in non-dimensional way, so impulse terms of Eq. (6.10) can be written in terms of lift and drag coefficients as:

UNIVERSIDAD DE MÁLAGA

$$C_L = C_{Lv} + C_{LI} + C_{Lo} + C_{LRe} + C_{LV} \,, \tag{7.8}$$

$$C_D = C_{Dv} + C_{DI} + C_{Do} + C_{DRe} \,. \tag{7.9}$$

We perform the calculations in a non-inertial reference frame centered on the flat plate chord. We obtain this final experimental frame using spline interpolation and the position of the flat plate in each snapshot, thus reducing the original (available) spatial domain in the z-axis (see Fig. 7.3).

We use two different spatial domains located in the center of the flat plate depending on the flight configuration, forward flight (-0.8 $\leq x \leq$ 1.3 or L_1=0.3, L_2=0.8) or hovering (-1.5 $\leq x \leq$ 1.5 or L_1=L_2=0.5), and where the z-coordinate remains in the same interval -$R \leq z \leq R$ (R=1.11). We shall consider a solid flat plate of volume V_s and surface S_s, whereas the fluid volume V_c has four different surfaces from n_1 to n_4.

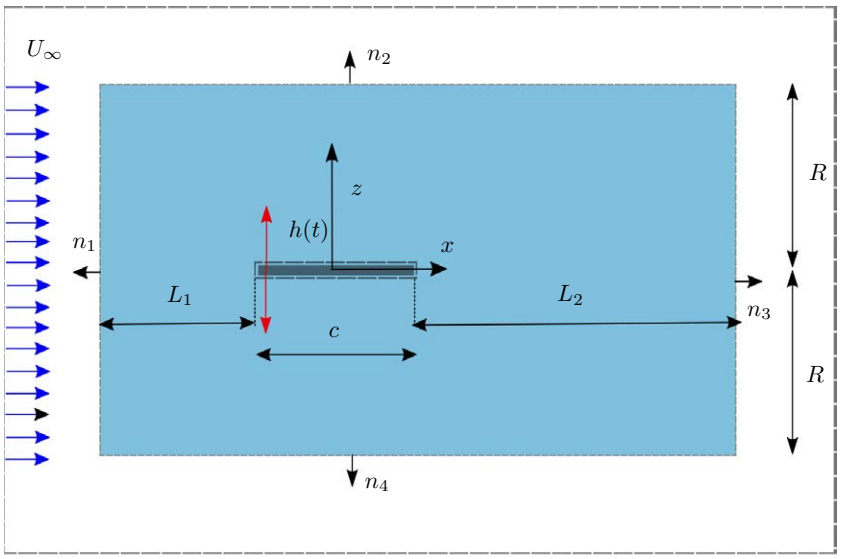

Fig. 7.3 Schematic view of the spatial domain to evaluate the aerodynamic forces on the flat plate.

7.3 Results

7.3.1 Forward flight configuration

The velocity fields have been calculated using the average phase data from eight cycles and three different experiments for each studied frequency. Vorticity is computed by the 9 points circulation based method (see Raffel et al. [5]). We plot in Fig. 7.4 the average

UNIVERSIDAD DE MÁLAGA

velocity and vorticity fields of one experiment and eight cycles starting at h=-h_0 (t/T=0) in the forward flight for Re=1000 with k=2.7 (left column) and k=5.4 (right column). Plots (a) and (b) correspond to t/T=0, (c) and (d) correspond to t =0.25, and the rest of the figures are displayed in increments of t =0.25. We can distinguish big vortex structures of the Leading- and Trailing-Edge Vortices (LEV, TEV), which are responsible for the generation of aerodynamic forces. It is observed that the magnitude of vorticity increases with the reduced frequency of k (see the magnitude of ω in the color bars).

We observe that for $k = 2.7$, the LEV moves by convection downstream. Conversely, it remains attached to the wing for $k = 5.4$.

We pay attention now to the different terms that form the lift coefficient of C_L in Eq. (6.27). In Fig. 7.5, we depict the lift forces' temporal evolution during one average cycle that results from three experiments of eight cycles. We select four different points (1)-(4) over the average cycle in which the signal C_L presents a peak or is null along with the corresponding snapshots of the vorticity where the forces have been computed to explain how the IF theoretical approach works. Firstly, although the term C_{LI} seems to be the most important in the impulse formulation, the correction made by the term C_{Lo} is crucial, becoming both of the same order. The sequence of the peaks (1) and (3) that appear in the term C_{LI} is practically compensated with the term C_{Lo}. At time (1) and (3), the correction comes from the emission of large vortical structures in the outer surface (see snapshots (1) and (3) on the right-hand side). Secondly, the term C_{Lv} takes on some relevance in the total lift, while C_{LRe} and C_{LV} have a weak influence on C_L. These two main characteristics are independent of k.

We test the robustness of the force estimation by using thirteen different volume domains in each experiment. For instance, we depict in Fig. 7.6 only three of these areas which are delimited in the x-axis by surfaces (1), (2), and (3) in the outlet surface S_3.

To have a quantitative estimation of the error in the force induced by this method, we compute again the root-mean-square deviation (RMSD) as

$$\mathrm{RMSD} = \sqrt{\frac{\sum_{i=1}^{N} (\mathrm{PIV}_i - \mathrm{FS}_i)^2}{N}} \tag{7.10}$$

where N is the total number of time steps, and the force obtained from the sensor (FS) is selected as the baseline to calculate the error. RSMD as a function of the position of surface S_3 is shown on the left column of Fig. 7.7 for two reduced frequencies k=2.7 and 5.4. Although the analysis has been made for thirteen experimental areas, the points (1), (2) and (3) have been highlighted in Fig. 7.6 . Finally, we plot the instantaneous lift in the right column of Fig. 7.7. It can be seen from the results that the forces computed using IF

UNIVERSIDAD DE MÁLAGA

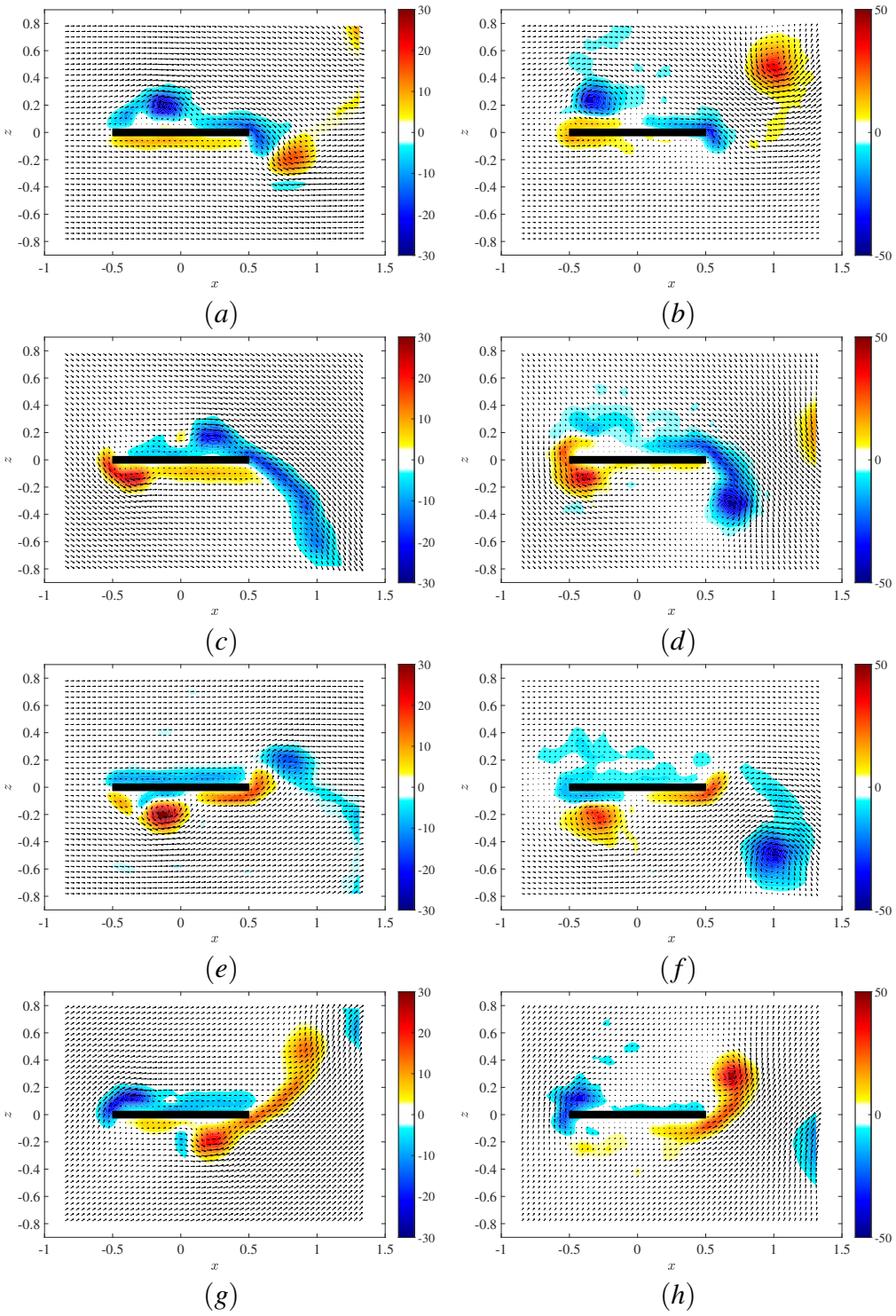

Fig. 7.4 2D-PIV Isocontours of ω for Re=1000 and k=2.7 (left column) and k=5.4 (right column) at h=-h_0 (a)-(b), h=0 (c)-(d), h=h_0 (e)-(f), h=0 (g)-(h).

UNIVERSIDAD DE MÁLAGA

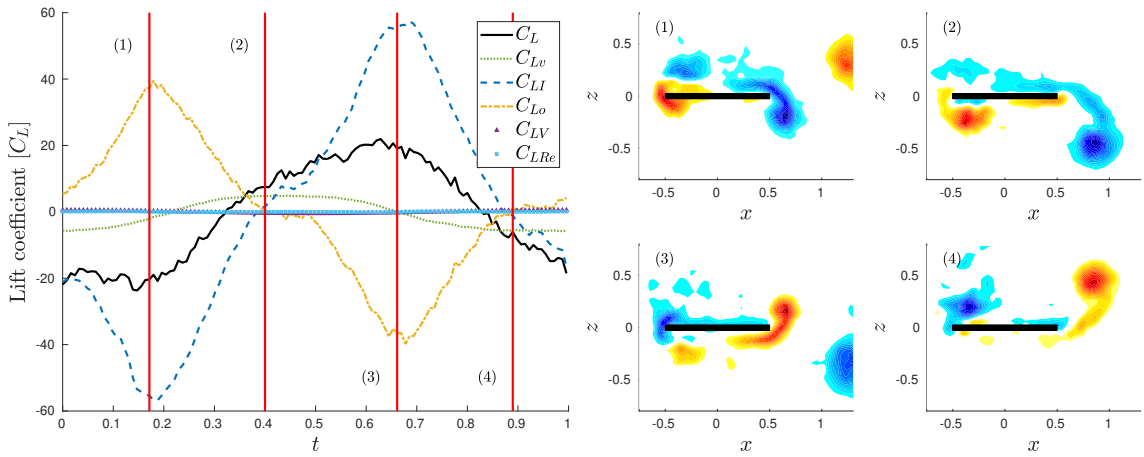

Fig. 7.5 Temporal evolution of each term of IF formulation lift for *Re*=1000 and *k*=2.7 on the left image. (1)-(4) represents 4 instants showed on right side.

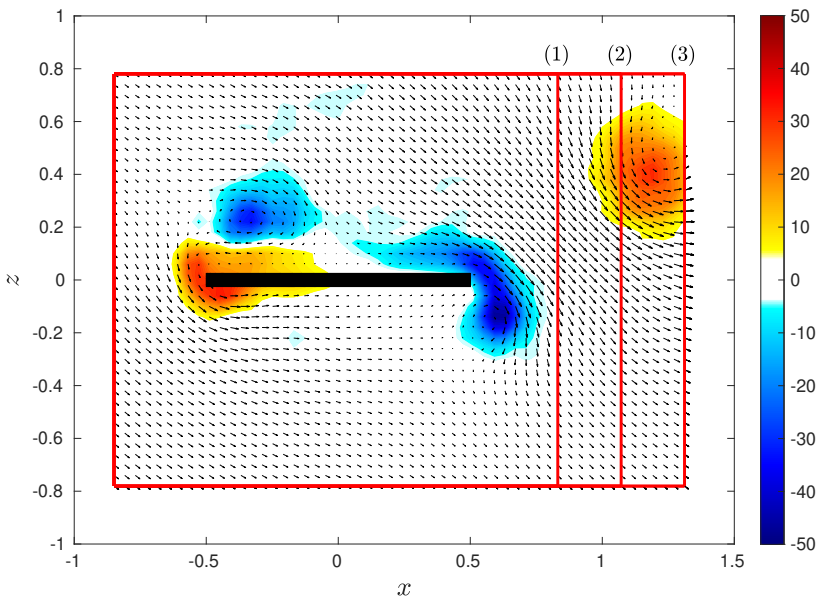

Fig. 7.6 Experimental windows domain used for computation in the forward flight.

UNIVERSIDAD DE MÁLAGA

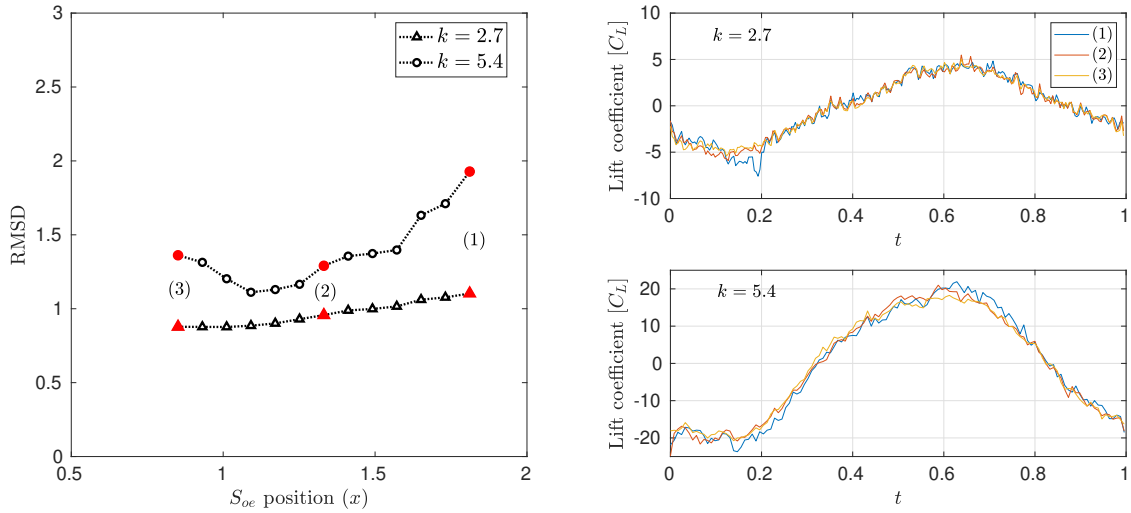

Fig. 7.7 RMSD as a function of the position of surface S_3 on the left column for forward flight experiments. The red points (1)-(3), represents the experimental windows domains shown in Fig. 7.6. Temporal evolution of Lift coefficient is shown on right column for points (1)-(3).

are nearly independent of the size of the windows on the range tested, as we could have expected from our preliminary results on Chapter 6. The calculation of C_L is solid, and the experimental area has practically no influence on the final result given by IF, which guarantees a good experimental procedure in the case of forward flight configuration. We consider the intermediate volume (2) to show the results for the estimation of C_L and C_D. The reader should note that other methods in the literature (Guissart et al. [126], Siala and Liburdy [122]) depend largely on the size of the spatial domain.

Fig. 7.8 represents one cycle that corresponds to the temporal data evolution of lift and drag coefficients for two forward flight cases considered at Re=1000: k=2.7 (a) and k=5.4 (b). The shadow of the Force Sensor (FS) shows the standard deviation of three experiments, while the estimation of the instantaneous aerodynamic coefficients is obtained from the average value of three experiments. The lift coefficient shows good agreement with force sensor measurements, which increases as long as the forces involved increase for higher k. On the other hand, and paying our attention on the drag coefficient, it is observed that the estimation has many uncertainties due to (i) the level of forces involved in the experiment, (ii) the inconvenience of having experimental data near the boundary layer, and (iii) the performance of 2D-PIV measurements while the flow is fully 3D (including trailing vortices). This less accurate result regarding the C_D estimation is also reported in other studies in the State of Art, as explained in the Introduction section. It is naively possible to intuit the

UNIVERSIDAD DE MÁLAGA

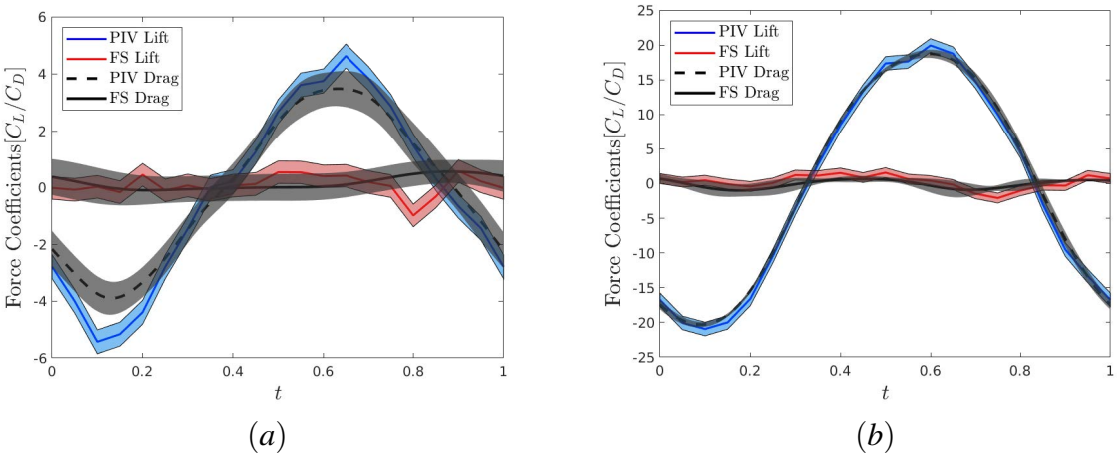

Fig. 7.8 Temporal evolution of C_L and C_D (a)-(b) with different computations (see legend) for Re=1000 and k=2.7 (a) and k=5.4 (b).

production of thrust (negative C_D), taking into account the average signal using IF for the highest k.

Although the results presented in Fig. 7.8 show a reasonably good agreement for C_L, some discrepancies appear for k=2.7 or k=5.4 near the peaks. A possible explanation for this error lies in the fact that this discrepancy occurs at the beginning of the downstroke or upstroke motions, where the flow remains fully attached to the surface of the flat plate see, for example, snapshots (1) and (3) in Fig. 7.5. It is precisely in those times where unfortunately the resolution of the boundary layer and the consequent generation of vorticity is not well resolved by the 2D-PIV. This uncertainty quantification has been also reported before in Siala and Liburdy [122]. Furthermore, the magnification of this discrepancy is highlighted by k=2.7 since the force magnitude is 0.1 N instead of 0.5 N, which is present by k=5.4. In any case, the 2D-PIV results predict quite correct the shape and the values of C_L.

7.3.2 Hovering configuration

We also test IF in the hovering configuration, starting from rest. In this case, we will never get a periodic flow, every cycle will be different, and the influence of the smallest perturbation can increase along time, so only the first cycle can guarantee some repeatability. The velocity field has been phase averaged between the three experiments, providing an average of three values. In general, the margin of error in estimating the forces using IF combined with 2D-PIV in the hovering configuration is higher compared to the forward flight. This higher

UNIVERSIDAD DE MÁLAGA

error is due to both the flow dependency of the initial experimental state and the chaotic mixing process of the generated vortices over time produced from the 2D-PIV measurement window. Also, we noticed that there was a small initial movement around the flat plate due to slight buoyancy forces enhanced by temperature differences (stratified water flow).

We show 2D-PIV instantaneous measurements of one experiment in Fig. 7.9 for Re_h=335.2 (left column) and 668.7 (right column) for the first cycle of the periodic movement starting at h=-h_0 and decomposing the cycle in four snapshots over one period, T, with the same interval $T/4$, corresponding (a) and (b) to t/T=0.25. We observe vortex structures well-captured even near the boundary layer of both edges where the onset and growth of these vortices take place in the oscillating flat plate. Besides, we expect a more intense gradient in the boundary layer near the flat plate as we increase Re_h. This observation is also shown in Fig. 7.9 so we can see a larger area with high vorticity near the solid for Re_h=668.7 (f) in comparison to that computed for Re_h=335.2 (e) in the downstroke.

We depict in Fig. 7.10 the first cycle showing the different terms from IF for Re_h=668.7. Most of the contribution in IF corresponds to the term C_{LI} while the term C_{Lo} starts to become relevant as the vortex structures appear and disappear in the bounded domain, especially in S_2 and S_4, thus correcting mainly the peaks generated by C_{LI}. For this reason, IF follows better the reference signal of the force sensor, as shown below. This correction, however, works better as the Reynolds number increases. A possible explanation for this phenomenon lies in the greater definition of the vortices that diffuse downstream as they move from the plate in the upstroke and downstroke motion, as depicted in snapshots (1), and (4) of Fig. 7.10. Besides, it should be mentioned that the contribution of C_{L0} in the hovering configuration is less than the calculated in the forward flight (compare the term C_{L0} in Figs. 7.5 and 7.10).

As we did on forward flight, we perform an error analysis on the lift coefficient taking into account different windows domains of the same rectangular shape and varying area. Only three areas composed by the limits (1), (2) and (3) are shown in Fig. 7.11.

We depict in Fig. 7.12 the signal RSMD against the area of the domain for two hovering cases, and three computations of C_L corresponding to the highlighted experimental regions (1), (2) and (3). We observe that the experimental window does not influence the final results in the hovering case. However, the magnitude of the RSMD is greater than the one calculated in the forward flight configuration due to the reasons explained above.

Finally, we show in Fig. 7.13 the time evolution of three cycles from the theoretical approximation presented in our study using the staging area (2), together with experimental data obtained from the force sensor. The shaded regions around the signal of the force sensor correspond to the standard deviation of three different experiments. We observe a change in the accuracy depending on Re_h taking into account that the force sensor (black) dashed

UNIVERSIDAD DE MÁLAGA

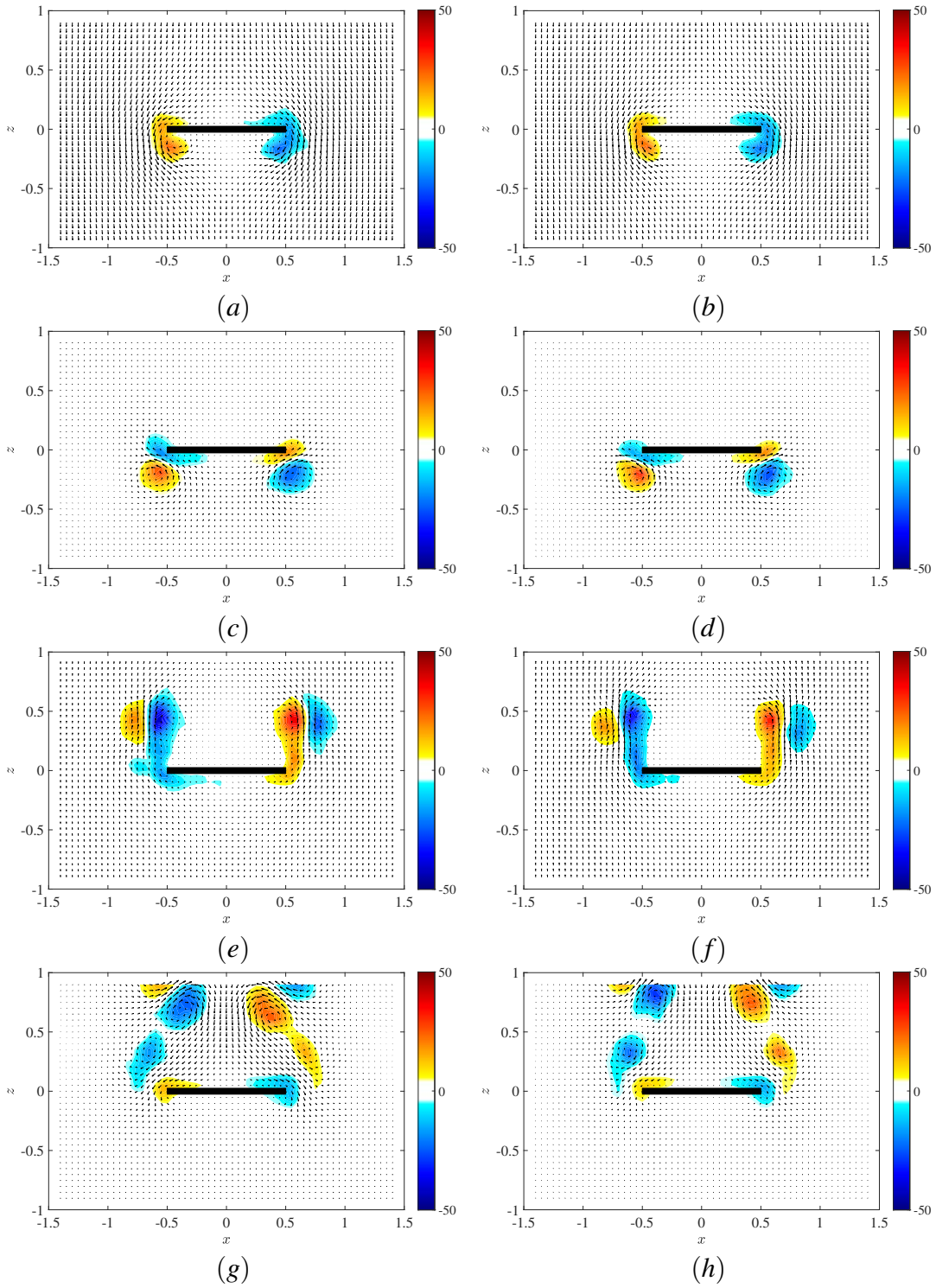

Fig. 7.9 2D-PIV Isocontours of ω for Re_h=335.2 (left column) and 668.7 (right column) at $\hat{h}$=0 (a)-(b), $\hat{h}$=$\hat{h}_0$ (c)-(d), $\hat{h}$=0 (e)-(f), $\hat{h}$=-$\hat{h}_0$ (g)-(h), starting at $\hat{h}$=-$\hat{h}_0$.

UNIVERSIDAD DE MÁLAGA

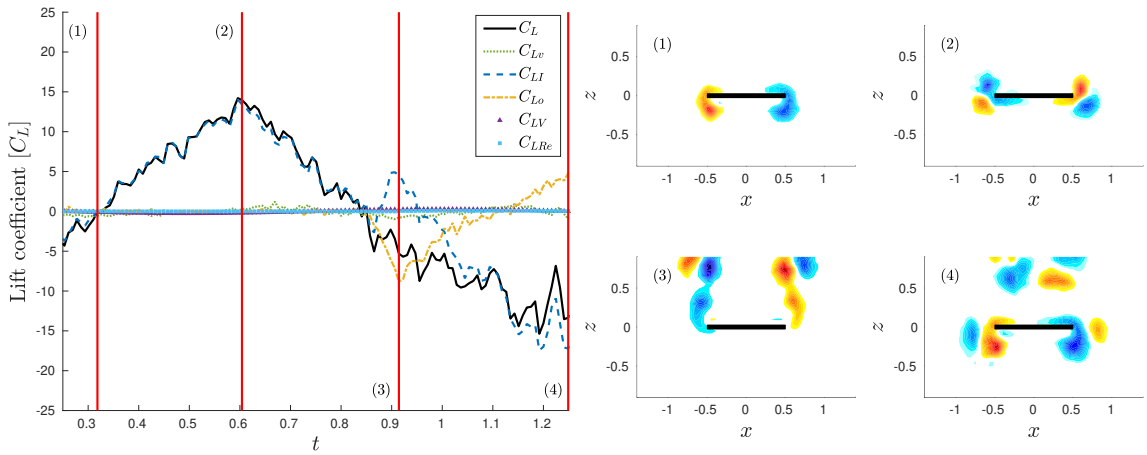

Fig. 7.10 Lift coefficient against time and its corresponding five terms using IF for Re_h=668.7 on the left. (1)-(4) represents four instants and their associated snapshots are presented on the right side using the vorticity magnitude.

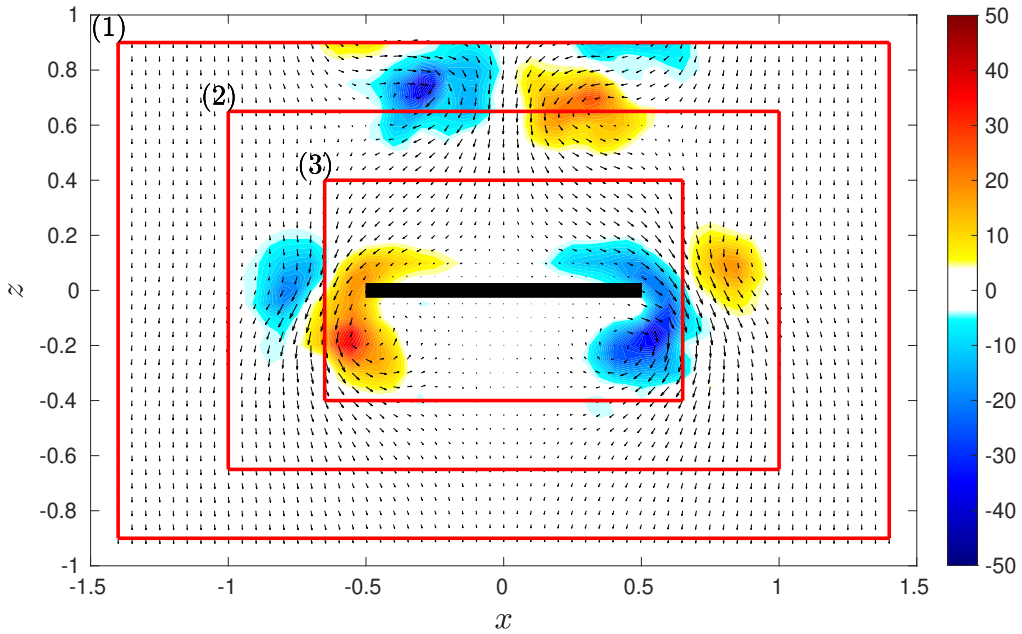

Fig. 7.11 Experimental windows used for computation in the hovering case.

UNIVERSIDAD DE MÁLAGA

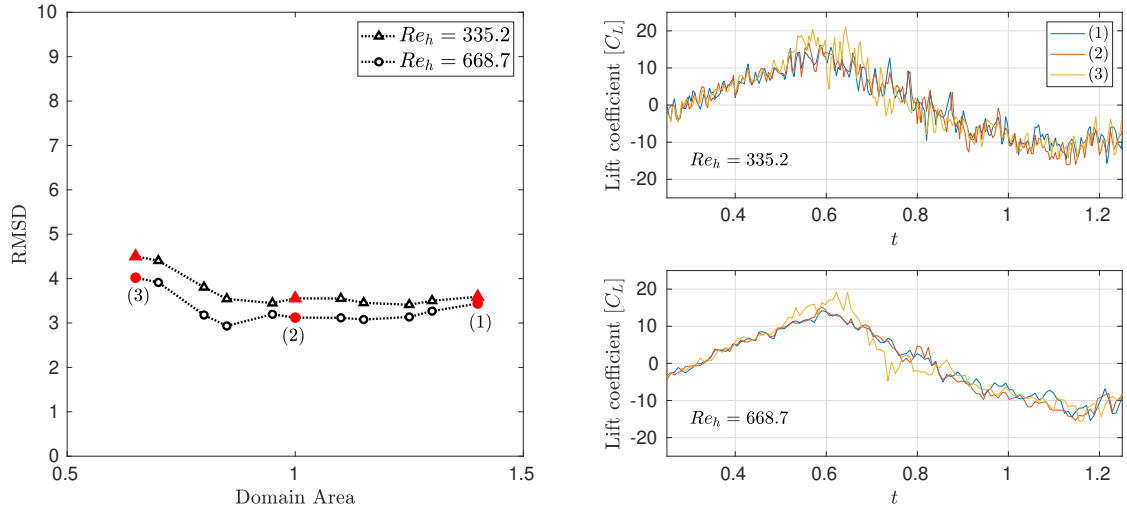

Fig. 7.12 RMSD against area of the domain on the left column for hovering experiments. The red highlighted points (1)-(3), represent the experimental window domains shown in Fig. 7.11. Temporal evolution of Lift coefficient is shown on right column.

line is the signal of reference. IF follows reasonably well the measured lift coefficient at low and high Re_h. However, the signal obtained from IF has a higher level of noise. Unlike the forward flight case, in the hovering configuration, there is never a repeated pattern over time because this case depends on (i) the initial instant where the movement of the oscillating plate begins, (ii) the diffusion of vortices in the surrounding flow forms chaotic patterns as the vortices generated in the downstroke and upstroke part of the cycle interact and (iii) the possible three-dimensionality of the recirculations in the spanwise direction (y-axis). Besides, we do believe that the small discrepancies in the estimation of the lift coefficient near the peaks are mainly due to the vorticity gradient close to the solid surface that is difficult to compute making use of 2D-PIV, see for example snapshots (2) and (4) on the right column for Re_h=668.7 in Fig. 7.10.

7.4 Conclusions

We have carried out 2D-PIV measurements using one flapping plate in both forward flight and hovering configurations. IF has the particularity that the main contribution of the force is based on the term $\vec{F_I}$ that corresponds to the vorticity multiplied by the distance to the object. This term helps reduce the influence on the final result due to the velocity field near the flapping flat plate, but it does not allow to rule out of the (high) importance of vortices

UNIVERSIDAD DE MÁLAGA

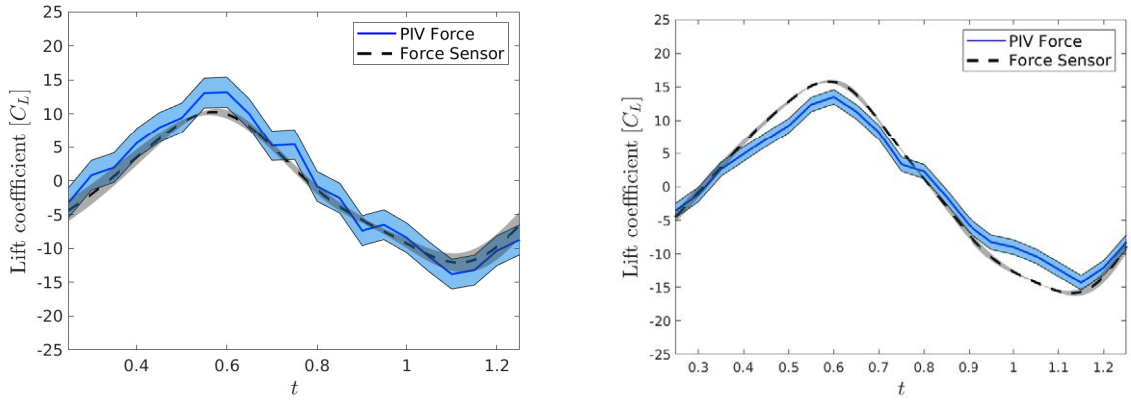

(a) (b)

Fig. 7.13 Temporal evolution of C_L with different computations (see legend) for Re_h=335.2 (a) and Re_h=668.7 (b).

far from the object. This last contribution is crucial in the term C_{Lo}, formed by the surface S_3 in the forward flight configuration. However, surfaces S_1 and S_2 have a weak influence in hovering while correcting the total lift. In the case of the hovering configuration, it has been found that the agreement between the force sensor data and the estimates of the impulse formulation are reasonable.

To the best of our knowledge, it is the first time that this impulse formulation given by Martín-Alcántara and Fernandez-Feria [128] has been successfully applied to the force calculation of the flapping wing problem from 2D-PIV data taking into account the vorticity that comes out of the domain in both forward flight and hovering configurations. This contribution is beneficial for increasing computations in real experiments with spatial domains within a spatially limited measurement region. However, the calculation of the drag coefficient is still a challenge though our case studies at a null angle of attack are quite promising.

UNIVERSIDAD DE MÁLAGA

Chapter 8

Conclusions and future work

8.1 Conclusions

This dissertation has focused on the characterization of wing aerodynamics with low and moderate Reynolds numbers. We describe the main findings as follows.

In the descriptive work that has been carried out at the experimental level, a total of two large installations have been set up to carry out tests for the measurement of force in a wind tunnel and in a towing tank. Thus, for example, the design, assembly and tuning of an experiment with a force sensor, described in the second chapter, has allowed to know the exact value of the temporal evolution in the forward flight and hovering configurations. Another important element in the development of this thesis has been a key tool for the generation of synthetic images of particle image velocimetry (PIV) by means of analytical solutions or numerical simulations. In addition to the implementation of an open-source algorithm in graphic processing units (GPUs) to know the velocity field through images. Note also that the analyzed flows are especially difficult to simulate and verify numerically.

Regarding the characterization of the lift distribution in finite size wings models, we have studied the aerodynamics of the wings outside the limits of potential theory. The conditions of Reynolds number of order 10^4 and aspect ratios, AR, between 2 and 4 are those corresponding to unmanned aerial vehicles (UAVs). Initially, we analyzed the canonical shape of a rectangular flat plate by varying the Reynolds number and aspect ratio in a wind tunnel. The lift slope $C_{L\alpha}$ was studied with these two variables to provide a single heuristic correlation with only two free parameters, where the influence of the Reynolds numbers and the aspect ratio are included simultaneously. The proposed correlation contains two parts, one that modifies the value of $C_{L\alpha}$ taking into account the use of finite wings and that behaves similarly to the results predicted by Prandtl's lifting line theory. The second part only depends on the Reynolds number having an exponent of 1/5.

UNIVERSIDAD DE MÁLAGA

Another conclusion is drawn from the characterization of non-linearity appearing in symmetrical thin foils for moderate Reynolds numbers in the UAV application range. Thus, and trying to extend this idea to real wings, a study on the NACA0012 profile was conducted both experimentally and numerically. Surprisingly, the lift curve shows a non-linear behavior for very low angles of attack. This behavior is not considered in many studies, and only three publications has referred to this strange phenomenon, but no explanation has been given yet. Using a low turbulence wind tunnel, we tested different wing models using the NACA0012 profile, and we observed that the non-linearity around the zero appears for semi-aspect ratios $AR = 2$ or more. The two-dimensional numerical simulations using a SST transition model implemented in Ansys®-Fluent v19.1 show this same behavior and the results have been validated with the previous research studies that were able to reproduce the negative lift obtaining a good agreement. As long as negative lift appears for relative large AR wing models, and 2D simulations are able to reproduce it, we conclude that is a completely 2D phenomenon. The numerical simulations also reveal that in cases with negative lift force, there is a pre-alignment of the flow upstream the airfoil that results in a maximum pressure gradient with a negative vertical component near the leading edge, promoting the negative lift.

Finally, there are some findings corresponding to the development of advanced experimental methods to indirectly evaluate the forces in 2D aerodynamic profiles for strongly non-stationary flows through the knowledge of the velocity field. Examples of this type of flows are the analytical solutions of the Navier-Stokes Equations or bio-inspired flight movements that have occupied the second half of the thesis. To this end, several research works have been developed that move towards the non-intrusive measurement of forces through numerical simulations or through experimental measurements in two dimensions by means of PIV. To achieve this objective we have taken three basic steps.

Firstly, we have developed a 2D-PIV software written in Python and accelerated by GPUs to dramatically increase the processing speed of the experimental velocity field. To this end, we have created synthetic images using analytic examples such as the Hagen-Poiseuille flow or the Rankine vortex finding that, although the calculation time can be up to 300 times faster compared to the calculation time given by a computer processing unit (CPU), the average errors made are assumable.

Secondly, and using CFD simulations we have simulated the flow around a square to obtain a non-stationary velocity field and the forces generated in the object. Using these simulations we have also generated synthetic images that imitate the numerical flow to test two force calculation methods and thus know their validity. In addition to the above, this set of synthetic images has also served to virtually reproduce an experiment with a limited

UNIVERSIDAD DE MÁLAGA

(spatial) window of vision. We have found that the momentum balance and the impulse formulation approaches can successfully reproduce the forces of a given velocity field. In our test, it was found that momentum balance requires the calculation of pressure as it is the most important term in the calculation. However, the impulse formulation does not require the pressure calculation and it has the particularity that the main contribution corresponds to the vorticity multiplied by the distance to the object. Furthermore, the approach of the impulse formulation has only given acceptable results in a certain range of limits associated with the spatial domain. The final spatial domain window chosen for experimental tests in the following step was approximately the one with the best result in reducing the error made with synthetic images from the numerical simulations.

Thirdly, an experiment of a flapping rectangular flat plate has been carried out and the forces obtained with a sensor are compared with those given by the impulse formulation, obtaining a good agreement. To that end, we have conducted 2D-PIV measurements using a flapping flat plate in both forward flight and hovering configurations. It has been verified that the contribution of the term containing the force on the vortex output surface is crucial in the forward flight configuration. However, the upper and lower surfaces have a weak influence. In the case of the hovering configuration, it has been found that the agreement between the force sensor data and the estimates of the impulse formulation are reasonable. Finally, the calculation of the drag coefficient is still a challenge, although our case studies at zero angle of attack are quite encouraging.

8.2 Future work

These brief assessments presented as conclusions on Aerodynamics with moderate and low Reynolds numbers, give the idea that their study requires a depth and a long time of investigation if one wants to account for the numerous phenomena of turbulence and the possible theoretical approaches to know the indirect calculation of the forces exerted by the aerodynamic profiles. As the research progressed, a number of considerations have been made which foresee numerous potential lines of research that could be developed from this study. Below we will briefly describe some of them.

It is still an open challenge to demonstrate the physical scale laws for the calculation of $C_{L\alpha}$ with respect to Re not only for a flat plate but also for other profiles as NACA0012. Besides, it is unknown the plausible theoretical explanation of the exponent 1/5 found for a flat plate.

As future work to extend the idea of negative lift that appears in the NACA0012 wing models, we plan to perform PIV measurements in a towing tank. In this setup, the level

UNIVERSIDAD DE MÁLAGA

of turbulence is reduced to almost to zero, so we expect to experimentally capture the mechanism that generates negative lift at a low angle of attack, which only appears in low turbulence conditions. Moreover, it is interesting to develop a code in spectral elements to better understand the mechanism that causes the pre-alignment of the flow upstream of the airfoil to appear.

Regarding the PIV estimate of forces by means of the velocity field there are some tasks planned to do further research. The first one is to run the PIV software for GPU accelerated computation presenting an exhaustive study of accuracy for 2D force estimations using different parameters of PIV such as particle size, overlap, interrogation windows or density of seeding along with the dimensions of the (bounded) spatial domain. To our knowledge, as long as OpenPIV GPU version remains alpha with only one pass implemented, this would be the first open-source GPU-accelerated PIV accessible to the community with double-pass and windows deformation. This alternative could be developed using synthetic images generated by numerical simulations.

On the indirect force estimate it should be interesting to perform a more exhaustive study of errors between different methods. In this sense, not only the momentum balance or the impulse formulation but also interesting to explore other methods using potential functions. Finally, it is worth mentioning how the calculation of the drag coefficient in flapping flat plate remains a challenge.

It would also be interesting to know experimentally in the towing tank the values of aerodynamic coefficients in a tandem of flapping flat plates instead of a single flat plate studied in this work. With respect to this problem the research group has 2D numerical simulations for different Reynolds numbers of the order of 1000 and different Strouhal values. The study with a mechanical system with two force sensors coupled to each flat plate and a synchronized encoder could give us the efficiency in this configuration of two plates. The PhD student has been involved in this task but there are still experimental issues to overcome.

Finally, the active control part is one of the tasks that have been developed to a lesser extent throughout this research work. However, the setting up of an active control in a wing model by means of a synthetic jet for different frequencies and different amplitudes that can be studied by means of the PIV technique in three dimensions is an activity that the author has been able to carry out and that has not been shown in this document. This study and a detailed analysis of the modes using Proper Orthogonal Decomposition or Dynamic Mode Decomposition is open.

UNIVERSIDAD DE MÁLAGA

References

[1] Alain Pelletier and Thomas J Mueller. Low reynolds number aerodynamics of low-aspect-ratio, thin/flat/cambered-plate wings. *Journal of Aircraft*, 37(5):825–832, 2000.

[2] F Fedoul, L Parras, C del Pino, and R Fernandez-Feria. Experimental study of the aerodynamic characteristics of a low-aspect-ratio flat plate array in a configuration of interest for a tidal energy converter. *Journal of Fluids and Structures*, 48:487–496, 2014.

[3] J. Tank, L. Smith, and G.R. Spedding. On the possibility (or lack thereof) of agreement between experiment and computation of flows over wings at moderate Reynolds number. *The Royal Societey*, 7:20160076, 2017.

[4] Tomohisa Ohtake, Yusuke Nakae, and Tatsuo Motohashi. Nonlinearity of the aerodynamic characteristics of NACA0012 aerofoil at low Reynolds numbers. *Japan Society of Aeronautical Space Sciences*, 55:439–445, 2007.

[5] Markus Raffel, Christian E Willert, Fulvio Scarano, Christian J Kähler, Steve T Wereley, and Jürgen Kompenhans. *Particle image velocimetry: a practical guide*. Springer, 2018.

[6] Eastman Nixon Jacobs, Kenneth Edwards Ward, and Robert McLean Pinkerton. *The Characteristics of 78 related airfoil section from tests in the Variable-Density Wind Tunnel*. Number 460. US Government Printing Office, 1933.

[7] Max M Munk. General theory of thin wing sections. 1923.

[8] S. D. Sharma and P. J. Deshpande. Kutta-Joukowsky theorem in viscous and unsteady flow. *Experiments in Fluids*, 52:1581–1591, 2012.

[9] T. Lee and Y. Y. Su. Low Reynolds number airfoil aerodynamic loads determination via line integral of velocity obtained with particle image velocimetry. *Experiments in Fluids*, 53:1177–1190, 2012.

[10] L. Rosenhead. The lift on a flat plate between parallel walls. *Proceeding Royal Society London A*, 132:127–152, 1931.

[11] T. H. Havelock. Flow over a flat plate with uniform inlet and incident coherent gusts. *Proceeding Royal Society London A*, 166:178–196, 1938.

[12] H. Glauert. *The Elements of Aerofoil and Airscrew Theory*. Cambridge Univ. Press, London, 1947.

UNIVERSIDAD DE MÁLAGA

[13] J. D. Anderson. *Fundamentals of Aerodynamics*. McGraw-Hill, New York, 1947.

[14] D. J. Pines and F. Bohorquez. Challenges facing future micro-air-vehicle development. *Journal of Aircraft*, 43(2):290–305, 2006.

[15] J.-M. Moschetta. The aerodynamics of micro air vehicles: technical challenges and scientific issues. *International Journal of Engineering Systems Modelling and Simulation*, 6:134–148, 2014. ISSN 1755-9758.

[16] E. N. Barmpounakis, E. I. Vlahogianni, and J. C. Golias. Unmanned aerial aircraft systems for transportation engineering: Current practice and future challenges. *International Journal of Transportation Science and Technology*, 5:111–122, 2016. ISSN 2046-0430.

[17] Jacopo Primicerio, Salvatore Filippo Di Gennaro, Edoardo Fiorillo, Lorenzo Genesio, Emanuele Lugato, Alessandro Matese, and Francesco Primo Vaccari. A flexible unmanned aerial vehicle for precision agriculture. *Precision Agriculture*, 13(4):517–523, 2012.

[18] Xinyu Xue, Yubin Lan, Zhu Sun, Chun Chang, and W Clint Hoffmann. Develop an unmanned aerial vehicle based automatic aerial spraying system. *Computers and electronics in agriculture*, 128:58–66, 2016.

[19] SR Herwitz, LF Johnson, SE Dunagan, RG Higgins, DV Sullivan, J Zheng, BM Lobitz, JG Leung, BA Gallmeyer, M Aoyagi, et al. Imaging from an unmanned aerial vehicle: agricultural surveillance and decision support. *Computers and electronics in agriculture*, 44(1):49–61, 2004.

[20] Kevin Y Ma, Pakpong Chirarattananon, Sawyer B Fuller, and Robert J Wood. Controlled flight of a biologically inspired, insect-scale robot. *Science*, 340(6132): 603–607, 2013.

[21] Wolfgang Send, Markus Fischer, Kristof Jebens, Rainer Mugrauer, Agalya Nagarathinam, and Felix Scharstein. Artificial hinged-wing bird with active torsion and partially linear kinematics. In *Proceeding of 28th Congress of the International Council of the Aeronautical Sciences*. Brisbane, Australia, 2012.

[22] Stefan Drzewiecki. *Théorie générale de l'hélice: hélices aériennes et hélices marines*. Gauthier-Villars et cie., 1920.

[23] Hermann Glauert. Airplane propellers. In *Aerodynamic theory*, pages 169–360. Springer, 1935.

[24] Gordon J Leishman. *Principles of helicopter aerodynamics with CD extra*. Cambridge university press, 2006.

[25] Jens Nørkær Sørensen. *General momentum theory for horizontal axis wind turbines*, volume 4. Springer, 2016.

[26] P. B. S. Lissaman. Low-Reyndols-number airfoils. *Ann. Rev. Fluid Mech.*, 15:423–434, 1983.

UNIVERSIDAD DE MÁLAGA

[27] R. Dudley. *The Biomechanics of Insect Flight*. Princeton University Press, 2000.

[28] G. R. Spedding and A. Hedenström. PIV-based investigations of animal flights. *Experiments in fluids*, 46:749–763, 2009.

[29] W. Shyy, H. Aono, C.-K. Kang, and H. Liu. *An Introduction to Flapping Wing Aerodynamics*. Cambridge University Press., 2013.

[30] A. W. Mackowski and C. H. K. Williamson. Direct measurement of thrust and efficiency of an airfoil undergoing pure pitching. *Journal of Fluid Mechanics*, 765: 524–543, 2015.

[31] T. Weis-Fogh and M. Jensen. Biology and physics of locust flight. *Proceeding Royal Society London B*, 239:415–585, 1956.

[32] M. J. Lighthill. *Mathematical Biofluiddynamics*. SIAM, 1975.

[33] S. Childress. *Mechanics of Swimming and Flying*. Cambridge University Press., 1981.

[34] P. Meunier and T. Leweke. Analysis and treatment of errors due to high velocity gradients in particle image velocimetry. *Experiments in fluids*, 35:408–421, 2003.

[35] R. Lagrange, C. Eloy, F. Nadal, and P. Meunier. Instability of a fluid inside a precessing cylinder. *Physics of Fluids*, 20(081701), 2008.

[36] T. Albrecht, H. M. Blackburn, J. M. Lopez, R. Manasseh, and P. Meunier. Triadic resonances in precessing rapidly rotating cylinder flows. *Journal of Fluid Mechanics*, 778:R1–12, 2015.

[37] J. H. García-Ortiz, A. Domínguez-Vázquez, J. J. Serrano-Aguilera, L. Parras, and C. del Pino. A complementary numerical and experimental study of the influence of Reynolds number on theoretical models for wingtip vortices. *Computers and Fluids*, 180:176–189, 2019.

[38] R Nakayama, Y. Nakamura, Y. Ohya, and S. Ozono. A numerical study on the flow around flat plates at low Reynolds numbers. *Journal of Wind Engineering and Industrial Aerodynamics*, 46:255–264, 1993.

[39] M. G. Savage and G. L. Larose. An experimental study of the aerodynamic influence of a pair of winglets on a flat plate model. *Journal of Wind Engineering and Industrial Aerodynamics*, 91:113–126, 2003.

[40] B. Wu, Q. Wang, H. Liao, Y. Li, and M. Li. Flutter derivatives of a flat plate section and analysis of flutter instability at various wind angles of attack. *Journal of Wind Engineering and Industrial Aerodynamics*, 196:104046, 2020.

[41] Z. Zhang, J. P. Hubner, A. Timpe, L. Ukeiley, Y. Abudaram, and P. Ifju. Effect of aspect ratio on flat-plate membrane airfoils. *50th AIAA Aerospace Sciences Meeting including the New Horizons Forum and Aerospace Exposition*, pages 1–15, 2012.

[42] H.-T. Yu and L. P. Bernal. Effects of pivot location and reduced pitch rate on pitching rectangular flat plates. *AIAA Journal*, pages 1–17, 2016.

UNIVERSIDAD DE MÁLAGA

[43] J. T. Murphy and H. Hu. An experimental study of a bio-inspired corrugated airfoil for micro air vehicle applications. *Experiments in Fluids*, 49:531–546, 2010.

[44] Z. Wang and I. Gursul. Lift enhancement of a flat-plate airfoil by steady suction. *AIAA Journal*, 55:1–18, 2017.

[45] J. M. Chen and Y.-C. Fang. Strouhal numbers of inclined flat plates. *Journal of Wind Engineering and Industrial Aerodynamics*, 61:99–112, 1996.

[46] W. E. Olmstead and D. L. Hector. The lift and drag on a flat plate at low Reynolds number via variational methods. *Quarterly of Applied Mathematics*, 25:415–422, 1966.

[47] I. Afgan, S. Benhamadouche, X. Han, P. Sagaut, and D. Laurence. Flow over a flat plate with uniform inlet and incident coherent gusts. *Journal of Fluid Mechanics*, 720: 457–485, 4 2013. ISSN 1469-7645.

[48] G. L. Larose and F. M. Livesey. Performance of streamlined bridge decks in relation to the aerodynamics of a flat plate. *Journal of Wind Engineering and Industrial Aerodynamics*, 69-71:851–860, 1997.

[49] A. Jafari, F. Ghanadi, M. Arjomandi, M. J. Emes, and B. S. Cazzolato. Correlating turbulence intensity and length scale with the unsteady lift force on flat plates in an atmospheric boundary layer flow. *Journal of Wind Engineering and Industrial Aerodynamics*, 189:218–230, 2019.

[50] J. Aguilar Cabello, P. Gutierrez-Castillo, L. Parras, C. del Pino, and E. Sanmigul-Rojas. On the onset of negative lift in a symmetric airfoil at very small angles of attack. *Physics of Fluids*, 32:055107, 2020.

[51] S Martínez-Aranda, AL García-González, L Parras, JF Velázquez-Navarro, and C del Pino. Comparison of the aerodynamic characteristics of the NACA0012 airfoil at low-to-moderate reynolds numbers for any aspect ratio. *International Journal of Aerospace Sciences*, 4(1):1–8, 2016.

[52] D. Küchemann. A simple method for calculating the span and chordwise loading on straight and swept wings of any given aspect ratio at subsonic speeds. *Research and Memoranda 2935*, 132:1–54, 1952.

[53] B. H. Wick. Study of the subsonic forces and moments on an inclined plate of infinite span. *NACA TN 3321*, pages 1–25, 1954.

[54] H. B. Helmbold. Der unverwundene Ellipsenflügel als tragende fläche. *Jahrbuch der Deutschen Luftfahrtforschung, R. Oldenbourg (Munich)*, pages I–111–I–113, 1942.

[55] L.W. Traub. Aerodynamic impact of aspect ratio at low Reynolds number. *Journal of Aircraft*, 50(2):626–634, 2013.

[56] T. LIneham and K. Mohseni. Leading-edge flow reattachment and the lateral static stability of low-aspect-ratio rectangular wings. *Physical Review Fluids*, 2:113901, 2017.

UNIVERSIDAD DE MÁLAGA

[57] S. Watkins, S. Ravi, and B. Loxton. The effect of turbulence on the aerodynamics of low Reynolds number wings. *Engineering Letters*, 18:1–6, 2010.

[58] S. Sunada, A. Sakaguchi, and K. Karachi. Airfoil section characteristics at a low reynolds number. *Journal of Fluids Engineering*, 119:129–135, 1997.

[59] M. Shields and K. Mohsenii. Effects of sideslip on the aerodynamics of low-aspect-ratio low-Reynolds-number wings. *AIAA Journal*, 50:85–99, 2012.

[60] R. C. Frost and R. Rutherford. Der unverwundene Ellipsenflügel als tragende fläche. *AIAA Journal*, pages 931–933, 1963.

[61] A. Fage and B. Johansen. On the flow of air behind an inclined flat plate of infinite span. *Proceeding Royal Society London A*, 116:170–197, 1927.

[62] G E Torres and T J Mueller. Low aspect ratio aerodynamics at low Reynolds numbers. *AIAA Journal*, 42(5):865–873, 2004.

[63] P. Cosyn and J. Vierendeels. Numerical investigation of low-aspect-ratio wings at low Reynolds numbers. *Journal of Aircraft*, 43(3):713–722, 2006.

[64] M. Mizoguchi and Y. Yamaguchi. Aerodynamic characteristics of rectangular flat plate wings in low Reynolds number flows. *Journal of the Japan Society for Aeronautical and Space Sciences*, 60:121–127, 2012.

[65] GK Ananda, PP Sukumar, and MS Selig. Measured aerodynamic characteristics of wings at low reynolds numbers. *Aerospace Science and Technology*, 42:392–406, 2015.

[66] J B Barlow, X Rae, and X Pope. *Low-Speed Wind Tunnel Testing, Chap 10*. Wiley, New York, 1999.

[67] Kenneth W McAlister. *NACA 0015 wing pressure and trailing vortex measurements*, volume 3151. National Aeronautics and Space Administration, Office of Management . . . , 1991.

[68] L. Bernstein and S. Hamid. On the effect of a swept-wing–plate junction flow on the lift and drag. *The Aeronautical Journal*, 99(987):293–305, 1995.

[69] A Malik. *Suppression of Junction Flow Effects in Half Model Wind Tunnel Testing*. PhD thesis, Loughborough University, 2012.

[70] E. N. Jacobs, K. E. Ward, and R. M. Pinkerton. The characteristics of 78 related airfoil sections for tests in the variable-density wind tunnel. *National Advisory Committe for Aeronautis (NACA)*, 790:523–552, 1933.

[71] S.-J. Lee and Y.-G. Jang. Control of flow around a NACA 0012 airfoil with a micro-riblet film. *Journal of Fluids and Structures*, 20:659–672, 2005.

[72] A. L. Heyes and D. A. R. Smith. Behaviour of trailing wing(s) in echelon formation due to wing twist and aspect ratio. *Aerospace Science and Technology*, 9:469–475, 2005.

UNIVERSIDAD DE MÁLAGA

[73] K. Inoaka, T. Mori, M. Yamaguchi, and M. Senda. Feedback flow control of a low-re airfoil by flap actuators. *Journal of Fluids and Structures*, 58:319–330, 2015.

[74] N. H. Al-Battal, D. J. Cleaver, and I. Gursul. Lift reduction by counter flowing wall jets. *Aerospace Science and Technology*, 78:682–695, 2018.

[75] F. J. García-Ortiz. J. H., Blanco-Rodríguez, L. Parras, and C. del Pino. Experimental observations of the effects of spanwise blowing on the wingtip vortex evolution at low Reynolds numbers. *European Journal of Mechanics - B/Fluids*, 80:133–145, 2020.

[76] E. V. Laitone. Wind tunnel tests of wings at Reynolds numbers below 70 000. *Experiments in Fluids*, 23(5):405–409, 1997. ISSN 07234864. doi: 10.1007/s003480050128.

[77] N. J. Kay, P. J. Richards, and R. N. Sharma. Influence of turbulence on cambered and symmetrical airfoils at low Reynolds numbers. *AIAA journal*, 58, 2020.

[78] M. H. Akbari and S.J. Prices. Simulation of dynamic stall for a NACA 0012 airfoil using a vortex method. *Journal of Fluids and Structures*, 17:855–574, 2003.

[79] M. Gunasekaran and R. Mukherjee. Behaviour of trailing wing(s) in echelon formation due to wing twist and aspect ratio. *Aerospace Science and Technology*, 63:294–303, 2017.

[80] J. Boulet, G. Dimitriadis, and X. Amanandolese. A modified leishman-beddoes model for airfoil sections undergoing dynamic stall at low Reynolds numbers. *Journal of Fluids and Structures*, 93:102852, 2020.

[81] D. Poire, Y. Harris, and A. Benaiss. Self-sustained aeroelastic oscillations of a NACA0012 airfoil at low-to-moderate Reynolds numbers. *Journal of Fluids and Structures*, 24:700–719, 2008.

[82] W. Kang, L. Pengfei, J. Zhang, and M. Xu. Effects of local oscillation of airfoil surface on lift enhancement at low Reynolds number. *Journal of Fluids and Structures*, 57: 49–65, 2015.

[83] W. Shyy, H. Aono, S. K. Chimakurthi, P. Trizila, C.-K. Kang, C.E.S. Cesnik, and H. Liu. Recent progess in flapping wind aerodynamics and aeroelasticity. *Progessin Aerospace Sciences*, 46:284–327, 2010.

[84] N. Chiereghin, D. Cleaver, and I. Gursul. Unsteady lift and moment of a periodically plunging airfoil. *Journal of Aircraft*, 57:208–222, 01 2019.

[85] C. del Pino, L. Parras, M. Felli, and R. Fernandez-Feria. Structure of trailing vortices: Comparison between particle image velocimetry measurements and theoretical models. *Physics of Fluids*, 23(113602), 2011.

[86] C. del Pino, J. M. López-Alonso, L. Parras, and R. Fernandez-Feria. Dynamics of the wing-tip vortex in the near field of a NACA 0012 airfoil. *The Aeronautical Journal*, 115:1166, 2011.

UNIVERSIDAD DE MÁLAGA

[87] F. Guignery, E. Montreuil, O. Thual, and X. Vancassel. Contrail microphysics in the near wake of a realistic wing through RANS simulations. *Aerospace Science and Technology*, 23:399–408, 2012.

[88] J. J. Serrano-Aguilera, García-Ortiz. J. H., A. Gallardo-Claros, L. Parras, and C. del Pino. Experimental characterization of wingtip vortices in the near field using smoke flow visualizations. *Experiments in Fluids*, 57:137, 2016.

[89] J. Feys and S. A. Maslowe. Linear stability of the moore-saffman model for a trailing wingtip vortex. *Physics of Fluids*, 26:024108, 2014.

[90] A. M. Edstrand, T. B. Davis, P. J. Schmid, and K. Taira. On the mechanism of trailing vortex wandering. *Journal of Fluid Mechanics*, 801:R1:1–11, 2016.

[91] F. Viola, C. Arratia, and F. Gallaire. Mode selection in trailing vortices: harmonic response of the non-parallel Batchelor vortex. *Journal of Fluid Mechanics*, 790: 523–552, 2016.

[92] F. J. Blaco-Rodriguez, J. O. Rodriguez-Garcia, L. Parras, and Carlos del Pino. Optimal response of Batchelor vortex. *Physics of Fluids*, 29:064108, 2017.

[93] T. J. Mueller and S. M. Batill. Experimental studies of separation on a two-dimensional airfoil at low Reynolds numbers. *AIAA J.*, 20:457–463, 1982.

[94] J. DeYoung and W. H. Jr Barling. *Technical Note 3500. Correction of additional span loadings computed by the weissinger seven-point method for moderately tapered wings of high aspect ratio*. National Advisrory Committe for Aeronautis (NACA), Wahington, 1956.

[95] K. Yonemoto, K. Takato, H. Ochi, and S. Fujie. Kutta condition violation in two-dimensional NACA0012 airfoil at low Reynolds numbers. In *26th AIAA Applied Aerodynamics Conference*, page 092407, 18-21 August 2008.

[96] S. Heinz. A review of hybrid RANS-LES methods for turbulent flows: Concepts and applications. *Progress in Aerospace Sciences*, page In press., 2020.

[97] Justin Winslow, Hikaru Otsuka, Bharath Govindarajan, and Inderjit Chopra. Basic understanding of airfoil characteristics at low reynolds numbers (10 4–10 5). *Journal of Aircraft*, 55(3):1050–1061, 2017.

[98] C. Pranesh, M. Sivapragasam, M.D. Deshpande, and H. K. Narahari. Negative lift characteristics of NACA 0012 aerofoil at low Reynolds numbers. *Indian Academy of Sciences*, 44:21, 2019.

[99] R. B. Langtry and F. R. Menter. Correlation-based transition modeling for unstructured parallelized computational fluid dynamics codes. *AIAA journal*, 47(12):2894–2906, 2009.

[100] R. B. Langtry, F. R. Menter, S. R. Likki, Y. B. Suzen, P. G. Huang, and S. Völker. A correlation-based transition model using local variables—part ii: test cases and industrial applications. *J. Turbomach.*, 128(3):423–434, 2006.

UNIVERSIDAD DE MÁLAGA

[101] P. Malan, K. Suluksna, and E. Juntasaro. Calibrating the $\gamma - re_\theta$ transition model for commercial cfd. *AIAA Paper*, 1142, 2009.

[102] R. Wang and Zuoli Xiao. Transition effects on flow characteristics around a static two-dimensional airfoil. *Phys. Fluids*, 32:035133, 2020.

[103] S. Gorji, M. Seddighi, C. Ariyaratne, A. E. Vardy, T. O'Donoghue, D. Pokrajac, and S. He. A comparative study of turbulence models in a transient channel flow. *Computers and fluids*, 89:111–123, 2014.

[104] Thomas Schiwietz and Rüdiger Westermann. Gpu-piv. In *VMV*, pages 151–158, 2004.

[105] Shuhei Tarashima, Manabu Tange, Satoshi Someya, Koji Okamoto, et al. Gpu accelerated direct cross-correlation piv with window deformation. In *Proceedings 15th Int Symp on Applications of Laser Techniques to Fluid Mechanics*, 2010.

[106] Frédéric Champagnat, Aurélien Plyer, Guy Le Besnerais, Benjamin Leclaire, Samuel Davoust, and Yves Le Sant. Fast and accurate piv computation using highly parallel iterative correlation maximization. *Experiments in fluids*, 50(4):1169, 2011.

[107] Guy Le Besnerais and Frédéric Champagnat. Dense optical flow by iterative local window registration. In *IEEE International Conference on Image Processing 2005*, volume 1, pages I–137. IEEE, 2005.

[108] Zachary J Taylor, Roi Gurka, Gregory A Kopp, and Alex Liberzon. Long-duration time-resolved piv to study unsteady aerodynamics. *IEEE Transactions on Instrumentation and Measurement*, 59(12):3262–3269, 2010.

[109] Andreas Klöckner, Nicolas Pinto, Yunsup Lee, Bryan Catanzaro, Paul Ivanov, and Ahmed Fasih. Pycuda and pyopencl: A scripting-based approach to gpu run-time code generation. *Parallel Computing*, 38(3):157–174, 2012.

[110] Jerry Westerweel. Digital particle image velocimetry: Theory and application. 1995.

[111] John E Stone, David Gohara, and Guochun Shi. Opencl: A parallel programming standard for heterogeneous computing systems. *Computing in science & engineering*, 12(3):66–73, 2010.

[112] Michael Scully. *Computation of helicopter rotor wake geometry and its influence on rotor harmonic airloads*. PhD thesis, Massachusetts Institute of Technology, 1975.

[113] J.-C Lin and D. Rockwell. Force identification by vorticity fields: techniques based on flow imaging. *Journal of Fluids and Structures*, 10:663–668, 1996.

[114] F. Noca, D. Shiels, and D. Jeon. Measuring instantaneous fluid dynamic forces on bodies, using only velocity fields and their derivatives. *Journal of Fluids and Structures*, 11:345–350, 1997.

[115] M. F. Unal, J.-C. Lin, and D. Rockwell. Force prediction by PIV imaging: a momentum-based approach. *Journal of Fluids and Structures*, 11:965–971, 1997.

UNIVERSIDAD DE MÁLAGA

[116] F. Noca, D. Shiels, and D. Jeon. A comparison of methods for evaluating time-dependent fluid dynamic forces on bodies, using only velocity fields and their derivatives. *Journal of Fluids and Structures*, 13:551–578, 1999.

[117] B. W. van Oudheusden, F. Scarano, and E. W. F. Casimiri. Non-intrusive load characterization of an airfoil using PIV. *Experiments in fluids*, 40:988–992, 2006.

[118] B. W. van Oudheusden, E. W. F. Casimiri, and F. Scarano. Aerodynamic load characterisation of a low speed aerofoil using particle image velocimetry. *The Aeronautical Journal*, 3240:197–205, 2008.

[119] T. Jardin, L. David, and A. Farcy. Characterization of vortical structures and loads based on time-resolved PIV for asymmetric hovering flapping flight. *Experiments in fluids*, 46:847–857, 2009.

[120] B. W. van Oudheusden. PIV-based pressure measurement. *Measurement Science and Technology*, 24, 2013.

[121] K. Gharali and D. A. Jonhson. PIV-based load investigation in dynamic stall for different reduced frequencies. *Experiments in fluids*, 55:1803–1807, 2014.

[122] F. F. Siala and J. A. Liburdy. Leading-edge vortex dynamics and impulse-based lift force analysis of oscillating airfoils. *Experiments in fluids*, 60:157, 2019.

[123] A. C. DeVoria, Z. R. Carr, and M. J. Ringuette. On calculating forces from the flow field with application to experimental volume data. *Journal of Fluid Mechanics*, 749: 297–319, 2014.

[124] T. Albrecht, V. del Campo, T. Weier, H. Metzkes, and J. Stiller. Deriving forces from 2D velocity field measurements. *The European Physical Journal Special Topics*, 220: 91–100, 2012.

[125] D. Rival, T. Prangemeier, and C. Tropea. The influence of airfoil kinematics on the formation of leading-edge vortices in bio-inspired flight. *Experiments in fluids*, 46: 823–833, 2009.

[126] A. Guissart, L. P. Bernal, G. Dimitriadis, and V. E. Terrapon. PIV-based estimation of unsteady loads on a flat plate at high angle of attack using momentum equation approaches. *Experiments in fluids*, 58:53, 2017.

[127] D. F. Kurtulus, F. Scarano, and L. David. Unsteady aerodynamic forces estimation on a square cylinder by tr-piv. *Experiments in fluids*, 42:185–196, 2007.

[128] A. Martín-Alcántara and R. Fernandez-Feria. An assessment of some vortex formulations for computing forces of a flapping foil at high Reynolds numbers. *Physical Review Fluids*, 4(024702), 2019.

[129] W. R. Graham, C. W. Pitt Ford, and H. Babinsky. An impulse-based approach to estimating forces in unsteady flow. *Journal of Fluid Mechanics*, 815:60–76, 2017.

[130] J. McClure and S. Yarusevych. Planar momentum balance in three-dimensional flows: applications to load estimation. *Experiments in fluids*, 60:41, 2019.

UNIVERSIDAD DE MÁLAGA

[131] E. Limacher, C. Morton, and D. Wood. On the calculation of force from PIV data using the generalized added-mass and circulatory force decomposition. *Experiments in fluids*, 60:4, 2019.

[132] L. L. Kang, L. Q. Liu, W. D. Su, and J. Z. Wu. Minimum-domain impulse theory for unsteady aerodynamic force. *Physics of Fluids*, 30(016107), 2018.

[133] J. Z. Wu, H. Y. Ma, and M. D. Zhou. *Vorticity and vortex dynamics*. Springer, 2006.

[134] J. Z. Wu, X. Y. Lu, and L. X. Zhuang. Integral force acting on a body due to local flow structures. *Journal of Fluid Mechanics*, 576:265–286, 2007.

[135] J. Z. Wu, L. Liu, and T. Liu. Fundamental theories of aerodynamic force in viscous and compressible complex flows. *Progress in Aerospace Sciences*, 99:27–63, 2018.

[136] Z. J. Wang. Vortex shedding and frequency selection in flapping flight. *Journal of Fluid Mechanics*, 410:323–341, 2000.

[137] G. C. Lewin and H. Haj-Hariri. Modelling thrust generation of a two-dimensional heaving airfoil in a viscous. *Journal of Fluid Mechanics*, 492:339–362, 2003.

[138] A. Martín-Alcántara, R. Fernandez-Feria, and E. Sanmiguel-Rojas. Vortex flow structures and interactions for the optimum thrust efficiency of a heaving airfoil at different mean angles of attack. *Physics of Fluids*, 27(073602), 2015.

[139] T. Y. Hubel and C. Tropea. The importance of leading edge vortices under simplified flapping flight conditions at the size scale of birds. *Journal of Experimental Biology*, 213:1930–1939, 2010.

[140] M. Moriche, O. Flores, and M García-Villalba. On the aerodynamic forces on heaving and pitching airfoils at low reynolds number. *Journal of Fluid Mechanics*, 828: 395–423, 2017.

[141] Z. J. Wang, J. M. Birch, and M. H. Dickinson. Unsteady forces and flows in low Reynolds number hovering flight: two-dimensional computations vs robotic wing experiments. *The Journal of Experimental Biology*, 207:449–460, 2004.

UNIVERSIDAD DE MÁLAGA